

## Hydrodynamic description of ultrarelativistic heavy-ion collisions

Peter F. Kolb<sup>1</sup> and Ulrich Heinz<sup>2</sup>

<sup>1</sup>*Department of Physics and Astronomy, SUNY Stony Brook,  
Stony Brook, NY 11974, USA*

<sup>2</sup>*Department of Physics, The Ohio State University,  
Columbus, OH 43210, USA*

Relativistic hydrodynamics has been extensively applied to high energy heavy-ion collisions. We review hydrodynamic calculations for Au+Au collisions at RHIC energies and provide a comprehensive comparison between the model and experimental data. The model provides a very good description of all measured momentum distributions in central and semiperipheral Au+Au collisions, including the momentum anisotropies (elliptic flow) and systematic dependencies on the hadron rest masses up to transverse momenta of about 1.5–2 GeV/ $c$ . This provides impressive evidence that the bulk of the fireball matter shows efficient thermalization and behaves hydrodynamically. At higher  $p_T$  the hydrodynamic model begins to gradually break down, following an interesting pattern which we discuss. The elliptic flow anisotropy is shown to develop early in the collision and to provide important information about the early expansion stage, pointing to the formation of a highly equilibrated quark-gluon plasma at energy densities well above the deconfinement threshold. Two-particle momentum correlations provide information about the spatial structure of the fireball (size, deformation, flow) at the end of the collision. Hydrodynamic calculations of the two-particle correlation functions do not describe the data very well. Possible origins of the discrepancies are discussed but not fully resolved, and further measurements to help clarify this situation are suggested.

**Contents**

1	Introduction . . . . .	3
2	Formulation of hydrodynamics . . . . .	6
2.1	Hydrodynamic prerequisites . . . . .	6
2.2	Hydrodynamic equations of motion . . . . .	7
2.3	The nuclear equation of state . . . . .	8
2.4	Initialization . . . . .	10
2.5	Decoupling and freeze-out . . . . .	14
2.6	Longitudinal boost invariance . . . . .	17
3	Phenomenology of the transverse expansion . . . . .	19
3.1	Radial expansion in central collisions . . . . .	19
3.2	Anisotropic flow in non-central collisions . . . . .	25
4	Experimental observables . . . . .	29
4.1	Momentum space observables . . . . .	29
4.1.1	Single particle spectra . . . . .	30
4.1.2	Mean transverse momentum and transverse energy . . . . .	39
4.1.3	Momentum anisotropies as early fireball signatures . . . . .	41
4.1.4	Elliptic flow at RHIC . . . . .	43
4.2	Space-time information from momentum correlations . . . . .	59
4.2.1	The hydrodynamic source function . . . . .	60
4.2.2	HBT-radii – central collisions . . . . .	63
4.2.3	HBT with respect to the reaction plane . . . . .	67
5	Summary and Conclusions . . . . .	74
	References . . . . .	77

## 1. Introduction

The idea of exploiting the laws of ideal hydrodynamics to describe the expansion of the strongly interacting matter that is formed in high energy hadronic collisions was first formulated by Landau in 1953.<sup>1</sup> Because of their conceptual beauty and simplicity, models based on hydrodynamic principles have been applied to calculate a large number of observables for various colliding systems and over a broad range of beam energies. However, it is by no means clear that the highly excited, but still small systems produced in those violent collisions satisfy the criteria justifying a dynamical treatment in terms of a macroscopic theory which follows idealized laws (see Section 2.1). Only recently, with first data<sup>2,3</sup> from the Relativistic Heavy Ion Collider (RHIC) at Brookhaven National Laboratory came striking evidence for a strong collective expansion which is, for the first time, in *quantitative* agreement with hydrodynamic predictions,<sup>4</sup> both in central and non-central collisions (in this case Au+Au collisions with center of mass (c.m.) energies of 130 and 200 GeV per nucleon-pair).

The validity of ideal hydrodynamics requires local relaxation times towards thermal equilibrium which are much shorter than any macroscopic dynamical time scale. The significance and importance of rapid thermalization of the created fireball matter cannot be over-stressed: Only if the system is close to local thermal equilibrium, its thermodynamic properties, such as its pressure, entropy density and temperature, are well defined. And only under these conditions can we pursue to study the equation of state of strongly interacting matter at high temperatures. This is particularly interesting in the light of the expected phase transition of strongly interacting matter which, at a critical energy density of about 1 GeV/fm<sup>3</sup>, undergoes a transition from a hadron resonance gas to a hot and dense plasma of color deconfined quarks and gluons. Lattice QCD calculations indicate<sup>5,6</sup> that this transition takes place rather rapidly at a critical temperature  $T_{\text{crit}}$  somewhere between 155 and 175 MeV.

In this article we review and discuss data and calculations which provide strong evidence that the created fireball matter reaches temperatures above  $2T_{\text{crit}}$  and which indicate a thermalization time below 1 fm/c. Due to the already existing extensive literature on relativistic hydrodynamics, in particular in the context of nuclear collisions, we will be rather brief on its theoretical foundations, referring instead to the available excellent introductory material<sup>7,8,9</sup> and comprehensive reviews.<sup>10,11,12</sup>

In Section 2 we briefly present the formulation of the hydrodynamic framework. Starting with the microscopic prerequisites, we perform the

transition to macroscopic thermodynamic fields and formulate the hydrodynamic equations of motion. These are equivalent to the local conservation of energy and momentum of a relativistic fluid, together with continuity equations for conserved charges in the system. The set of equations is closed by providing a nuclear equation of state whose parameterization is also presented in that section. This is followed by a discussion of the initial conditions at thermalization which are used to start off the hydrodynamic part of the collision fireball evolution. Towards the end of the expansion, local thermalization again breaks down because the matter becomes dilute and the mean free paths become large. Hence the hydrodynamic evolution has to be cut off by hand by implementing a “freeze-out criterion” which is discussed at the end of Section 2.

Phenomenological aspects of the expansion are studied in Section 3. First we elaborate on central collisions and their characteristics – their cooling behavior, their dilution, their expansion rates, etc. We then proceed to discuss the special features and possibilities offered by non-central collisions, due to the breaking of azimuthal symmetry. We will see how the initial spatial anisotropy of the nuclear reaction zone is rapidly degraded and transferred to momentum space. This results in a strong momentum anisotropy which is easily observable in the measured momentum spectra of the finally emitted hadrons.

Experimental observables reflecting the hydrodynamic fireball history are the subject of Section 4. These include both momentum and coordinate space observables. Momentum space features are discussed in Section 4.1. We begin by analyzing the angle-averaged transverse momentum spectra of a variety of different hadron species for evidence of azimuthally symmetric radial flow. The measured centrality dependences of the charged multiplicity near midrapidity, of the mean transverse energy per particle, and of the shapes and mean transverse momenta of identified hadron spectra are compared with hydrodynamic calculations. We then discuss azimuthal momentum anisotropies by decomposing the same spectra into a Fourier series with respect to the azimuthal emission angle  $\varphi_p$  relative to the reaction plane. We investigate in particular the mass and centrality dependence of the second Fourier coefficient  $v_2(p_T)$ , the *differential elliptic flow*. Combining the experimental observations with a simple and quite general theoretical arguments, we will build a compelling case for the necessity of *rapid thermalization* and *strong rescattering* at early times. We will show that this provides a very strong argument for the creation of a well-developed quark-gluon plasma at RHIC, with a significant lifetime of about 5-7 fm/c

and an initial energy density which exceeds the critical value for color deconfinement by at least an order of magnitude.

In Section 4.2 we describe how two-particle momentum correlations can be used to explore the *spatial* geometry of the collision fireball at the time of hadron emission. This so-called Hanbury Brown-Twiss (HBT) intensity interferometry supplements the momentum space information extracted from the single particle spectra with information about the size and shape of the fireball in coordinate space. Whereas the momentum anisotropies are fixed early in the collision, spatial anisotropies continue to evolve until the very end of the collision, due to the early established anisotropic flow. By combining information on the momentum and spatial anisotropies one can hope to constrain the total time between nuclear impact and hadronic freeze-out rather independently from detailed theoretical arguments. We will show that, contrary to the momentum spectra, the experimentally measured HBT size parameters are not very well described by the hydrodynamical model. Since, contrary to the momentum anisotropies, the HBT correlations are only fixed at the point of hadronic decoupling, one might suspect that they are particularly sensitive to the drastic and somewhat unrealistic sharp freeze-out criterion employed in the hydrodynamic simulations. However, this so-called *HBT-puzzle*<sup>13,14</sup> is shared by most other available dynamical models, including those which start hydrodynamically but then describe hadron freeze-out kinetically,<sup>15,16,17,18,19,20</sup> and still awaits its resolution.

In our concluding Section 5 we give a summary and also highlight the need for future studies of uranium-uranium collisions. Since uranium nuclei in their ground state are significantly deformed, the long axis being almost 30% larger than the short one, they offer a significantly deformed initial geometry even for central collisions with complete nuclear overlap.<sup>4,21,22</sup> The resulting deformed fireballs are much larger and significantly denser than those from equivalent semicentral gold-gold collisions, providing better conditions for local thermalization and the validity of hydrodynamic concepts even at lower beam energies where data from Au+Au and Pb+Pb collisions indicate a gradual breakdown of ideal hydrodynamics.<sup>23</sup> Central U+U collisions may thus provide a chance to explore the hydrodynamic behavior of elliptic flow down to lower collision energies and confirm the hydrodynamic prediction<sup>4,24</sup> of a non-monotonic structure in its excitation function which can be directly related to the quark-hadron phase transition and its softening effects on the nuclear equation of state in the transition region (see also Section 4.1).

## 2. Formulation of hydrodynamics

### 2.1. Hydrodynamic prerequisites

For macroscopic systems with a large number (say, of the order of Avogadro's number) of microscopic constituents, thermodynamics takes advantage of the fact that fluctuations in the system are small, microscopic dynamics drives such systems rapidly to a state of maximum disorder, and the system's global behavior can then be expressed in terms of a few macroscopic thermodynamic fields. Thermalization happens locally and on microscopic time scales which are many orders of magnitude smaller than the macroscopic time scales related to the reaction of the system to small inhomogeneities of the density, pressure, temperature, etc. Under such conditions, the system can be described as an ideal fluid which reacts instantaneously to any changes of the local macroscopic fields, by readjusting the slope of its particles' momentum distribution (i.e. its temperature) locally on an infinitesimally short time scale. The resulting equations of motion for the macroscopic thermodynamic fields are the equations of ideal (i.e. non-viscous) hydrodynamics, i.e. the Euler equations and their relativistic generalizations.<sup>25</sup> They describe how macroscopic pressure gradients generate collective flow of the matter, subject to the constraints of local conservation of energy, momentum, and conserved charges.

The systems produced in the collision of two large nuclei are much smaller: In central Au+Au or Pb+Pb collisions at RHIC energies (i.e. up to 200 GeV per nucleon pair in the center of mass system), about 400 nucleons collide with each other, producing several thousand secondary particles. Recent experiments with trapped cold fermionic atoms with tunable interaction strength have shown that systems involving a few hundred thousand particles behave hydrodynamically if the local re-equilibration rates are sufficiently large.<sup>26,27</sup> Similar experiments involving much smaller numbers of atoms are under way. In fact, one can argue that the number of particles is not an essential parameter for the validity of the hydrodynamic approach, and that hydrodynamics does not even rely on the applicability of a particle description for the expanding system at all. The only requirement for its validity are sufficiently large momentum transfer rates on the microscopic level such that relaxation to a local thermal equilibrium configuration happens fast on macroscopic time scales. Local thermal equilibrium can also be formulated for quantum field theoretical systems which are too hot and dense to allow for a particle description because large scattering rates never let any of the particles go on-shell.

If the fireballs formed in heavy ion reactions were not expanding, the typical macroscopic time scales would be given by the spatial dimensions of the reaction zone divided by the speed of sound  $\sim c/\sqrt{3}$ , i.e. of the order of  $10 \text{ fm}/c$ . Collective expansion reduces this estimate, and the geometric criterion must be replaced by a dynamical one involving the local expansion rate (“Hubble constant”),  $\tau_{\text{exp}}^{-1} = \partial_\mu u^\mu$  where  $u^\mu(x)$  is the local flow 4-velocity.<sup>28,29,30,31</sup> Typical values for  $\tau_{\text{exp}}$  are of the order of only one to several  $\text{fm}/c$ .<sup>32</sup> The hydrodynamic description of heavy-ion collisions thus relies on local relaxation times below  $1 \text{ fm}/c$  which, until recently, was thought to be very difficult to achieve in heavy-ion collisions, causing widespread skepticism towards the hydrodynamic approach. The new RHIC data have helped to overcome this skepticism, leaving us with the problem to theoretically explain the microscopic mechanisms behind the observed fast thermalization rates.

From these considerations it is clear that in heavy-ion collisions a hydrodynamic description can only be valid during a finite interval between thermalization and freeze-out. Hydrodynamics can never be expected to describe the earliest stage of the collision, just after nuclear impact, during which some of the initial coherent motion along the beam direction is redirected into the transverse directions and randomized. The results of this process enter the hydrodynamic description through *initial conditions* for the starting time of the hydrodynamic stage and for the relevant macroscopic density distributions at that time. The hydrodynamic evolution is ended by implementing a *freeze-out condition* which describes the breakdown of local equilibrium due to decreasing local thermalization rates. These *initial and final conditions* are crucial components of the hydrodynamic model which must be considered carefully if one wants to obtain phenomenologically relevant results.

## 2.2. Hydrodynamic equations of motion

The energy momentum tensor of a thermalized fluid cell in its local rest frame is given by<sup>25</sup>  $T_{\text{rest}}^{\mu\nu}(x) = \text{diag}(e(x), p(x), p(x), p(x))$  where  $x$  labels the position of the fluid cell and  $e(x)$  and  $p(x)$  are its energy density and pressure. If in a global reference frame this fluid cell moves with four-velocity  $u^\mu(x)$  (where  $u^\mu = \gamma(1, v_x, v_y, v_z)$  with  $\gamma = 1/\sqrt{1 - \mathbf{v}^2}$  and  $u^\mu u_\mu = 1$ ), a corresponding boost of  $T_{\text{rest}}^{\mu\nu}$  yields the fluid’s energy momentum tensor in the global frame:

$$T^{\mu\nu}(x) = \left( e(x) + p(x) \right) u^\mu(x) u^\nu(x) - p(x) g^{\mu\nu}. \quad (1)$$

Note that this form depends on local thermal equilibrium at each point of the fluid in its local rest frame, i.e. it corresponds to an *ideal fluid* where dissipative effects can be neglected. The local conservation of energy and momentum can be expressed by

$$\partial_\mu T^{\mu\nu}(x) = 0, \quad (\nu = 0, \dots, 3). \quad (2)$$

If the fluid carries conserved charges  $N_i$ , with charge densities  $n_i(x)$  in the local rest frame and corresponding charge current densities  $j_i^\mu(x) = n_i(x)u^\mu(x)$  in the global reference frame, local charge conservation is expressed by

$$\partial_\mu j_i^\mu(x) = 0, \quad i = 1, \dots, M. \quad (3)$$

Examples for such conserved charges are the net baryon number, electric charge, and net strangeness of the collision fireball.

If local relaxation rates are not fast enough to ensure almost instantaneous local thermalization, the expressions for the energy momentum tensor and charge current densities must be generalized by including dissipative terms proportional to the transport coefficients for diffusion, heat conduction, bulk and shear viscosity.<sup>7,8,25</sup> The solution of the correspondingly modified equations is very challenging.<sup>33</sup> We will later discuss some first order viscous corrections in connection with experimental observables.

### 2.3. The nuclear equation of state

The set (2,3) of  $4 + M$  differential equations involves  $5 + M$  undetermined fields: the 3 independent components of the flow velocity, the energy density, the pressure, and the  $M$  conserved charge densities. To close this set of equations we must provide a nuclear equation of state  $p(e, n_i)$  which relates the local thermodynamic quantities. We consider only systems with zero net strangeness and do not take into account any constraints from charge conservation which are known to have only minor effects.<sup>34</sup> This leaves the net baryon number density  $n$  as the only conserved charge density to be evolved dynamically.

The equation of state for dense systems of strongly interacting particles can either be modeled or extracted from lattice QCD calculations. We use a combination of these two possibilities: In the low temperature regime, we follow Hagedorn<sup>35</sup> and describe nuclear matter as a noninteracting gas of hadronic resonances, summing over all experimentally identified<sup>36</sup> resonance states.<sup>37,38</sup> As the temperature is increased, a larger and larger fraction of the available energy goes into the excitation of more and heavier

resonances. This results in a relatively soft equation of state (“EOS H”) with a smallish speed of sound:  $c_s^2 = \partial p / \partial e \approx 0.15$ .<sup>24</sup>

As the available volume is filled up with resonances, the system approaches a phase transition in which the hadrons overlap and the microscopic degrees of freedom change from hadrons to deconfined quarks and gluons. Due to the large number of internal quark and gluon degrees of freedom (color, spin, and flavor) and their small or vanishing masses, this transition is accompanied by a rather sudden increase of the entropy density at a critical temperature  $T_{\text{crit}}$ . Above the transition, the system is modeled as a noninteracting gas of massless  $u$ ,  $d$ ,  $s$  quarks and gluons, subject to an external bag pressure  $B$ .<sup>39</sup> The corresponding equation of state  $p = \frac{1}{3}e - \frac{4}{3}B$  is quite stiff and yields a squared sound velocity  $c_s^2 = \partial p / \partial e = \frac{1}{3}$  which is more than twice that of the hadron resonance gas. In the following we refer to this equation of state as “EOS I”.

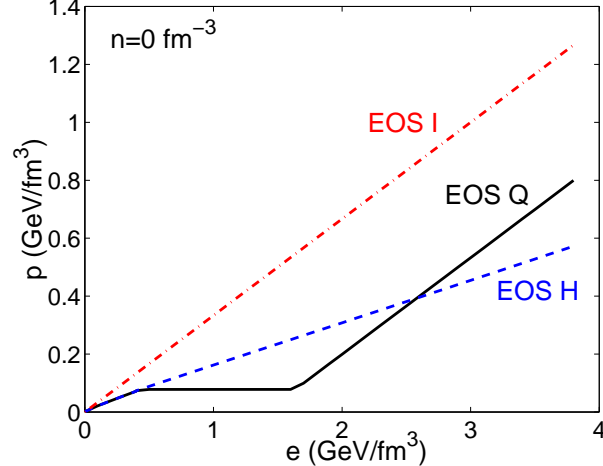


Fig. 1. Equation of state of the Hagedorn resonance gas (EOS H), an ideal gas of massless particles (EOS I) and the Maxwellian connection of those two as discussed in the text (EOS Q). The figure shows the pressure as function of energy density at vanishing net baryon density.

We match the two equations of state by a Maxwell construction, adjusting the bag constant  $B^{1/4} = 230$  MeV such that for a system with zero net baryon density the transition temperature coincides with lattice QCD results.<sup>5,6</sup> We choose<sup>38</sup>  $T_{\text{crit}} = 164$  MeV and call the resulting combined equation of state “EOS Q”. It is plotted as  $p(e)$  at vanishing net baryon

density and strangeness in Figure 1, together with the hadron resonance gas EOS H and the ideal gas of massless partons, EOS I. The Maxwell construction inevitably leads to a strong first order transition,<sup>37</sup> with a large latent heat  $\Delta e_{\text{lat}} = 1.15 \text{ GeV/fm}^3$  (between upper and lower critical values for the energy density of  $e_Q = 1.6 \text{ GeV/fm}^3$  and  $e_H = 0.45 \text{ GeV/fm}^3$ ).<sup>24</sup> This contradicts lattice QCD results<sup>5,6</sup> which suggest a smoother transition (either very weakly first order or a smooth cross-over). However, the total increase of the entropy density across the transition as observed in the lattice data<sup>5,6</sup> is well reproduced by the model, and it is unlikely that the artificial sharpening of the transition by the Maxwell construction leads to significant dynamical effects. This is in particular true since the numerical algorithm used to solve the hydrodynamic equations tends to soften shock discontinuities such as those which might be generated by a strong first order phase transition. We will return to the possible influence of details of the EOS on certain observables in Section 4 when we discuss experimental data.

#### 2.4. Initialization

As discussed in Section 2.1, the initial thermalization stage in a heavy-ion collision lies outside the domain of applicability of the hydrodynamic approach and must be replaced by initial conditions for the hydrodynamic evolution. Different authors have explored a variety of routes to arrive at reasonable such initial conditions. For example, one can try to treat the two colliding nuclei as two interpenetrating cold fluids feeding a third hot fluid in the reaction center (“three-fluid dynamics”<sup>11</sup>). This requires modelling the source and loss terms describing the exchange of energy, momentum and baryon number among the fluids. Alternatively, one can model the early stage kinetically, using a transport model such as the parton cascades VNI<sup>40</sup>, VNI/BMS<sup>41</sup>, MPC<sup>42</sup>, AMPT<sup>43</sup> or one of several other available transport codes to estimate the initial energy and entropy distributions in the collision region<sup>44</sup> before switching to a hydrodynamic evolution.

However, the microscopic effects which generate the initial entropy are still poorly understood, and it is quite likely that, due to the high density and collision rates, transport codes which simulate the solution of a Boltzmann equation using on-shell particles are not really valid during the early thermalization stage. In our own calculations, we therefore simply parameterize the initial transverse entropy or energy density profile geometrically, using an optical Glauber model calculation<sup>45</sup> to estimate the density of

wounded nucleons and binary nucleon-nucleon or parton-parton collisions in the plane transverse to the beam and superimposing a “soft” component (scaling with the number of wounded nucleons) and a “hard” component (scaling with the number of binary collisions) in such a way<sup>46,47</sup> that the experimentally observed rapidity density of charged hadrons at the end of the collision<sup>48,49</sup> and its dependence on the collision centrality<sup>50,51</sup> are reproduced.<sup>46</sup>

For the Glauber calculation we describe the density distributions of the colliding nuclei (with mass numbers  $A$  and  $B$ ) by Woods-Saxon profiles,

$$\rho_A(r) = \frac{\rho_0}{e^{(r-R_A)/\xi} + 1}, \quad (4)$$

with the nuclear radius  $R_A = (1.12 A^{1/3} - 0.86 A^{-1/3})$  fm and the surface diffuseness  $\xi = 0.54$  fm.<sup>52</sup> The nuclear thickness function is given by the optical path-length through the nucleus along the beam direction:

$$T_A(x, y) = \int_{-\infty}^{\infty} dz \rho_A(x, y, z). \quad (5)$$

The coordinates  $x, y$  parametrize the transverse plane, with  $x$  pointing in the direction of the impact parameter  $\mathbf{b}$  (such that  $(x, z)$  span the reaction plane) and  $y$  perpendicular to the reaction plane. For a non-central collision with impact parameter  $b$ , the density of binary nucleon-nucleon collisions  $n_{BC}$  at a point  $(x, y)$  in the transverse plane is proportional to the product of the two nuclear thickness functions, transversally displaced by  $b$ :

$$n_{BC}(x, y; b) = \sigma_0 T_A(x + b/2, y) T_B(x - b/2, y). \quad (6)$$

$\sigma_0$  is the total inelastic nucleon-nucleon cross section; it enters here only as a multiplicative factor which is later absorbed in the proportionality constant between  $n_{BC}(x, y; b)$  and the “hard” component of the initial entropy deposition.<sup>46</sup> Integration over the transverse plane (the  $(x, y)$ -plane) yields the total number of binary collisions,

$$N_{BC}(b) = \int dx dy n_{BC}(x, y; b) \quad (7)$$

Its impact parameter dependence, as well as that of the maximum density of binary collisions in the center of the reaction zone,  $n_{BC}(0, 0; b)$ , are shown as the dashed lines in Fig. 2.

The “soft” part of the initial entropy deposition is assumed to scale with the density of “wounded nucleons”,<sup>53</sup> defined as those nucleons in the projectile and target which *participate* in the particle production process by suffering at least one collision with a nucleon from the other nucleus.

The Glauber model gives the following transverse density distribution of wounded nucleons:<sup>53</sup>

$$n_{WN}(x, y; b) = T_A(x + b/2, y) \left( 1 - \left( 1 - \frac{\sigma_0 T_B(x - b/2, y)}{B} \right)^B \right) \\ + T_B(x - b/2, y) \left( 1 - \left( 1 - \frac{\sigma_0 T_A(x + b/2, y)}{A} \right)^A \right). \quad (8)$$

Here the value  $\sigma_0$  of the total inelastic nucleon-nucleon cross section plays a more important role since it influences the shape of the transverse density distribution  $n_{WN}(x, y; b)$ , and its dependence<sup>36</sup> on the collision energy  $\sqrt{s}$  must be taken into account. The total number of wounded nucleons is obtained by integrating Eq. (8) over the transverse plane. Its impact parameter dependence, as well as that of the maximum density of wounded nucleons in the center of the reaction zone,  $n_{WN}(0, 0; b)$ , are shown as the solid lines in Fig. 2.

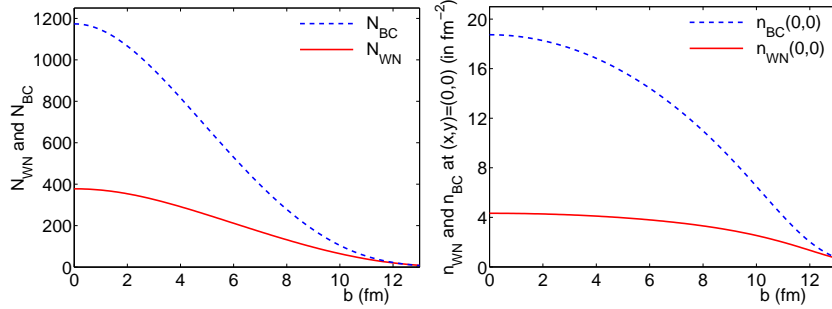


Fig. 2. Left: Number of wounded nucleons and binary collisions as a function of impact parameter, for Au+Au collisions  $\sqrt{s} = 130$  A GeV ( $\sigma_0 = 40$  mb). Right: Density of wounded nucleons and binary collisions in the center of the collision as a function of impact parameter.

Our hydrodynamic calculations were done with initial conditions which ascribed 75% of the initial entropy production to “soft” processes scaling with  $n_{WN}(x, y; b)$  and 25% to “hard” processes scaling with  $n_{BC}(x, y; b)$ . This was found<sup>46</sup> to give a reasonable description of the measured<sup>50,51</sup> centrality dependence of the produced charged particle rapidity density per participating (“wounded”) nucleon.

Figure 2 shows that exploring the centrality dependence of heavy-ion collisions provides access to rich physics: With increasing impact parameter

both the number of participating nucleons and the volume of the created fireball decrease. Except for effects related to the deformation of the reaction zone in non-central collisions, increasing the impact parameter is thus equivalent to colliding smaller nuclei, eventually reaching the limit of  $pp$  collisions in the most peripheral nuclear collisions. Furthermore, at fixed beam energy, the initially deposited entropy and energy densities decrease with increasing impact parameter. To a limited extent, heavy-ion collisions at fixed beam energy but varying impact parameter are therefore equivalent to central heavy-ion collisions at varying beam energy, i.e. one can map sections of the “excitation function” of physical observables without changing the collision energy, but only the collision centrality.

In one respect, however, non-central collisions of large nuclei such as Au+Au are fundamentally different from central collisions between lighter nuclei: A finite impact parameter breaks the azimuthal symmetry inherent in all central collisions. In a strongly interacting fireball, the initial geometric anisotropy of the reaction zone gets transferred onto the final momentum spectra and thus becomes experimentally accessible. As we will see, this provides a window into the very early collision stages which is completely closed in central collisions between spherical nuclei. (The same information is, however, accessible, with even better statistics due to the larger overlap volume and number of produced particles, in completely central collisions between *deformed* nuclei, such as W+W or U+U.)

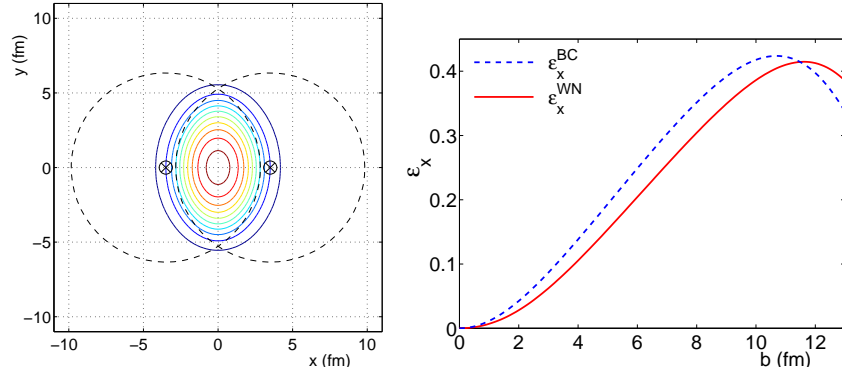


Fig. 3. Density of binary collisions in the transverse plane for a Au+Au collision with impact parameter  $b = 7$  fm (left). Shown are contours of constant density together with the projection of the initial nuclei (dashed lines). The right plot shows the geometric eccentricity as a function of the impact parameter for the wounded nucleon and binary collision distributions.

The left panel of Fig. 3 shows the distribution of binary collisions in the transverse plane for Au+Au collisions at impact parameter  $b = 7$  fm. Shown are lines of constant density at 5, 15, 25, ...% of the maximum value. The dashed lines indicate the Woods-Saxon circumferences of the two colliding nuclei, displaced by  $\pm b/2$  from the origin. The obvious geometric deformation of the overlap region can be quantified by the *spatial eccentricity*

$$\epsilon_x(b) = \frac{\langle y^2 - x^2 \rangle}{\langle y^2 + x^2 \rangle}, \quad (9)$$

where the averages are taken with respect to the underlying density ( $n_{\text{WN}}$  or  $n_{\text{BC}}$  or a combination thereof, depending on the exact parametrization used). The centrality dependence of  $\epsilon_x$  is displayed in the right panel of Fig. 3.

### 2.5. Decoupling and freeze-out

As already mentioned in Section 2.1, the hydrodynamic description begins to break down again once the transverse expansion becomes so rapid and the matter density so dilute that local thermal equilibrium can no longer be maintained. Detailed studies<sup>32,54</sup> comparing local mean free paths with the overall size of the expanding fireball and the local Hubble radius (inverse expansion rate) have shown that bulk freeze-out happens *dynamically*, i.e. it is driven by the expansion of the fireball and not primarily by its finite size. This is similar to the decoupling of the primordial nuclear abundances and the cosmic microwave background in the early universe which was also entirely controlled by the cosmic expansion rate. Nonetheless, some part of the initially produced matter never becomes part of the hydrodynamic fluid, but decouples right away even though no transverse flow has developed yet. Figure 2 shows that already at initialization the density distribution has dilute tails where the mean free path is never short enough to justify a hydrodynamic treatment. These tails should be considered as immediately frozen out, i.e. they describe particles which carry their momentum information directly and without further modification to the detector. Their decoupling is obviously not a result of (transverse) dynamics, but a geometric effect. However, for both geometric and dynamical freeze-out the local scattering rate (density times cross section) is the controlling factor, with the density showing the largest variations across the fireball, and it was found<sup>32,54</sup> that the hypersurface along which the local mean free path begins to exceed the local Hubble radius or the global fireball size can be

characterized in good approximation as a surface of constant temperature. Note that for almost baryon-antibaryon symmetric systems such as the ones generated near midrapidity at RHIC, the entropy density, energy density, particle density and temperature profiles are directly related and all have similar shapes. A surface of constant temperature is therefore, in excellent approximation, also a surface of constant energy and particle density.

A traditional way of describing the breakdown of hydrodynamics and particle freeze-out is the Cooper-Frye prescription<sup>55</sup> which postulates a sudden transition from perfect local thermal equilibrium to free streaming of all particles in a given fluid cell once the kinetic freeze-out criterion (obtained, for example, in the way just described, by comparing local scattering and expansion rates etc.) is satisfied in that cell. In the Cooper-Frye formalism, one first lets hydrodynamics run up to large times, then determines the space-time hypersurface  $\Sigma(x)$  along which the hydrodynamic fluid cells first pass the freeze-out criterion, and computes the final spectrum of particles of type  $i$  from the formula

$$E \frac{dN_i}{d^3p} = \frac{dN_i}{dp p_T dp_T d\varphi_p} = \frac{g_i}{(2\pi)^3} \int_{\Sigma} f_i(p \cdot u(x), x) p \cdot d^3\sigma(x), \quad (10)$$

where  $d^3\sigma_{\mu}(x)$  is the outward normal vector on the freeze-out surface  $\Sigma(x)$  such that  $p^{\mu} f_i d^3\sigma_{\mu}$  is the local flux of particles with momentum  $p$  through this surface. For the phase-space distribution  $f$  in this formula one takes the local equilibrium distribution *just before* decoupling,

$$f_i(E, x) = \frac{1}{\exp[(E - \mu_i(x))/T(x)] \pm 1}, \quad (11)$$

boosted with the local flow velocity  $u^{\mu}(x)$  to the global reference frame by the substitution  $E \rightarrow p \cdot u(x)$ .  $\mu_i(x)$  and  $T(x)$  are the chemical potential of particle species  $i$  and the local temperature along  $\Sigma$ , respectively. The temperature and chemical potentials on  $\Sigma$  are computed from the hydrodynamic output, i.e. the energy density  $e$ , net baryon density  $n$  and pressure  $p$ , with the help of the equation of state.<sup>38</sup>

This formalism is used to calculate the momentum distribution of all directly emitted hadrons of all masses. Unstable resonances are then allowed to decay (we include all strong decays, but consider weakly decaying particles as stable), taking the appropriate branching ratio of different decay-channels into account.<sup>36</sup> The contribution of the decay products is added to the thermal momentum spectra of the directly emitted stable hadrons to give the total measured particle spectra.<sup>56</sup>

Initial particle production at high  $p_T$  is controlled by hard QCD processes which produce transverse momentum spectra which strongly deviate from an exponential thermal or hydrodynamic shape. Since the momentum transfer per collision is limited, such particles require a larger number of rescatterings than soft particles for reaching thermal equilibrium. They have a much higher chance of escaping from the fireball before being thermalized than soft hadrons. This is not captured by the Cooper-Frye formula which freezes out *all* particles in a given fluid cell together, irrespective of their momenta. A modified freeze-out criterium which takes the momentum dependence of the escape probability into account has recently been advocated.<sup>57,58,59</sup> We will discuss phenomena at large transverse momenta in the last part of Section 4.1.

The Cooper-Frye formula has another shortcoming which materializes if the freeze-out normal vector  $d^3\sigma^\mu(x)$  is spacelike (as it happens in certain regions of our hydrodynamic freeze-out surfaces), in which case the Cooper-Frye integral also counts (with negative flux) particles entering the thermalized fluid from outside. However, simple attempts to cut these contributions by hand<sup>60</sup> generate problems with energy-momentum conservation, and only recently a possible resolution of this problem has been found.<sup>61</sup>

Clearly, any Cooper-Frye like prescription implementing a sudden transition from local equilibrium (infinite scattering cross section) to free-streaming (zero cross section) is ultimately unrealistic and should be replaced by a more realistic prescription. A preferred procedure would be the transition from hydrodynamics to kinetic transport theory just before hydrodynamics begins to break down,<sup>15,16,17,18,19,20</sup> thus allowing for a gradual decoupling process which is fully consistent with the underlying microscopic physics. Such a realistic treatment of the freeze-out process is clearly much more involved than the Cooper-Frye formalism, and so far it has not led to strong qualitative differences for the emitted hadron spectra, even though in detail some phenomenological advantages of the hybrid (hydro+transport) approach can be identified.<sup>19</sup> Also, the crucial question whether for rapidly expanding heavy-ion fireballs there is really an overlap window where both the macroscopic hydrodynamic and the microscopic transport approach using on-shell particles work simultaneously has not been finally settled. Most of the results presented in this review have therefore been obtained using the simple Cooper-Frye freeze-out algorithm.

### 2.6. *Longitudinal boost invariance*

Most of the observables to be discussed below have been collected near mid-rapidity. This region is of particular interest as one expects there the energy- and particle density to be the largest, giving the clearest signals of the anticipated phase-transition, and many components of the large heavy-ion experiments have therefore been optimized for the detection of midrapidity particles. Furthermore, rapidity distributions are more difficult to analyze theoretically than transverse momentum distributions since they are strongly affected by “memories of the pre-collision state”: Whereas all transverse momenta are generated by the collision itself, a largely unknown fraction of the beam-component of the momenta of the produced hadrons is due to the initial longitudinal motion of the colliding nuclei. In hydrodynamics one finds that final rapidity distributions are very sensitive to the initialization along the beam direction, and that hydrodynamic evolution is not very efficient in changing the initial distributions.<sup>64</sup> Collective transverse effects are thus a cleaner signature of the reaction dynamics than longitudinal momentum distributions, and the best way to isolate oneself longitudinally from remnants of the initially colliding nuclei is by going as far away as possible from the projectile and target rapidities, i.e. by studying midrapidity hadron production.

Near midrapidity one is far from the kinematic limits imposed by the finite collision energy, and the microscopic processes responsible for particle production, scattering, thermalization and expansion should therefore be locally the same everywhere and invariant under limited boosts along the beam direction.<sup>62</sup> In a hydrodynamic description this implies a boost-invariant longitudinal flow velocity<sup>62</sup> whose form is independent of the transverse expansion of the fluid while the latter is identical for all transverse planes in their respective longitudinal rest frames. Under these assumptions the analytically solvable longitudinal evolution decouples from the transverse evolution<sup>63,70</sup> which greatly reduces the numerical task of solving the hydrodynamic equations of motion. Limitations of Bjorken’s solution and boost invariance will be discussed in Section 4.1.4, but most of the review reports results obtained under the assumption of longitudinal boost invariance.

Bjorken showed<sup>62</sup> that the boost invariant longitudinal flow field has the scaling (Hubble) form  $v_z = z/t$  and that the hydrodynamic equations preserve this form in proper time if the initial conditions for the thermodynamic variables do not depend on space-time rapidity  $\eta =$

$\frac{1}{2} \ln[(t+z)/(t-z)]$ . With this profile the flow 4-velocity can be parametrized as  $u^\mu = \cosh y_\perp(\cosh \eta, v_x, v_y, \sinh \eta)$ , where the transverse flow rapidity  $y_\perp(\tau, \mathbf{r})$  does not depend on  $\eta$  and is related to the radial flow velocity  $v_r = \sqrt{v_x^2 + v_y^2}$  at midrapidity  $\eta = 0$  by  $v_r(\tau, \mathbf{r}, \eta=0) = \tanh y_\perp(\tau, \mathbf{r})$ . It is then sufficient to solve the hydrodynamic equations for  $v_r$  at  $z = 0$ , and the transverse velocity at other longitudinal positions is given by<sup>63</sup>

$$v_r(t, \mathbf{r}, z) = v_r(\tau, \mathbf{r}, \eta) = \frac{v_r(\tau, \mathbf{r}, 0)}{\cosh \eta}. \quad (12)$$

Solving the hydrodynamic equations in the transverse plane  $\mathbf{r} = (x, y)$  with longitudinally boost-invariant boundary conditions becomes easiest after a coordinate transformation from  $(z, t)$  to longitudinal proper time  $\tau$  and space-time rapidity  $\eta$ :

$$\begin{aligned} x^\mu &= (t, x, y, z) \longrightarrow \bar{x}^m = (\tau, x, y, \eta) \\ t &= \tau \cosh \eta & \tau &= \sqrt{t^2 - z^2} \\ z &= \tau \sinh \eta & \eta &= \text{Artanh}(z/t). \end{aligned} \quad (13)$$

In these coordinates, the equations of motions become<sup>4</sup>

$$T^{\tau\tau, \tau} + (v_x T^{\tau\tau})_{,x} + (v_y T^{\tau\tau})_{,y} = -\frac{1}{\tau} (T^{\tau\tau} + p) - (p v_x)_{,x} - (p v_y)_{,y}, \quad (14)$$

$$T^{\tau x, \tau} + (v_x T^{\tau x})_{,x} + (v_y T^{\tau x})_{,y} = -p_{,x} - \frac{1}{\tau} T^{\tau x}, \quad (15)$$

$$T^{\tau y, \tau} + (v_x T^{\tau y})_{,x} + (v_y T^{\tau y})_{,y} = -p_{,y} - \frac{1}{\tau} T^{\tau y}, \quad (16)$$

$$\frac{1}{\tau^2} p_{,\eta} = 0, \quad (17)$$

$$j^\tau_{,\tau} + (v_x j^\tau)_{,x} + (v_y j^\tau)_{,y} = -\frac{1}{\tau} j^\tau, \quad (18)$$

where the lower case comma indicates a partial derivative with respect to the coordinate following it. One sees that the evolution in  $\eta$ -direction is now trivial, and that only 4 coupled equations remain to be solved.

### 3. Phenomenology of the transverse expansion

In this section we study the transverse fireball expansion at midrapidity as it follows from the hydrodynamic equations of motion (Sections 2.2 and 2.6) with the equation of state described in Section 2.3 and the initial conditions from Section 2.4.

In the first part of this section we study central collisions ( $b = 0$ ). These are used to tune the initial conditions of the calculations, by requiring the calculation to reproduce the measured rapidity density of charged hadrons at midrapidity and the shape of the pion and proton spectra in central collisions. For Au+Au collisions with a center of mass energy of 200 GeV per nucleon pair, we find for the initial equilibration time (i.e. for the beginning of the hydrodynamic stage)  $\tau_{\text{equ}} = 0.6 \text{ fm}/c$  and an initial entropy density in the center of the fireball of  $s_{\text{equ}} = 110 \text{ fm}^{-3}$ .<sup>65</sup> Freeze-out occurs when the energy density drops below  $e_{\text{dec}} = 0.075 \text{ GeV}/\text{fm}^3$ . How these parameters are fixed will be described in some detail in Section 4.1. In the present section we will simply use them to illustrate some of the characteristic features of the transverse hydrodynamic expansion.

In the second part we address non-central collisions and discuss the special opportunities provided by the breaking of azimuthal symmetry in this case. We discuss how the initial spatial deformation transforms rapidly into a momentum space anisotropy which ultimately manifests itself through a dependence of the emitted hadron spectra and their momentum correlations on the azimuthal emission angle relative to the reaction plane.

#### 3.1. Radial expansion in central collisions

As seen from the terms on the right hand side in Eqs. (14)-(16), the driving force for the hydrodynamic expansion are the transverse pressure gradients which accelerate the fireball matter radially outward, building up collective transverse flow. As a result, the initial one-dimensional boost-invariant expansion along the beam direction gradually becomes fully three-dimensional. For the adiabatic (ideal fluid) expansion discussed here, this implies that the entropy and other conserved charges spread out over a volume which initially grows linearly with time, but as time evolves increases faster and ultimately as  $\tau^3$ . Accordingly, the entropy and baryon densities follow inverse power laws  $\sim \tau^{-\alpha}$  with a “local expansion coefficient”  $\alpha = -\frac{\partial \ln s}{\partial \ln \tau}$  which changes smoothly from 1 to 3.

This is seen in the left panel of Figure 4 which shows a double logarithmic plot of the entropy density at three points in the fireball (at the origin

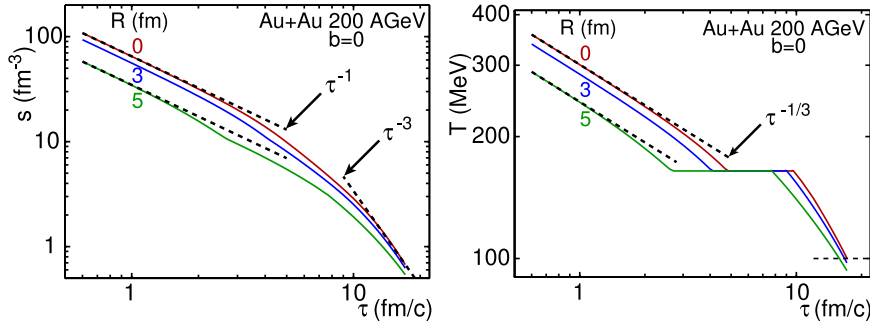


Fig. 4. Left panel: Time evolution of the entropy density at three different points in the fireball (0, 3, and 5 fm from the center). Dashed lines indicate the expectations for pure one-dimensional and three-dimensional dilution, respectively. Right panel: Time evolution of the temperature at the same points. The plateau at  $T = 164$  MeV results from the transition of the corresponding fluid cells through the mixed phase.

$R=0$  as well as 3 and 5 fm away from it) as a function of time. At early and late times the solid lines representing the numerical solution are seen to follow simple  $\tau^{-1}$  and  $\tau^{-3}$  scaling laws, indicated by dashed lines. For an ideal gas of massless particles (such as our model for the quark-gluon plasma above the hadronization phase transition)  $s \sim T^3$ , and a  $\tau^{-1}$  scaling of the entropy density translates into a  $\tau^{-1/3}$  scaling of the temperature. The right panel of Figure 4 shows that the numerical solution follows this simple scaling rather accurately almost down to the phase transition temperature  $T_{\text{crit}}$ . At this point the selected fluid cell enters the mixed phase and the temperature remains constant until the continued expansion dilutes the energy density below the lower critical value  $e_H = 0.45$  GeV/fm $^3$ . This is an artefact of the Maxwell construction employed in Section 2.3; for a more realistic rapid but smooth crossover between the QGP and hadron gas phases the horizontal plateau in Figure 4 would be replaced by a similar one with smoothed edges and a small but finite slope. As the fluid cell exits the phase transition on the hadronic side, its temperature is seen to drop very steeply; this is caused not only by the now much more rapid three-dimensional expansion, but also by the different temperature dependence of  $s(T)$  in the hadronic phase, generated by the exponential dependence of the phase-space occupancy on the hadron rest masses. The horizontal dashed line indicates the freeze-out temperature of about 100 MeV (see Section 4.1); one sees that in central collisions freeze-out occurs about 15 fm/ $c$  after equilibration.

Figure 5 compares the time-dependence of the local expansion coefficient  $\alpha = -\frac{\partial \ln s}{\partial \ln \tau} = -\frac{\tau}{s} \frac{\partial s}{\partial \tau}$  with that of the local expansion rate divided by

the boost-invariant longitudinal expansion rate,  $\tau(\partial_\mu u^\mu)$ .<sup>66</sup> The horizontal dashed lines indicate the expectations for pure 1-dimensional longitudinal (Bjorken-like) expansion ( $\alpha = \tau(\partial_\mu u^\mu) = 1$ ) and for 3-dimensional isotropic radial (Hubble-like) expansion ( $\alpha = \tau(\partial_\mu u^\mu) = 3$ ), respectively. One sees

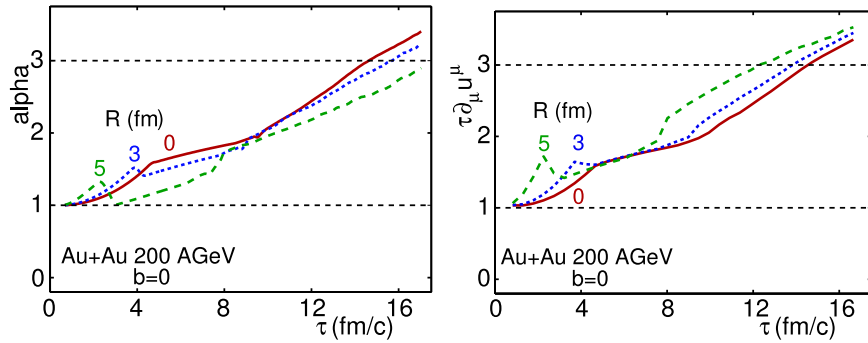


Fig. 5. Left panel: Time evolution of the local expansion coefficient  $\alpha = -\partial(\ln s)/\partial(\ln \tau)$  at three different fireball locations. The horizontal dashed lines indicate expectations for pure Bjorken ( $\alpha = 1$ ) and Hubble-like expansions ( $\alpha = 3$ ). Right panel: The local expansion rate  $\partial_\mu u^\mu$  multiplied by time, again compared to Bjorken and Hubble-like scaling expansions. Note that the expansion coefficient  $\alpha$  decreases with radial distance from the center whereas the expansion rate shows the opposite behavior.

that in the numerical solutions both quantities increase with time from a Bjorken-like behavior initially to a Hubble-like behavior at later times. Weak structures in the time evolution at the beginning and end of the mixed phase are probably due to our artificially sharp phase transition and should disappear for a realistic equation of state. Note that both the local expansion coefficient  $\alpha$  and the normalized local expansion rate  $\tau \partial \cdot u$  exceed the limiting global value of 3 at large times. This does not violate causality, but is due to the existence of density gradients and their time evolution.<sup>66</sup>

At late times the expansion rate  $\tau \partial \cdot u$  is larger for points at the edge of the fireball than in the center, again due to the stronger density and pressure gradients near the edge. In contrast, the local dilution rate  $\alpha$  shows the opposite dependence on the radial distance, being smaller at large radial distance than in the center. This reflects the transport of matter from the center to the edge, due to radial flow and density gradients.<sup>66</sup> The relation between  $\alpha$  and  $\tau \partial \cdot u$  can be established by using entropy conservation,  $\partial_\mu(su^\mu) = 0$ , to write  $\partial \cdot u = -(u \cdot \partial s)/s$ . Assuming longitudinal boost-invariance and a temporal power law  $s(r, \tau) = s_0(r)(\frac{\tau_0}{\tau})^\alpha$  for the lo-

cal entropy dilution rate one finds the relation<sup>66</sup>

$$\partial_\mu u^\mu = \gamma \left( \frac{\alpha}{\tau} - v_r \frac{\partial_r s_0}{s_0} \right). \quad (19)$$

The last term involving the radial flow and radial entropy density gradient is positive, especially at large radii, explaining the different ordering of the three curves in the left and right panels of Figure 5.

To further illustrate the transverse dynamics we show in Figure 6 the radial velocity  $v_r$  as a function of time and radial distance. The left panel shows the time evolution of  $v_r$  at fixed radii of 3 and 5 fm. After a steep initial rise of  $v_r$ , the radial velocity at fixed position  $R$  is seen to decrease with time while the matter there changes from QGP into a hadron gas. Inside the mixed phase the pressure is constant (i.e. the pressure gradient vanishes) and the matter is not further accelerated. As a result, the system expands without acceleration, with rapidly flowing matter moving to larger radii while more slowly moving matter from the interior arrives at the fixed radius  $R$ . Only after the mixed phase has completely passed through the radius  $R$  does the radial expansion accelerate again, caused by the reappearance of pressure gradients.

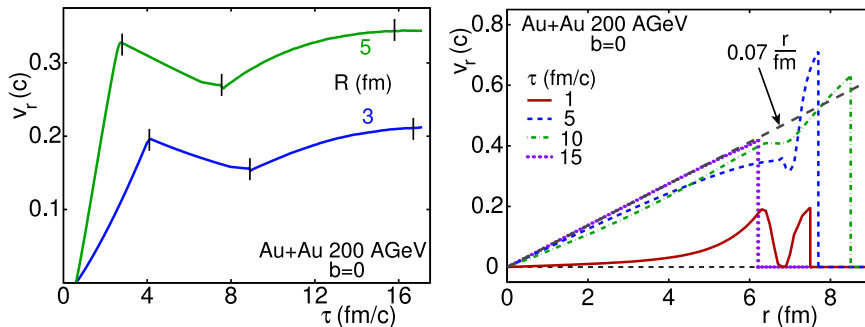


Fig. 6. Left panel: Time evolution of the collective radial velocity at 3 and 5 fm radial distance from the origin. The short vertical lines in the figure indicate the beginning and end of the hadronization phase transition and the freeze-out time. Right panel: The radial velocity profile  $v_r(r)$  at four different times. The dashed line indicates a linear profile  $v_r(r) = \xi r$  with slope  $\xi = 0.07$  fm $^{-1}$ .

The right panel of Figure 6 shows the radial velocity profile at selected times. Initially  $v_r \equiv 0$  whereas the pressure profile  $p(r)$  features strong radial gradients (especially near the surface), except for a moderately thin layer between the QGP and hadron gas phases where the matter is in the phase transition and the corresponding softness of the equation of state does not

allow for pressure gradients. Accordingly, the initial acceleration happens mostly in the outer part of the QGP core and in the hadron gas shell, with no acceleration in the mixed phase layer which only gets squashed by the accelerating matter pushing out from the interior. This is clearly seen in the solid line in Figure 6 which represents the radial velocity profile at  $\tau = 1 \text{ fm}/c$ . As time proceeds the structure caused by the weak acceleration in the mixed phase gets washed out and the velocity profile becomes more uniform. It very rapidly approaches a nearly linear shape  $v_r(r) \approx \xi r$  with an almost time-independent limiting slope of  $\xi \simeq 0.07 \text{ fm}^{-1}$ .

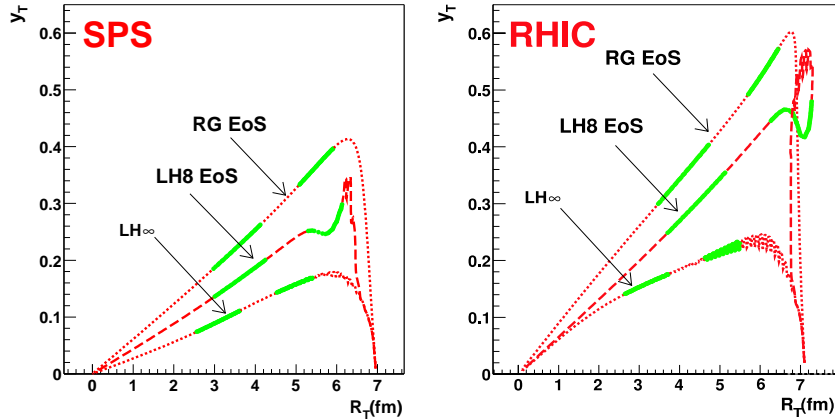


Fig. 7. The transverse flow rapidity  $y_\perp$  as a function of radial distance  $r$  along a surface of constant energy density  $e = 0.45 \text{ GeV}/\text{fm}^3$ , for Pb+Pb collisions at the SPS (left) and for Au+Au collisions at RHIC (right).<sup>19</sup> Three different equations of state have been explored in this figure,<sup>19</sup> with LH8 corresponding most closely to EOS Q shown in Figure 1. The dashed and solid line segments subdivide the surface into 5 equal pieces of 20% each with respect to the entropy flowing through the surface.

The near constancy of this slope implies that one also obtains an almost linear transverse velocity profile along a hypersurface of fixed temperature or energy density rather than fixed time. Figure 7 compares the radial flow rapidity profile  $y_\perp(r)$  for Pb+Pb or Au+Au collisions at SPS and RHIC energies for three different equations of state,<sup>19</sup> with LH8 corresponding most closely to EOS Q shown in Figure 1. Figure 7 provides welcome support for the phenomenologically very successful blast-wave parametrization<sup>67,68</sup> which is usually employed with a linear transverse velocity or rapidity profile for reasons of simplicity. (Note that for the range of velocities covered in the figure the difference between rapidity  $y_\perp$  and velocity  $v_r = \tanh y_\perp$  can be neglected.)

As discussed in Sections 2.1 and 2.5, the freeze-out of particle species  $i$  is mostly controlled by the competition between the macroscopic expansion time scale<sup>32,31</sup>  $\tau_{\text{exp}} = (\partial \cdot u)^{-1}$  and the microscopic scattering time scale  $\tau_{\text{scatt}}^i = 1 / \sum_j \langle \sigma_{ij} v_{ij} \rangle \rho_j$ ; here the sum goes over all particle species  $j$  (with density  $\rho_j$ ) in the fireball and  $\langle \sigma_{ij} v_{ij} \rangle$  are the corresponding thermally averaged and velocity weighted scattering cross sections. The scattering rates drop steeply with temperature,<sup>32,68,69</sup> enabling us to idealize freeze-out as a relatively sudden process which happens along a freeze-out surface  $\Sigma$  of approximately constant decoupling temperature  $T_{\text{dec}}$ . The most important contributions to the local scattering rate arise from  $\pi$ +meson (due to their large abundance) and  $\pi$ +(anti)baryon collisions (due to their large resonant cross sections). At RHIC the total baryon density is somewhat lower than at the SPS, due to the smaller baryon chemical potential (note that this does not reduce the contribution from baryon-antibaryon pairs!), and one thus expects that, at the same temperature, the mean scattering time  $\tau_{\text{scatt}}$  should be slightly longer at RHIC than at the SPS. The magnitude of this effect should be small, however, and its sign could even be reversed if at RHIC the pion phase-space is significantly oversaturated.<sup>59</sup>

On the other hand, the expansion time scale  $\tau_{\text{exp}} = (\partial \cdot u)^{-1}$  does change significantly between SPS and RHIC: For boost-invariant longitudinal flow and a linear transverse flow rapidity profile  $y_{\perp} = \xi r$  (as suggested by Figs. 6 and 7) the expansion rate is easily calculated as<sup>66</sup>

$$\partial \cdot u = \frac{\cosh(\xi r)}{\tau} + \xi \left( \cosh(\xi r) + \frac{\sinh(\xi r)}{\xi r} \right) \approx \frac{1}{\tau} + 2\xi, \quad (20)$$

where the approximate expression<sup>59</sup> holds in the region  $\xi r \ll 1$ . Equation (20) gives  $\tau(\partial \cdot u) = 1 + 2\xi\tau$ ; reading off  $\xi \approx 0.07$  from Figures 6 and 7 at RHIC energies, this linear function reproduces well the almost linear behavior seen in the right panel of Fig. 5. On the other hand, Figure 7 shows at SPS energies a transverse flow rapidity slope that is only about 2/3 of the value at RHIC. At freeze-out ( $\tau_{\text{dec}} \simeq 15 - 17 \text{ fm}/c$ <sup>4,19</sup>) the expansion rate at RHIC is thus about 25% larger than at the SPS ( $(\partial \cdot u)_{\text{dec}} \approx 0.21$  for Au+Au at  $\sqrt{s} = 130 \text{ A GeV}$  vs.  $(\partial \cdot u)_{\text{dec}} \approx 0.16$  for Pb+Pb at  $\sqrt{s} = 17 \text{ A GeV}$ ). The corresponding “Hubble times” at freeze-out are  $\tau_{\text{exp}}^{\text{dec}}(\text{RHIC}) \approx 4.8 \text{ fm}/c$  and  $\tau_{\text{exp}}^{\text{dec}}(\text{SPS}) \approx 6.1 \text{ fm}/c$ . Combining this with the already mentioned rather similar microscopic scattering time scales at both energies one is led to the conclusion that at RHIC freeze-out should happen at a somewhat higher decoupling temperature than at the SPS.

### 3.2. Anisotropic flow in non-central collisions

In Section 2.4 we have already addressed some of the great opportunities offered by non-central collisions. The most important ones are related to the broken azimuthal symmetry, introduced through the spatial deformation of the nuclear overlap zone at non-zero impact parameter (see Figure 3). If the system evolves hydrodynamically, driven by its internal pressure gradients, it will expand more strongly in its short direction (i.e. into the direction of the impact parameter) than perpendicular to the reaction plane where the pressure gradient is smaller.<sup>70</sup> This is shown in Figure 8 where contours of constant energy density are plotted at times 2, 4, 6 and 8 fm/c after thermalization. The figure illustrates qualitatively that, as the system evolves, it becomes less and less deformed. In addition, some interesting fine structure develops at later times: After about 6 fm/c the energy density distribution along the  $x$ -axis becomes non-monotonous, forming two fragments of a shell that enclose a little 'nut' in the center.<sup>71</sup> Unfortunately, when plotting a cross section of the profiles shown in Figure 8 one realizes that this effect is rather subtle, and it was also found to be fragile, showing a strong sensitivity to details of the initial density profile.<sup>4</sup>

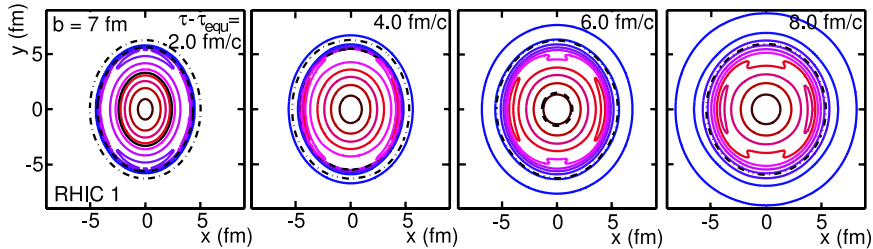


Fig. 8. Contours of constant energy density in the transverse plane at different times (2, 4, 6 and 8 fm/c after equilibration) for a Au+Au collision at  $\sqrt{s_{\text{NN}}} = 130$  GeV and impact parameter  $b = 7$  fm.<sup>4,72</sup> Contours indicate 5, 15, ..., 95 % of the maximum energy density. Additionally, the black solid, dashed and dashed-dotted lines indicate the transition to the mixed-phase, to the resonance gas phase and to the decoupled stage, where applicable.

A more quantitative characterization of the contour plots in Figure 8 and their evolution with time is provided by defining the *spatial eccentricity*

$$\epsilon_x(\tau) = \frac{\langle y^2 - x^2 \rangle}{\langle y^2 + x^2 \rangle}, \quad (21)$$

where the brackets indicate an average over the transverse plane with

the local energy density  $e(x, y; \tau)$  as weight function, and the *momentum anisotropy*

$$\epsilon_p(\tau) = \frac{\int dx dy (T^{xx} - T^{yy})}{\int dx dy (T^{xx} + T^{yy})}. \quad (22)$$

Note that with these sign conventions, the spatial eccentricity is positive for out-of-plane elongation (as is the case initially) whereas the momentum anisotropy is positive if the preferred flow direction is *into* the reaction plane.

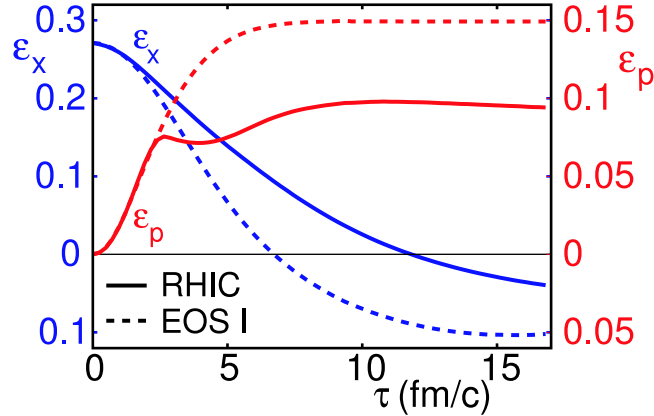


Fig. 9. Time evolution of the spatial eccentricity  $\epsilon_x$  and the momentum anisotropy  $\epsilon_p$  for Au+Au collisions at RHIC with  $b=7$  fm.<sup>73</sup>

Figure 9 shows the time evolution of the spatial and momentum anisotropies for Au+Au collisions at impact parameter  $b=7$  fm, for RHIC initial conditions with a realistic equation of state (EOS Q, solid lines) and for a much higher initial energy density (initial temperature at the fireball center = 2 GeV) with a massless ideal gas equation of state (EOS I, dashed lines).<sup>73</sup> The initial spatial asymmetry at this impact parameter is  $\epsilon_x(\tau_{\text{equ}})=0.27$ , and obviously  $\epsilon_p(\tau_{\text{equ}})=0$  since the fluid is initially at rest in the transverse plane. The spatial eccentricity is seen to disappear before the fireball matter freezes out, in particular for the case with the very high initial temperature (dashed lines) where the source is seen to switch orientation after about 6 fm/c and becomes in-plane-elongated at late times.<sup>74</sup> One also sees that the momentum anisotropy  $\epsilon_p$  saturates at about the same time when the spatial eccentricity  $\epsilon_x$  vanishes. All of the momentum anisotropy is built up during the first 6 fm/c.

Near a phase transition (in particular a first order transition) the equation of state becomes very soft, and this inhibits the generation of transverse flow. This also affects the generation of transverse flow *anisotropies* as seen from the solid curves in Figure 9: The rapid initial rise of  $\epsilon_p$  suddenly stops as a significant fraction of the fireball matter enters the mixed phase. It then even decreases somewhat as the system expands radially without further acceleration, thereby becoming more isotropic in both coordinate and momentum space. Only after the phase transition is complete and pressure gradients reappear, the system reacts to the remaining spatial eccentricity by a slight further increase of the momentum anisotropy. The softness of the equation of state near the phase transition thus focusses the generation of anisotropic flow to even earlier times, when the system is still entirely partonic and has not even begun to hadronize. At RHIC energies this means that almost all of the finally observed elliptic flow is created during the first 3-4 fm/c of the collision and reflects the hard QGP equation of state of an ideal gas of massless particles ( $c_s^2 = \frac{1}{3}$ ).<sup>4</sup> Microscopic kinetic studies of the evolution of elliptic flow lead to similar estimates for this time scale.<sup>75,76,77,78</sup>

We close this Section with a beautiful example of elliptic flow from outside the field of heavy-ion physics where the hydrodynamically predicted spatial expansion pattern shown in Figure 8 has for the first time been directly observed experimentally:<sup>26</sup> Figure 10 shows absorption images of an ensemble of about 200,000  ${}^6\text{Li}$  atoms which were captured and cooled to ultralow temperatures in a  $\text{CO}_2$  laser trap and then suddenly released by turning off the laser. The trap is highly anisotropic, creating a pencil-like initial spatial distribution with an aspect ratio of about 29 between the length and diameter of the pencil. The interaction strength among the fermionic atoms can be tuned with an external magnetic field by exploiting a Feshbach resonance. The pictures shown in Figure 10 correspond to the case of very strong interactions. The right panels in Figure 10 show that the fermion gas expands in the initially short (“transverse”) direction much more rapidly than along the axis of the pencil. As argued in the paper,<sup>26</sup> the measured expansion rates in either direction are consistent with hydrodynamic calculations.<sup>27</sup> At late times the gas evolves into a pancake oriented perpendicular to the pencil axis. The aspect ratio passes through 1 (i.e.  $\epsilon_x = 0$ ) about 600  $\mu\text{s}$  after release and continues to follow the hydrodynamic predictions to about 800  $\mu\text{s}$  after release. At later times it continues to grow, but more slowly than predicted by hydrodynamics, perhaps indicating a gradual breakdown of local thermal equilibrium due to increasing

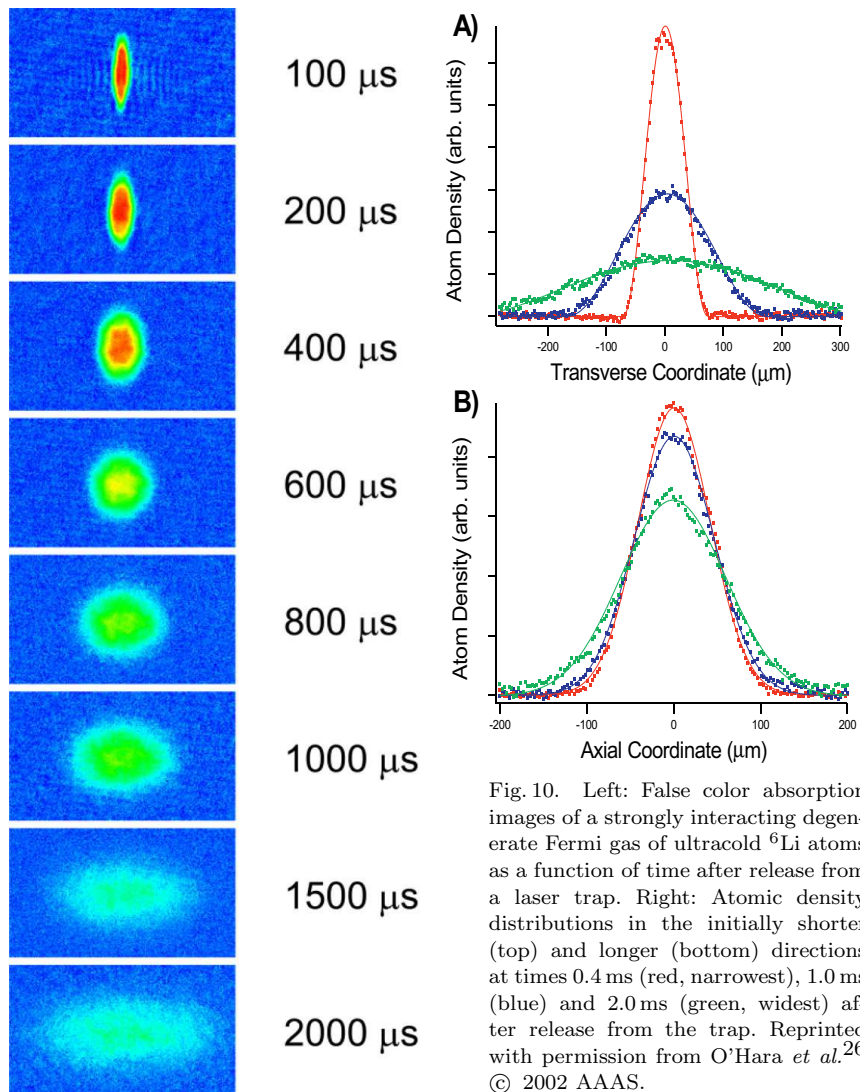


Fig. 10. Left: False color absorption images of a strongly interacting degenerate Fermi gas of ultracold  ${}^6\text{Li}$  atoms as a function of time after release from a laser trap. Right: Atomic density distributions in the initially shorter (top) and longer (bottom) directions at times 0.4 ms (red, narrowest), 1.0 ms (blue) and 2.0 ms (green, widest) after release from the trap. Reprinted with permission from O'Hara. *et al.*<sup>26</sup> © 2002 AAAS.

dilution. The authors of the paper<sup>26</sup> argue that, although the scattering among the fermions is very strong by design, it does not seem to be enough to ensure rapid local thermalization, and that sufficiently fast healing of deviations from local equilibrium caused by the collective expansion might require the fermions to be in a *superfluid* state.

#### 4. Experimental observables

Unfortunately, the small size and short lifetime prohibits a similar direct observation of the spatial evolution of the fireball in heavy-ion collisions. Only the momenta of the emitted particles are directly experimentally accessible, and spatial information must be extracted somewhat indirectly using *momentum correlations*. In the present Section we discuss measurements from Au+Au collisions at RHIC and compare them with hydrodynamic calculations. Most of the available published data stem from the first RHIC run at  $\sqrt{s} = 130 \text{ A GeV}$ , but a few selected preliminary data from the 200 A GeV run in the second year will also be studied. Occasionally comparison will be made with SPS data from Pb+Pb collisions at  $\sqrt{s} = 17 \text{ A GeV}$ .

This Section is subdivided into two major parts: In Section 4.1 we discuss single-particle momentum spectra, first averaged over the azimuthal emission angle and later analyzed for their anisotropies around the reaction plane. These data provide a complete characterization of the momentum-space structure of the fireball at freeze-out. In particular the analysis of momentum anisotropies yields a strong argument for rapid thermalization in heavy-ion collisions and for the creation of a quark-gluon plasma.

In the second part, Section 4.2, we discuss the extraction of coordinate-space information about the fireball at freeze-out from Bose-Einstein interferometry which exploits quantum statistical two-particle momentum correlations between pairs of identical bosons. The general framework of this method is discussed in the accompanying article by Tomášik and Wiedemann.<sup>79</sup> Here we will discuss specific aspects of Bose-Einstein correlations from hydrodynamic calculations, in particular their dependence on the azimuthal emission angle relative to the reaction plane and its implications for the degree of spatial deformation of the fireball at freeze-out.

##### 4.1. Momentum space observables

The primary observables in heavy-ion collisions are the triple-differential momentum distributions of identified hadrons  $i$  as a function of collision centrality (impact parameter  $b$ ):

$$\frac{dN_i}{p_T dp_T dy d\varphi_p}(b) = \frac{1}{2\pi} \frac{dN_i}{p_T dp_T dy}(b) \left( 1 + 2 v_2^i(p_T, b) \cos(2\varphi_p) + \dots \right). \quad (23)$$

We have expanded the dependence on the azimuthal emission angle  $\varphi_p$  relative to the reaction plane into a Fourier series.<sup>80</sup> Due to reflection symmetry with respect to the reaction plane, only cosine terms appear

in the expansion. As explained before, we restrict our attention to midrapidity,  $y = \ln[(E+p_z)/(E-p_z)] = 0$ , where all odd harmonics (in particular the *directed flow* coefficient  $v_1^i$ ) vanish. Accordingly, we have also dropped the  $y$ -dependence of the *elliptic flow* coefficient  $v_2^i$  but kept its dependence on transverse momentum and impact parameter. Hydrodynamic calculations<sup>24</sup> predict the next higher order coefficient  $v_4^i$  to be very small (< 0.1%), and up to now it has not been measured at RHIC. The spectra and flow coefficients depend on the hadron species  $i$  via the rest mass  $m_i$ , and this will be seen to play a crucial role.

As already mentioned, the parameters of the hydrodynamic model are fixed by reproducing the measured centrality dependence of the total charged multiplicity  $dN_{\text{ch}}/dy$  as well as the shape of the pion and proton spectra in central collisions at midrapidity (see below). The shapes of other hadron spectra, their centrality dependence and the dependence of the elliptic flow coefficient  $v_2^i$  on  $p_T$ , centrality and hadron species  $i$  are then all parameter free predictions of the model.<sup>81</sup> The same holds for all two-particle momentum correlations.<sup>13,14,74</sup> These predictions will be compared with experiment and used to test the hydrodynamic approach and to extract physical information from its successes and failures.

#### 4.1.1. Single particle spectra

The free parameters of the hydrodynamic model are the starting (thermalization) time  $\tau_{\text{equ}}$ , the entropy and net baryon density in the center of the reaction zone at this time, and the freeze-out energy density  $e_{\text{dec}}$ . The corresponding quantities at other fireball points at  $\tau_{\text{equ}}$  are then determined by the Glauber profiles discussed in Sec. 2.4 (see discussion below Fig. 2). The ratio of net baryon to entropy density is fixed by the measured proton/pion ratio. Since the measured chemical composition of the final state at RHIC was found<sup>82</sup> to accurately reflect a hadron resonance gas in chemical equilibrium at the hadronization phase transition, we require the hydrodynamic model to reproduce this  $p/\pi$  ratio on a hypersurface of temperature  $T_{\text{crit}}$ . By entropy conservation, the final total charged multiplicity  $dN_{\text{ch}}/dy$  fixes the initial product  $(s \cdot \tau)_{\text{equ}}$ .<sup>24,62,70</sup> The value of  $\tau_{\text{equ}}$  controls how much transverse flow can be generated until freeze-out. Since the thermal motion and radial flow affect light and heavy particles differently at low  $p_T$ ,<sup>67,83</sup> a simultaneous fit of the final pion and proton spectra separates the radial flow from the thermal component. The final flow strength then fixes  $\tau_{\text{equ}}$  whereas the freeze-out temperature determines the energy density  $e_{\text{dec}}$  at

decoupling.

The top left panel of Fig. 11 shows the hydrodynamic fit<sup>14</sup> to the transverse momentum spectra of positive pions and antiprotons, as measured by the PHENIX and STAR collaborations in central ( $b=0$ ) Au+Au collisions at  $\sqrt{s}=130$  A GeV.<sup>84,85,86</sup> The fit yields an initial central entropy density  $s_{\text{equ}}=95$  fm<sup>-3</sup> at an equilibration time  $\tau_{\text{equ}}=0.6$  fm. This corresponds to an initial temperature of  $T_{\text{equ}}=340$  MeV and an initial energy density  $e=25$  GeV/fm<sup>3</sup> in the fireball center. (Note that these parameters satisfy the “uncertainty relation”  $\tau_{\text{equ}} \cdot T_{\text{equ}} \approx 1$ .) Freeze-out was implemented on a hypersurface of constant energy density with  $e_{\text{dec}}=0.075$  GeV/fm<sup>3</sup>.

$\sqrt{s_{\text{NN}}}$ (GeV)	SPS	RHIC 1	RHIC 2
$s_{\text{equ}}$ (fm <sup>-3</sup> )	43	95	110
$T_{\text{equ}}$ (MeV)	257	340	360
$\tau_{\text{equ}}$ (fm/c)	0.8	0.6	0.6

Table 1. Initial conditions for SPS and RHIC energies used to fit the particle spectra from central Pb+Pb or Au+Au collisions.  $s_{\text{equ}}$  and  $T_{\text{equ}}$  refer to the maximum values at  $\tau_{\text{equ}}$  in the fireball center.

The fit in the top left panel of Fig. 11 was performed with a chemical equilibrium equation of state. Use of such an equation of state implicitly assumes that even below the hadronization temperature  $T_{\text{crit}}$  chemical equilibrium among the different hadron species can be maintained all the way down to kinetic freeze-out. With such an equation of state the decoupling energy  $e_{\text{dec}}=0.075$  GeV/fm<sup>3</sup> translates into a kinetic freeze-out temperature of  $T_{\text{dec}} \approx 130$  MeV. The data, on the other hand, show<sup>82</sup> that the hadron abundances freeze out at  $T_{\text{chem}} \approx T_{\text{crit}}$ , i.e. already when hadrons first coalesce from the expanding quark-gluon soup the inelastic processes which could transform different hadron species into each other are too slow to keep up with the expansion. The measured  $\bar{p}/\pi$  ratio thus does not agree with the one computed from the chemical equilibrium equation of state at the kinetic freeze-out temperature  $T_{\text{dec}}=130$  MeV, and the latter must be rescaled by hand if one wants to reproduce not only the shape, but also the correct normalization of the measured spectra in Fig. 11.

A better procedure would be to use a chemical non-equilibrium equation of state for the hadronic phase<sup>87,88,89</sup> in which for temperatures  $T$  below  $T_{\text{chem}}$  the chemical potentials for each hadronic species are readjusted in such a way that their total abundances (after decay of unstable resonances)

are kept constant at the observed values. This approach has recently been applied<sup>65</sup> to newer RHIC data at  $\sqrt{s} = 200$  A GeV and will be discussed below.

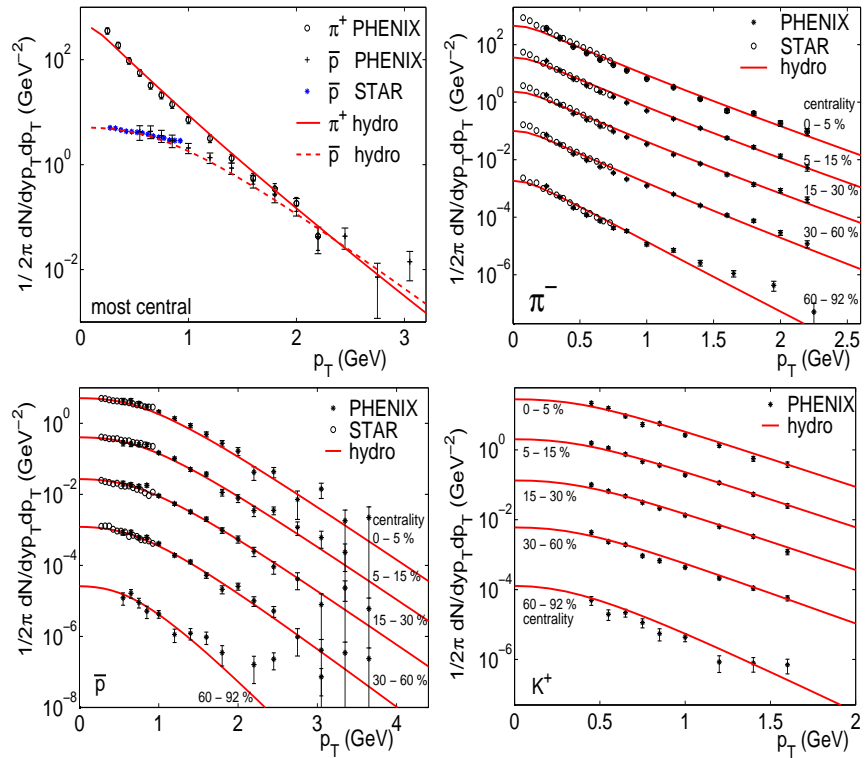


Fig. 11. Identified pion, antiproton and kaon spectra for  $\sqrt{s_{NN}} = 130$  GeV from the PHENIX<sup>84,91</sup> and STAR<sup>85,86</sup> collaborations in comparison with results from a hydrodynamic calculation.<sup>14</sup> The top left panel shows pion and (anti-)proton spectra from central collisions. Shown in the other panels are spectra of five different centralities: from most central (top) to the most peripheral (bottom). The spectra are successively scaled by a factor 0.1 for clarity.

For a single hadron species, the shape of the transverse momentum spectrum allows combinations of temperature and radial flow which are strongly anticorrelated.<sup>67</sup> By using two hadron species with significantly different masses this anticorrelation is strongly reduced albeit not completely eliminated. Consequently, the above procedure still leaves open a small range of possible variations for the extracted initial and final parameters. Within this range, we selected a value for  $\tau_{\text{equ}}$  which is, if anything, on the large

side; some of the hadron spectra would be fit slightly better with even smaller values for  $\tau_{\text{equ}}$  or a non-zero transverse flow velocity already at  $\tau_{\text{equ}}$  (see below). Table 1 summarizes the initial conditions applied in our hydrodynamic studies at SPS,<sup>24,90</sup> RHIC1<sup>13,23,46,81</sup> and RHIC2<sup>65</sup> energies.

Once the parameters have been fixed in central collisions, spectra at other centralities and for different hadron species can be predicted without introducing additional parameters. The remaining three panels of Fig. 11 show the transverse momentum spectra of pions, kaons and antiprotons in five different centrality bins as observed by the PHENIX<sup>84,91</sup> and STAR<sup>85,86</sup> collaborations. For all centrality classes, except the most peripheral one, the hydrodynamic predictions (solid lines) agree pretty well with the data. The kaon spectra are reproduced almost perfectly, but for pions the model consistently underpredicts the data at low  $p_{\text{T}}$ . This has now been understood to be largely an artifact of having employed in these calculations a chemical equilibrium equation of state all the way down to kinetic freeze-out. More recent calculations<sup>65</sup> with a chemical non-equilibrium equation of state, to be compared to  $\sqrt{s} = 200 \text{ A GeV}$  data below, show that, as the system cools below the chemical freeze-out point  $T_{\text{chem}} \approx T_{\text{crit}}$ , a significant positive pion chemical potential builds up, emphasizing the concave curvature of the spectrum from Bose effects and increasing the feeddown corrections from heavier resonances at low  $p_{\text{T}}$ . The inclusion of non-equilibrium baryon chemical potentials to avoid baryon-antibaryon annihilation further amplifies the resonance feeddown for pions.

Significant discrepancies are also seen at large impact parameters and large transverse momenta  $p_{\text{T}} \gtrsim 2.5 \text{ GeV}/c$ . This is not surprising since high- $p_{\text{T}}$  particles require more rescatterings to thermalize and escape from the fireball before doing so. This is in particular true in more peripheral collisions where the reaction zone is smaller.

For the calculations shown in Fig. 11 the same value  $e_{\text{dec}}$  was used for all impact parameters. Phenomenological studies<sup>92</sup> using a hydrodynamically motivated parametrization<sup>67</sup> to describe pion and antiproton spectra from 200 A GeV Au+Au collisions in a large number of centrality bins indicate somewhat earlier freeze-out, at higher temperature and with less transverse flow, in the most peripheral collisions (see Fig. 12). In the hydrodynamic model this can be accommodated by allowing the freeze-out energy density  $e_{\text{dec}}$  to increase with impact parameter. A consistent determination of  $e_{\text{dec}}$  from the kinetic decoupling criterion is expected to automatically yield such a behavior. Such a calculation would use the fitted value for  $e_{\text{dec}}$  extracted from central collision data to determine the unknown proportionality con-

stant between the local expansion and scattering time scales at decoupling (see discussion in Secs. 2.5 and 3.1), and then calculate  $e_{\text{dec}}$  for other impact parameters by using the kinetic freeze-out criterion  $\tau_{\text{exp}} = \kappa \tau_{\text{scatt}}$  with the *same* constant  $\kappa$  extracted from central collisions. So far this has not been done, though.

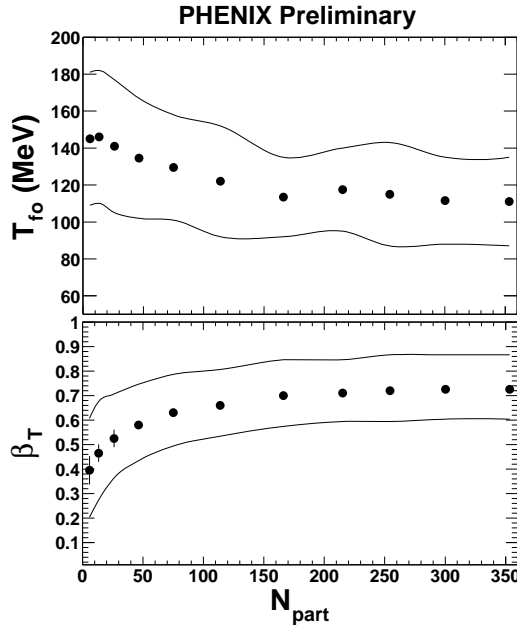


Fig. 12. Kinetic freeze-out temperature  $T_{\text{fo}} = T_{\text{dec}}$  and transverse flow velocity  $\beta_T$  at the fireball edge, extracted from a simultaneous fit of a flow spectrum parametrization<sup>67</sup> to  $\pi^\pm$ ,  $K^\pm$ ,  $p$  and  $\bar{p}$  spectra from 200 A GeV Au+Au collisions over the entire range of collision centralities.<sup>92</sup> More peripheral collisions (small numbers  $N_{\text{part}}$  of participating nucleons) are seen to decouple earlier, at higher freeze-out temperature and with less transverse flow.

Without transverse flow, thermal spectra exhibit  $m_T$ -scaling<sup>35</sup>, i.e. after appropriate rescaling of the yields all spectra collapse onto a single curve. Transverse collective flow breaks this scaling at low  $p_T \lesssim m_0$  (i.e. for non-relativistic transverse particle velocities) by an amount which increases with the particle rest mass  $m_0$ .<sup>68,83,93</sup> When plotting the spectra against  $p_T$  instead of  $m_T$ , any breaking of  $m_T$ -scaling is at least partially masked by a kinematic effect at low  $p_T$  which unfortunately again increases with the rest mass  $m_0$ . To visualize the effects of transverse flow on the spectral shape thus requires plotting the spectrum logarithmically as a function of  $m_T$  or  $m_T - m_0$ . Such plots can be found in recent experimental publications,<sup>94,95,96</sup> and although the viewer's eye is often misled by superimposed straight exponential lines  $\sim e^{-m_T/T_{\text{eff}}}$ , a second glance shows a clear tendency of the heavier hadron spectra to curve and to begin to develop a shoulder at low transverse kinetic energy  $m_T - m_0$ , as expected

from transverse flow.

One such example is shown in Fig. 13 where preliminary spectra of  $\Omega$  hyperons<sup>97</sup> are compared with hydrodynamic predictions. For this comparison the original calculations for 130  $A$  GeV Au+Au collisions<sup>81</sup> were repeated with RHIC2 initial conditions and a chemical non-equilibrium equation of state in the hadronic phase.<sup>65</sup> The solid lines are based on de-

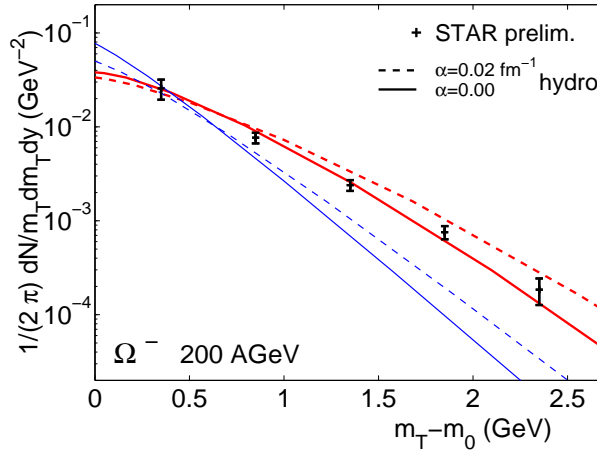


Fig. 13. Transverse mass spectrum of  $\Omega$  hyperons from central 200  $A$  GeV Au+Au collisions at RHIC.<sup>97</sup> The curves are hydrodynamic calculations with different initial and freeze-out conditions: Solid lines correspond to the default of no initial transverse flow at  $\tau_{\text{equ}}$ , dashed lines assume a small but non-zero radial flow,  $v_r = \tanh(\alpha r)$  with  $\alpha = 0.02 \text{ fm}^{-1}$ , already at  $\tau_{\text{equ}}$ . The lower (thin) set of curves assumes  $\Omega$ -decoupling at  $T_{\text{crit}} = 164 \text{ MeV}$ , the upper (thick) set of curves decouples the  $\Omega$  together with the pions and protons at  $T_{\text{dec}} = 100 \text{ MeV}$ .<sup>65</sup>

fault parameters (see Table 4.1.1) without any initial transverse flow at  $\tau_{\text{equ}}$ . (The dashed lines will be discussed further below.) Following a suggestion that  $\Omega$  hyperons, being heavy and not having any known strong coupling resonances with pions, should not be able to participate in any increase of the radial flow during the hadronic phase and thus decouple early,<sup>98</sup> we show two solid lines, the steeper one corresponding to decoupling at  $e_{\text{dec}} = 0.45 \text{ GeV/fm}^3$ , i.e. directly after hadronization at  $T_{\text{crit}}$ , whereas the flatter one assumes decoupling together with pions and other hadrons at  $e_{\text{dec}} = 0.075 \text{ GeV/fm}^3$ . The data clearly favor the flatter curve, suggesting intense rescattering of the  $\Omega$ 's in the hadronic phase. The microscopic mechanism for this rescattering is still unclear. However, without hadronic rescattering the hydrodynamic model, in spite of its perfect local thermalization

during the early expansion stages, is unable to generate enough transverse flow to flatten the  $\Omega$  spectra as much as required by the data. Partonic hydrodynamic flow alone can not explain the  $\Omega$  spectrum.

We close this subsection with a comparison of pion, kaon and hadron spectra from 200 A GeV Au+Au collisions (RHIC2) with recent hydrodynamic calculations which correctly implement chemical decoupling at  $T_{\text{crit}}$ . Figure 14 shows a compilation of preliminary spectra from the four RHIC collaborations.<sup>99,100,101,102</sup> For better visibility, the  $\pi^-$ ,  $K^-$  and  $\bar{p}$  spectra are separated artificially by scaling factors of 10 and 100, respectively. The lines reflect hydrodynamic results in these calculations the particle num-

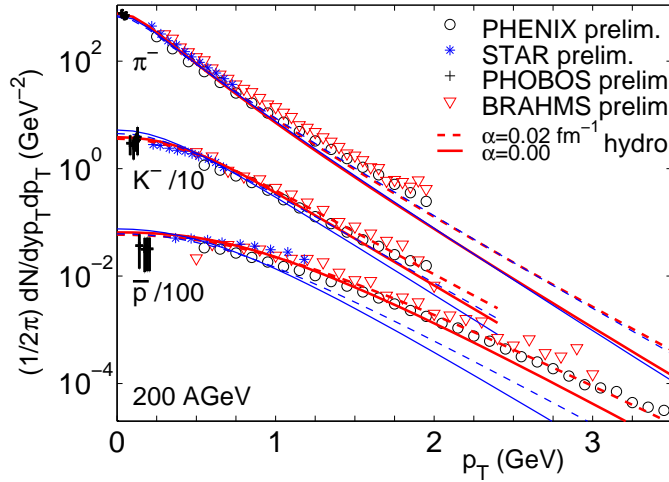


Fig. 14. Particle spectra of  $\pi^-$ ,  $K^-$  and antiprotons at  $\sqrt{s_{\text{NN}}} = 200$  GeV as measured by the four large experiments at RHIC.<sup>99,100,101,102</sup> The lines show hydrodynamic results under various considerations (see text).<sup>65</sup>

bers of all stable hadron species were conserved throughout the hadronic resonance gas phase of the evolution, by introducing appropriate chemical potentials.<sup>87,88,89</sup> It turns out that such a chemical non-equilibrium equation of state has almost the same relation  $p(e)$  between the pressure and energy density as the equilibrium one, and that the hydrodynamical evolution remains almost unaltered.<sup>87,89</sup> However, the relation between the decoupling energy density  $e_{\text{dec}}$  and the freeze-out temperature  $T_{\text{dec}}$  changes significantly, since the non-equilibrium equation of state prohibits the annihilation of baryon-antibaryon pairs as the temperature drops. Consequently, at any given temperature below  $T_{\text{chem}}$  the non-equilibrium equation of state

contains more heavy baryons and antibaryons than the equilibrium one and thus has a higher energy density.

The same energy density  $e_{\text{dec}} = 0.075 \text{ GeV/fm}^3$  then translates into a significantly lower freeze-out temperature  $T_{\text{dec}} \approx 100 \text{ MeV}$ .<sup>87,89,65</sup> The corresponding results are given as thick solid (red) lines in Fig. 14. The thin solid (blue) lines in the Figure, shown for comparison, were calculated by assuming kinetic freeze-out already at hadronization,  $T_{\text{crit}} = 165 \text{ MeV}$ . The data clearly favor the additional radial boost resulting from the continued buildup of radial flow in the hadronic phase. Still, even at  $e_{\text{dec}} = 0.075 \text{ GeV/fm}^3$ , the spectra are still steeper than the data and the previous calculations with a chemical equilibrium equation of state shown in Fig. 11, reflecting the combination of the same flow pattern with a lower freeze-out temperature. Somewhat unexpectedly, the authors of the study<sup>65</sup> were unable to significantly improve the situation by reducing  $e_{\text{dec}}$  even further: The effects of a larger radial flow at lower  $e_{\text{dec}}$  were almost completely compensated by the accompanying lower freeze-out temperature, leading to only modest improvements for kaons and protons and almost none for the pions.

This motivated the authors<sup>65</sup> to introduce a small but non-vanishing transverse “seed” velocity already at the beginning of the hydrodynamic stage. The dashed lines in Fig. 14 (and also earlier in Fig. 13) show hydrodynamic calculations with an initial transverse flow velocity profile given by  $v_r(r, \tau_{\text{equ}}) = \tanh(\alpha r)$  with  $\alpha = 0.02 \text{ fm}^{-1}$ . This initial transverse kick is seen to significantly improve the agreement with the pion, kaon and antiproton data up to  $p_T \gtrsim 1.5 - 2 \text{ GeV}/c$  for pions and kaons and up to  $p_T \gtrsim 3.5 \text{ GeV}/c$  for (anti)protons.<sup>65</sup> It can be motivated by invoking some collective (although not ideal hydrodynamic) transverse motion of the fireball already during the initial thermalization stage, although the magnitude of the parameter  $\alpha$  requires further study.

In Figure 14 the kaon and antiproton spectra were divided by factors of 10 and 100, respectively, for better visibility. If this is not done one notices that the antiproton spectrum crosses the pion spectrum at around  $p_T \sim 2 - 2.5 \text{ GeV}/c$ ,<sup>91,99</sup> i.e. at larger  $p_T$  antiprotons are more abundant than pions! This became known as the “ $\bar{p}/\pi^- > 1$  anomaly” and has attracted significant attention.<sup>103</sup> Here the word “anomaly” arises from a comparison of this ratio in central Au+Au with  $pp$  collisions and with string fragmentation models which both give  $\bar{p}/\pi^-$  ratios much below 1. However, in Au+Au collisions string fragmentation is expected to explain hadron production only at rather large  $p_T$ ,<sup>104</sup> and in the hydrodynamic picture which

is successful at  $p_T \lesssim 2 \text{ GeV}/c$  there is actually nothing anomalous about a  $\bar{p}/\pi$  ratio that exceeds 1.

To see this let us first look at a thermal system without flow. The corresponding transverse mass spectra are in good approximation simple exponentials in  $\frac{m_T}{T}$  whose ratios at fixed  $m_T$  are simply given by the ratios  $(g_{\bar{p}}/g_{\pi})e^{(\mu_{\bar{p}}-\mu_{\pi})/T}$  of their spin-isospin degeneracies and fugacities. For sufficiently large  $p_T \gg m_p$ ,  $m_T \approx p_T$  and the same holds true for the ratio of the  $p_T$ -spectra at fixed  $p_T$ . It still holds true in the presence of transverse flow which, at sufficiently large  $p_T$ , simply flattens all  $m_T$ -slopes by a common blueshift factor<sup>67,83,93</sup>  $\sqrt{\frac{1+v_r}{1-v_r}}$ . Since antiprotons have a 2-fold spin degeneracy and pions have none, we see that the asymptotic hydrodynamic  $\bar{p}/\pi$  ratio is above unity if the chemical potentials are sufficiently small.

$T$	$\mu_p$	$\mu_{\bar{p}}$	$\mu_{\pi}$	$\mu_{K^+}$
164 MeV	29 MeV	-29 MeV	0	0
100 MeV	379 MeV	344 MeV	81 MeV	167 MeV
$T$	$\bar{p}/p$	$(p/\pi^+)_\infty$	$(\bar{p}/\pi^-)_\infty$	$(K^+/\pi^+)_\infty$
164 MeV	0.7	2.4	1.7	1.0
100 MeV	0.7	40	28	2.4

Table 2. Upper part: Chemical potentials of protons, antiprotons, pions and kaons at the chemical (164 MeV) and kinetic (100 MeV) freeze-out temperatures for 200  $A \text{ GeV}$  Au+Au collisions.<sup>65</sup> Lower part: Asymptotic particle ratios for these hadrons at fixed large  $p_T$ , for two assumed hydrodynamic freeze-out temperatures of 164 and 100 MeV, respectively (see text).

In Au+Au collisions at  $\sqrt{s_{\text{NN}}} = 200 \text{ GeV}$  the baryon chemical potential at chemical freeze-out is small<sup>82</sup> (29 MeV) and the pion chemical potential vanishes. Correspondingly, the asymptotic  $p/\pi^+$  and  $\bar{p}/\pi^-$  ratios are both close to 2 (see Table 2). As the system cools below the chemical freeze-out temperature, however, pions, kaons and both protons and antiprotons all develop significant positive chemical potentials which are necessary to keep their total abundances (after unstable resonance decays) fixed at their chemical freeze-out values<sup>88</sup> (second row in Table 2). As a consequence, the asymptotic  $p/\pi$  and  $\bar{p}/\pi$  ratios increase dramatically, to 40 and 28, respectively, and even the asymptotic  $K^+/\pi^+$  ratio increases from 1 to 2.4.

We see that cooling at constant particle numbers strongly depletes the pions at high  $p_T$  in favor of high- $p_T$  baryons and kaons. Correspondingly, the ratios of the hydrodynamic spectra, shown in Fig. 15, rise far above

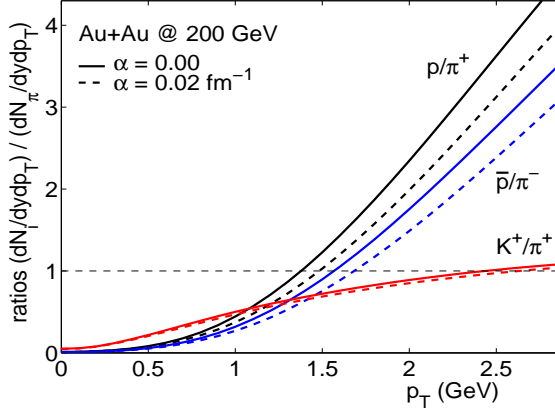


Fig. 15. Hydrodynamic predictions for the midrapidity ratios of  $p/\pi^+$ ,  $\bar{p}/\pi^-$ , and  $K^+/\pi^+$  as functions of  $p_T$  for 200 A GeV Au+Au collisions, extracted from the top pairs of curves shown in Fig. 14 (see description in text).

unity at large  $p_T$ . We should stress that the increase with  $p_T$  of these ratios at small  $p_T$  is generic for thermalized spectra and independent of whether or not there is radial flow. It is a simple kinematic consequence of replotted two approximately parallel exponentials (more exactly:  $K_2$ -functions) in  $m_T$  as functions of  $p_T$  and taking the ratio. Due to the larger rest mass the  $p_T$ -spectrum of the heavier particle is flattened more strongly at low  $p_T$  than that of the lighter particle, yielding for their ratio a rising function of  $p_T$ . The additional flattening from radial flow, which again affects the heavier particles more strongly than the light ones, further increases this tendency.

It is worth pointing out that a  $\bar{p}/\pi$  ratio well above 2 and a  $K/\pi$  ratio well above 1, as hydrodynamically predicted for  $p_T > 2.5$  GeV/c (see Fig. 15) would, when taken together with the measured global thermal yields, provide a unique proof for chemical and kinetic decoupling happening at different temperatures. Unfortunately, as we will see in more detail later, hydrodynamics begins to seriously break down exactly in this interesting  $p_T$  domain, and the experimentally observed ratios<sup>99</sup> never appear to grow much beyond unity before decreasing again at even higher  $p_T$ , eventually perhaps approaching the small asymptotic values expected from jet fragmentation.<sup>104</sup>

#### 4.1.2. Mean transverse momentum and transverse energy

The good agreement of the hydrodynamic calculations with the experimental transverse momentum spectra is reflected in a similarly good description

of the measured average transverse momenta.<sup>72</sup> Figure 16 shows a comparison of  $\langle p_T \rangle$  for identified pions, kaons, protons and antiprotons measured by PHENIX in 200  $\text{A GeV}$  Au+Au collisions<sup>99,105</sup> with the hydrodynamic results.<sup>65</sup> The bands reflect the theoretical variation resulting from possible initial transverse flow already at the beginning of the hydrodynamic expansion stage, as discussed at the end of the previous subsection. The figure shows some discrepancies between hydrodynamics and the data for peripheral collisions (small  $N_{\text{part}}$ ) which are strongest for the kaons whose spectra are flatter at large impact parameters than predicted by the model.

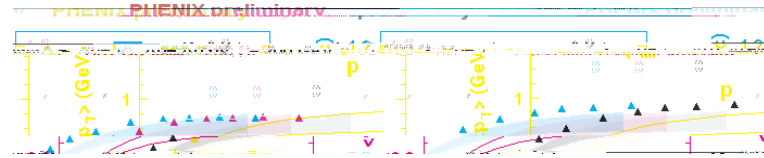


Fig. 16. Mean transverse momenta of pions, kaons and (anti)protons from 200  $\text{A GeV}$  Au+Au collisions.<sup>99,105</sup> Hydrodynamic results are included as bands whose lower ends reflect an initialization without initial transverse flow while the upper ends correspond to an initial transverse flow field  $v_r = \tanh(\alpha r)$  with  $\alpha = 0.02 \text{ fm}^{-1}$ .<sup>65</sup>

Figure 17 shows the total transverse energy per emitted charged hadron as a function of collision centrality. The data are from Pb+Pb collisions at the SPS<sup>106</sup> and Au+Au collisions at two RHIC energies.<sup>107,108</sup> Although both the charged particle multiplicity and total transverse energy vary strongly with the number of participating nucleons (and one or the other are therefore often used to determine the collision centrality), the transverse energy *per particle* is essentially independent of the centrality. It also depends only weakly on the collision energy.

The superimposed band in Figure 17 reflects hydrodynamic calculations for Au+Au collisions at  $\sqrt{s} = 200 \text{ A GeV}$  with and without initial transverse flow, as before. The slight rise of the theoretical curves with increasing  $N_{\text{part}}$

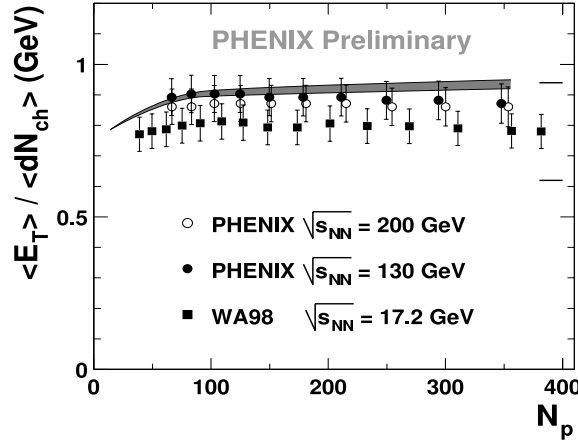


Fig. 17. Transverse energy per charged hadron as a function of collision centrality, for Au+Au and Pb+Pb collisions at three different beam energies.<sup>106,107,108</sup> Superimposed on the original experimental Figure<sup>108</sup> are hydrodynamic results for Au+Au collisions at  $\sqrt{s_{NN}} = 200 \text{ GeV}$ .<sup>65</sup> The lower end of the band results from an initialization without initial transverse flow, the upper end reflects an initial transverse flow field  $v_r = \tanh(\alpha r)$  with  $\alpha = 0.02 \text{ fm}^{-1}$ .

can be attributed to the larger average transverse flow developing in more central collisions, resulting from the higher initial energy density and the somewhat longer duration of the expansion until freeze-out.<sup>46</sup> Successful reproduction of the data requires a correct treatment of the chemical composition at freeze-out (by using a chemical non-equilibrium hadron equation of state below  $T_{\text{crit}}$ ). If one instead assumes chemical equilibrium of the hadron resonance gas down to kinetic freeze-out, hydrodynamics over-predicts the transverse energy per particle by about 15-20%.<sup>46</sup>

#### 4.1.3. Momentum anisotropies as early fireball signatures

In non-central nuclear collisions, or if the colliding nuclei are deformed, the nuclear overlap region is initially spatially deformed (see Fig. 3). Interactions among the constituents of the matter formed in that zone transfer this spatial deformation onto momentum space. Even if the fireball matter does not interact strongly enough to reach and maintain almost instantaneous local equilibrium, and a hydrodynamic description therefore fails, any kind of re-interaction among the fireball constituents will still be sensitive to the anisotropic density gradients in the reaction zone and thus redirect the momentum flow preferably into the direction of the strongest density gradients (i.e. in the “short” direction).<sup>75,76,78,109</sup> The result is a momentum-space anisotropy, with more momentum flowing into the reaction plane than out

of it.

Such a “momentum-space reflection” of the initial spatial deformation is a unique signature for re-interactions in the fireball and, when observed, proves that the fireball matter has undergone significant nontrivial dynamics between creation and freeze-out. Without rescattering, the only other mechanism with the ability to map a spatial deformation onto momentum space is the quantum mechanical uncertainty relation. For matter confined to smaller spatial dimensions in  $x$  than in  $y$  direction it predicts  $\Delta p_x > \Delta p_y$  for the corresponding widths of the momentum distribution. However, any momentum anisotropy resulting from this mechanism is restricted to momenta  $p \sim 1/(\text{size of the overlap zone})$  which for a typical fireball radius of a few fm translates into a fraction of  $200 \text{ MeV}/c$ . This is the likely mechanism for the momentum anisotropy observed<sup>110</sup> in calculations of the classical dynamical evolution of a postulated deformed “color glass condensate” created initially in the collision. Unlike the experimental data, this momentum anisotropy is concentrated around relatively low  $p_T$ .<sup>110</sup>

Whatever the detailed mechanism responsible for the observed momentum anisotropy, the induced faster motion into the reaction plane than perpendicular to it (“elliptic flow”) rapidly degrades the initial spatial deformation of the matter distribution and thus eliminates the driving force for any further increase of the anisotropic flow. Elliptic flow is therefore “self-quenching”,<sup>75,76</sup> and any flow anisotropy measured in the final state must have been generated early when the collision fireball was still spatially deformed (see Fig. 9). If elliptic flow does not develop early, it never develops at all (see also Sec. 4.1.4). It thus reflects the pressure and stiffness of the equation of state during the earliest collision stages,<sup>75,76,77,4,24</sup> but (in contrast to many other early fireball signatures) it can be easily measured with high statistical accuracy since it affects *all* final state particles.

Microscopic kinetic models show (see Fig. 19 below) that, for a given initial spatial deformation, the induced momentum space anisotropy is a monotonically rising function of the strength of the interaction among the matter constituents.<sup>77,78,109</sup> The maximum effect should thus be expected if their mean free path approaches zero, i.e. in the hydrodynamic limit.<sup>4,13</sup> Within this limit, we will see that the magnitude of the effect shows some sensitivity to the nuclear equation of state in the early collision stage, but the variation is not very large. This implies that, since the initial spatial deformation can be computed from the collision geometry (the average impact parameter can be determined, say, from the ratio of the observed multiplicity in the event to the maximum multiplicity from all events), the

observed magnitudes of the momentum anisotropies, and in particular their dependence on collision centrality,<sup>109,111</sup> provide valuable measures for the degree of thermalization reached early in the collision.

Experimentally this program was first pursued at the SPS in 158  $A$  GeV Pb+Pb collisions.<sup>112</sup> These data still showed significant sensitivity to details of the analysis procedure<sup>113</sup> and thus remained somewhat inconclusive.<sup>23</sup> Qualitatively, the SPS data (where the directed and elliptic flow coefficients,  $v_1$  and  $v_2$ , can both be measured) confirmed Ollitrault's 1992 prediction<sup>70</sup> that near midrapidity the preferred flow direction is *into* the reaction plane, supporting the conclusions from earlier measurements in Au+Au collisions at the AGS<sup>114</sup> where a transition from out-of-plane to in-plane elliptic flow had been found between 4 and 6  $A$  GeV beam energy. A comprehensive quantitative discussion of elliptic flow became first possible with RHIC data, because of their better statistics and improved event plane resolution (due to the larger event multiplicities) and also as a result of improved<sup>111</sup> analysis techniques.<sup>a</sup> In the meantime the latter have also been re-applied to SPS data and produced very detailed results from Pb+Pb collisions at this lower beam energy.<sup>122,123</sup>

#### 4.1.4. Elliptic flow at RHIC

The second published and still among the most important results from Au+Au collisions at RHIC was the centrality and  $p_T$  dependence of the elliptic flow coefficient at midrapidity.<sup>124</sup> For central to midperipheral collisions and for transverse momenta  $p_T \lesssim 1.5$  GeV/ $c$  the data were found to be in stunning agreement with hydrodynamic predictions,<sup>4,23</sup> as seen in Fig. 18. In the left panel, the ratio  $n_{\text{ch}}/n_{\text{max}}$  of the charged particle multiplicity to the maximum observed value is used to characterize the collision centrality, with the most central collisions towards the right near 1.  $n_{\text{ch}}/n_{\text{max}} = 0.45$  corresponds to an impact parameter  $b \approx 7$  fm.<sup>121</sup> Up to this value the observed elliptic flow  $v_2$  is found to track very well the increasing initial spatial deformation  $\epsilon_x$  of the nuclear overlap zone,<sup>121</sup> as

<sup>a</sup>One of the important experimental issues is the separation<sup>115,116</sup> of collective “flow” contributions to the observed momentum anisotropies from “non-flow” angular correlations, such as Bose-Einstein correlations,<sup>117</sup> correlations arising from momentum conservation,<sup>118,119</sup> and two-particle momentum correlations from resonance decays and jet production.<sup>120</sup> Many of the data shown in this review have not yet been corrected for non-flow contributions, but subsequent analysis<sup>121</sup> has shown that for the RHIC data and in the  $p_T$ -range of interest for this review these corrections are small ( $\lesssim 15\%$ ).

predicted by hydrodynamics.<sup>4</sup>

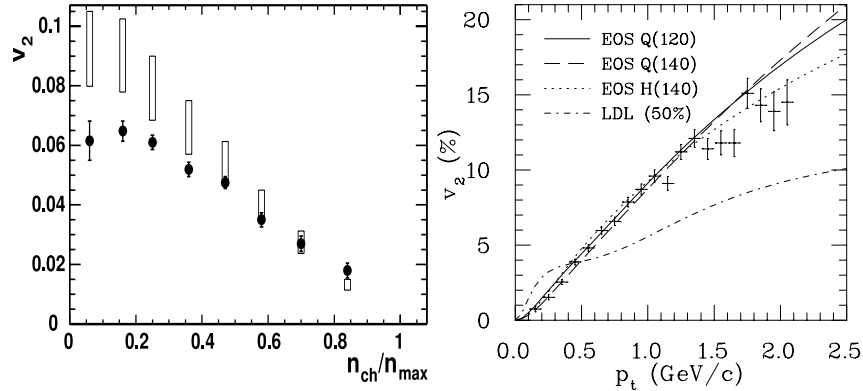


Fig. 18. Elliptic flow of unidentified charged particles in 130 A GeV Au+Au collisions, integrated over  $p_T$  as function of centrality (left) and for minimum bias collisions as a function of  $p_T$  (right). Both data sets (symbols with error bars) are from the original STAR publication.<sup>124</sup> The vertical bars in the left panel<sup>124</sup> indicate the range of earlier hydrodynamic predictions for a variety of equations of state and initial conditions.<sup>4</sup> The top three curves in the right panel<sup>23</sup> represent hydrodynamic predictions for semiperipheral collisions with initial conditions tuned to the observed<sup>48</sup> total charged multiplicity in central collisions where  $v_2$  vanishes. Different curves correspond to different equations of state and freeze-out temperatures.<sup>23</sup>

Following this discovery it soon became clear that the agreement of the data with the hydrodynamic calculations could not be accidental and in fact allows to draw a number of very strong and important conclusions. These conclusions refer to soft particle production, that is to mesons with transverse momenta up to about 1.5 GeV/c and baryons with  $p_T \lesssim 2.5$  GeV/c. This momentum range covers well over 99% of the produced particles. This means that we are talking about the global dynamical features of the bulk of the fireball matter. Of course, the small fraction of particles emitted with larger transverse momenta carry very important information themselves, but their behavior is not expected to be controlled by hydrodynamics in the first place, and they are not the subject of our discussion here. It should be noted, however, that interpreting the behavior of high- $p_T$  particles does require a prior understanding of the global fireball dynamics which *is* the subject of this review. In the following we discuss the aforementioned conclusions, as well as a number of additional theoretical and experimental aspects.

*Strong rescattering:*

It was quickly realized<sup>78</sup> that the measured<sup>124</sup> almost linear rise of the charged particle (i.e. predominantly pionic) elliptic flow with  $p_T$  requires strong rescattering among the fireball constituents. Figure 19 shows the results from microscopic simulations which describe the dynamics of the early expansion stage by solving a Boltzmann equation for colliding on-shell partons.<sup>78</sup> The different curves are parametrized by the transport opacity  $\xi = \sigma_0 dN_g/d\eta$  involving the product of the parton rapidity density and cross section in the early collision stage. As the opacity is increased, the elliptic flow is seen to approach the data (and the hydrodynamic limit) monotonically *from below*. Whereas the hydrodynamic limit predicts a continuous rise of  $v_2(p_T)$ , the elliptic flow from the parton cascade saturates at high  $p_T$ , as also seen in the data<sup>125</sup> (see Fig. 26 below). This is due to incomplete equilibration at high  $p_T$ : the critical  $p_T$  at which the cascade results cease to follow the hydrodynamic rise shifts to higher (lower) values as the transport opacity is increased (decreased).

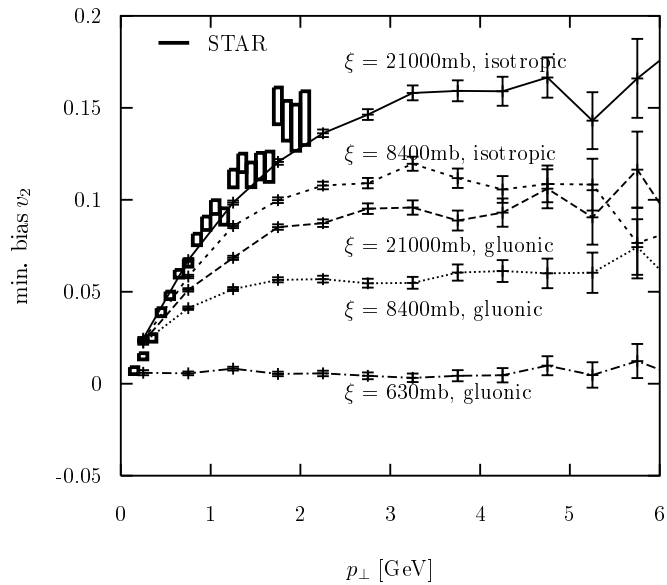


Fig. 19. Impact parameter averaged elliptic flow as a function of transverse momentum. The experimental data points from STAR<sup>124</sup> are compared with parton cascade calculations<sup>78</sup> with varying transport opacities  $\xi$ . Figure taken from Molnar and Gyulassy.<sup>78</sup>

It is interesting to observe that stronger rescattering manifests itself

in this way, i.e. by following the hydrodynamic curve with the *full* slope to higher  $p_T$  and *not* by producing a hydro-like quasi-linear rise with a *reduced* slope. In view of this the elliptic flow data at large impact parameters (see Fig. 20 below) and at lower collision energies<sup>23,112,122,123</sup>, which show a *linear rise of  $v_2(p_T)$  with a smaller slope* than hydrodynamically predicted, pose an unresolved puzzle which is not simply explained by incomplete local thermalization.

Figure 19 also shows that very high transport opacities are necessary if the parton cascade is required to follow the data to  $p_T \sim 1.5\text{--}2\text{ GeV}/c$ . The necessary values exceed perturbative expectations by at least a factor 30,<sup>78</sup> raising the question which microscopic interaction mechanism is responsible for the large observed elliptic flow.<sup>13,14,126</sup> However, it was recently discovered<sup>127</sup> that the partonic elliptic flow may not necessarily have to follow the hydrodynamic prediction all the way out to  $p_T \simeq 1.5\text{ GeV}/c$ : If the elliptic flow of the partons gets transferred to the hadrons by a momentum-space coalescence mechanism,<sup>128</sup> it is sufficient if it behaves hydrodynamically up to  $p_T \sim 0.7\text{--}0.8\text{ GeV}/c$  for the pion and proton  $v_2$  to “look hydrodynamic” up to  $p_T \simeq 1.5\text{ GeV}/c$  and  $2.2\text{--}2.4\text{ GeV}/c$ , respectively.<sup>127</sup> This takes away some of the pressure for anomalously large partonic transport opacities.<sup>127</sup>

#### *Centrality dependence of elliptic flow:*

Figure 18 showed that in peripheral collisions the  $p_T$ -integrated elliptic flow lags behind the hydrodynamic predictions. This may reflect incomplete thermalization in the smaller fireballs created in these cases. To study this in more detail, Fig. 20 shows the  $p_T$ -differential elliptic flow for pions and protons for three centrality bins.<sup>129</sup> Due to limitations for particle identification, the data cover only the low- $p_T$  region up to about  $800\text{ MeV}/c$ . In this  $p_T$  region, the left panel shows good agreement of  $v_2(p_T)$  for pions with the hydrodynamic predictions<sup>81</sup> for central and midcentral collisions, but smaller elliptic flow than predicted for the most peripheral bin (45–85% centrality, corresponding to an average impact parameter of about  $11\text{ fm}$ <sup>121</sup>). The graph clarifies that for peripheral collisions the smaller-than-predicted  $p_T$ -integrated elliptic flow seen in Fig. 18 arises mostly from a smaller-than-predicted slope of the  $p_T$ -differential elliptic flow for pions. For the most peripheral collisions this slope is about 20% less than expected if also there the reaction zone were able to fully thermalize. In view of the large average impact parameter in this centrality bin, it is rather surprising that the discrepancy to the hydrodynamic predictions is not larger.

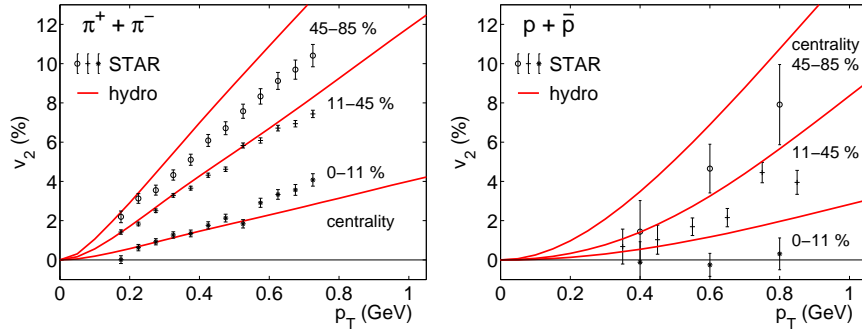


Fig. 20. Elliptic flow of pions (left) and (anti-)protons (right) as measured by the STAR Collaboration<sup>129</sup> in three different centrality bins. Included are results from a hydrodynamic prediction.<sup>81</sup>

The right panel in Fig. 20 shows a similar comparison for protons and antiprotons. Due to the limited statistics of the data, which also were not fully corrected for feeddown from weak  $\Lambda$  decays, no strong conclusions can be drawn from the plot, but the data seem to be generally on the low side compared to the hydrodynamic curves. However, this can have other reasons than a breakdown of hydrodynamics, due to a specific sensitivity of the elliptic flow of heavy hadrons to the nuclear equation of state (see below).

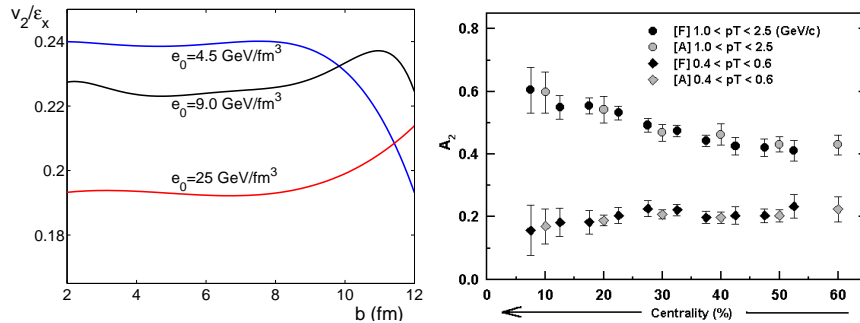


Fig. 21. Left: The  $p_T$ -integrated elliptic flow  $v_2$  scaled by the initial spatial eccentricity  $\epsilon_x$  as a function of impact parameter. Shown are hydrodynamic results with initial conditions corresponding to AGS, SPS and RHIC energies. Quoted are the respective values  $e_0$  for the central energy density in  $b=0$  Pb+Pb collisions:  $e_0 = 4.5$  GeV/fm $^3$  (AGS), 9.0 GeV/fm $^3$  (SPS) and 25 GeV/fm $^3$  (RHIC).<sup>4</sup> Right: PHENIX data<sup>130</sup> for the ratio  $A_2 = v_2/\epsilon_x$  measured in 130 A GeV Au+Au collisions at RHIC in two different  $p_T$  regions. Central collisions are towards the left, peripheral collisions towards the right of the diagram. (Figure taken from<sup>130</sup>).

In hydrodynamic calculations the finally observed elliptic flow is essentially proportional to the initial spatial eccentricity  $\epsilon_x$  of the reaction zone (Section 2.4). This is displayed in the left panel of Fig. 21, where the elliptic flow scaled by the initial eccentricity is plotted as a function of impact parameter<sup>4</sup> (note the suppressed zero on the vertical axis). The slight variation of the ratio  $A_2 = v_2/\epsilon_x$  with impact parameter reflects changes in the stiffness of the equation of state, resulting from the quark-hadron phase transition, which are probed as the impact parameter (and thus the initial energy density in the center of the reaction zone) is varied.<sup>4</sup> This will be discussed in more detail when we describe the beam energy dependence of elliptic flow.

The right panel of Fig. 21 shows RHIC data from the PHENIX Collaboration<sup>130</sup> for the same ratio, at low and high transverse momenta. While the low- $p_T$  data agree with the hydrodynamic prediction of an approximately constant ratio  $v_2/\epsilon_x$ , at high  $p_T$  the scaled elliptic flow is seen to decrease for more peripheral collisions. This is consistent with the earlier discussion of a gradual breakdown of hydrodynamics for increasing  $p_T$  and impact parameter.

#### *Elliptic flow of different hadron species:*

Hydrodynamics predicts a clear mass-ordering of elliptic flow.<sup>81</sup> As the collective radial motion boosts particles to higher average velocities, heavier particles gain more momentum than lighter ones, leading to a flattening of their spectra at low transverse kinetic energies.<sup>83</sup> When plotted against  $p_T$  this effect is further enhanced by a kinematic factor arising from the transformation from  $m_T$  to  $p_T$  (see Fig. 14 and discussion below Fig. 12). This flattening reduces the momentum anisotropy coefficient  $v_2$  at low  $p_T$ ,<sup>81</sup> and the heavier the particle the more the rise of  $v_2(p_T)$  is shifted towards larger  $p_T$  (see top left panel in Fig. 22).

This effect, which is a consequence of both the thermal shape of the single-particle spectra at low  $p_T$  and the superimposed collective radial flow, has been nicely confirmed by the experiments: Figure 22 and the right panel of Fig. 23 show that the data<sup>129,131,132</sup> follow the predicted mass ordering out to transverse momenta of about  $1.5 \text{ GeV}/c$ . For  $K_s^0$  and  $\Lambda + \bar{\Lambda}$  much more accurate data than those shown in Fig. 22 (top right) have recently become available from  $200 \text{ A GeV}$  Au+Au collisions,<sup>133</sup> again in quantitative agreement with hydrodynamic calculations up to  $p_T \simeq 1.5 \text{ GeV}/c$  for kaons and up to  $p_T \simeq 2.5 \text{ GeV}/c$  for  $\Lambda + \bar{\Lambda}$ . The inversion of the mass-ordering in the data at large  $p_T$  is caused by the mesons whose  $v_2(p_T)$  breaks away

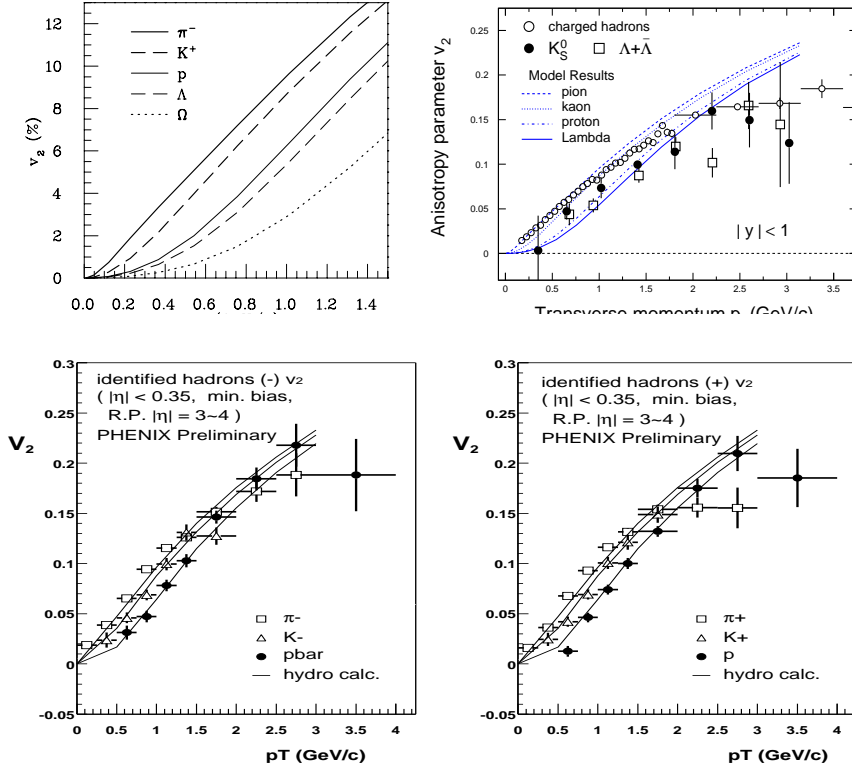


Fig. 22. The  $p_T$ -differential elliptic flow  $v_2(p_T)$  from minimum bias Au+Au collisions at RHIC, for different identified hadron species. Top left: hydrodynamic predictions for  $\sqrt{s} = 130 \text{ A GeV}$ .<sup>81</sup> Top right:  $v_2(p_T)$  for charged hadrons (mostly pions),  $K_s^0$  and  $\Lambda + \bar{\Lambda}$  at  $\sqrt{s} = 130 \text{ A GeV}$  measured by the STAR Collaboration and shown together with hydrodynamic calculations.<sup>131</sup> Bottom row: preliminary results for  $v_2(p_T)$  of identified pions, kaons and protons with negative (left) and positive (right) charge, measured by the PHENIX Collaboration<sup>132</sup> at  $\sqrt{s} = 200 \text{ A GeV}$  and compared with hydrodynamic calculations.<sup>131</sup>

from the hydrodynamic rise and begins to saturate at  $p_T \gtrsim 1.5 \text{ GeV}/c$ . In contrast, baryons appear to behave hydrodynamically to  $p_T \simeq 2.5 \text{ GeV}/c$ , breaking away from the flow prediction and saturating at significantly larger  $p_T$  than the mesons. This is consistent with the idea that the partonic elliptic flow established before hadronization exhibits a hydrodynamic rise at low  $p_T$  followed by saturation above  $p_T \simeq 750 - 800 \text{ MeV}/c$ , and that these features are transferred to the observed hadrons by quark coalescence, manifesting themselves there at twice resp. three times larger  $p_T$ -values.<sup>127</sup>

*Sensitivity to the equation of state:*

The experimental determination of the nuclear equation of state at high densities relies on detailed studies of collective flow patterns generated in relativistic heavy-ion collisions.<sup>11</sup> Since elliptic flow builds up and saturates early in the collision, it is more sensitive to the high density equation of state than the azimuthally averaged radial flow.<sup>75</sup> Hydrodynamic calculations allow to study in the most direct way the influence of the phase transition and its strength (the latent heat  $\Delta e_{\text{lat}}$ ) on the generated flow patterns. This was investigated systematically and in great detail by Teaney et al.,<sup>18,19,20</sup> using hydrodynamics to describe the early quark-gluon plasma expansion stage (including the quark-hadron phase transition), followed by a kinetic afterburner which simulates the subsequent hadronic evolution and freeze-out with the relativistic hadron cascade RQMD.<sup>134</sup> One of their important

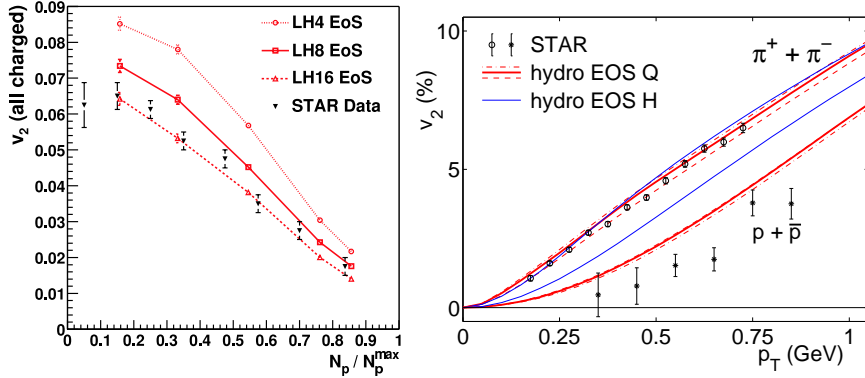


Fig. 23. Left:  $p_T$ -integrated elliptic flow for 130 A GeV Au+Au as a function of collision centrality from a hydrodynamic calculation with a hadron cascade afterburner.<sup>20</sup> LH4, LH8 and LH16 label three different phase transitions with latent heats  $\Delta e_{\text{lat}} = 0.4, 0.8$  and  $1.6 \text{ GeV/fm}^3$ , respectively. Data are from the STAR Collaboration.<sup>124</sup> Right:  $p_T$ -differential elliptic flow of identified pions and (anti)protons from minimum bias 130 A GeV Au+Au collisions,<sup>129</sup> compared with hydrodynamic calculations using Cooper-Frye freeze-out.<sup>14,135</sup> See text for details.

results is shown in the left panel of Fig. 23 which (similar to Fig. 18) gives the  $p_T$ -integrated elliptic flow as a function of the normalized particle yield as a centrality measure. The three curves correspond to equations of state with a first order quark-hadron transition, with latent heat values  $\Delta e_{\text{lat}}$  of 0.4, 0.8 and  $1.6 \text{ GeV/fm}^3$ , respectively.<sup>20</sup> Comparison with the results from the STAR Collaboration shows that a phase transition of significant strength ( $\Delta e_{\text{lat}} \gtrsim 1 \text{ GeV/fm}^3$ ) is necessary to reproduce the data. Without

the softening of the equation of state induced by the phase transition, the single-particle spectra are too flat and the  $p_T$ -integrated elliptic flow comes out too large, even though  $v_2(p_T)$  has roughly the correct slope for pions.

On the other hand, if one eliminates the “QGP push” entirely and replaces the hard quark-gluon plasma equation of state above the phase transition by a softer hadron resonance gas without phase transition (EOS H), one underpredicts the hydrodynamic mass-splitting of the elliptic flow.<sup>14,135</sup> This is seen in the right panel of the figure which shows the  $p_T$ -differential elliptic flow for pions and protons both with a realistic equation of state (EOS Q) and for a pure hadron resonance gas (EOS H). The proton data<sup>129</sup> shown in this plot obviously favor EOS Q, irrespective of moderate variations of the freeze-out temperature, indicated by the three lines labelled by EOS Q.<sup>14,135</sup> Teaney et al.<sup>19</sup> came to similar conclusions; this implies that the details of how the hadronic rescattering stage is described (hydrodynamically with Cooper-Frye freeze-out<sup>14,135</sup> or kinetically via a hadron cascade<sup>18,19,20</sup>) do not matter.

#### *Rapid thermalization:*

We can summarize the comparison between RHIC data and the hydrodynamic model up to this point by stating that hydrodynamics provides a good description of all aspects of the single particle momentum spectra, from central and semicentral Au+Au collisions up to impact parameters  $b \simeq 10$  fm, and for transverse momenta up to  $1.5 \text{ GeV}/c$  for mesons and up to  $2.5 \text{ GeV}/c$  for baryons. Since this  $p_T$ -range covers well over 95% of the emitted particles, it is fair to say that the bulk of the fireball matter created at RHIC behaves hydrodynamically, with little indication for non-ideal (viscous) effects. As explained, the successful description of the data by the hydrodynamic model requires starting the hydrodynamic evolution no later than about  $1 \text{ fm}/c$  after nuclear impact. This estimate is even conservative since it does not take into account any transverse motion of the created fireball matter between the time when the nuclei first collide and when the fireball has thermalized and the hydrodynamic expansion begins. We will now give an independent argument<sup>4,111</sup> why thermalization must happen very rapidly in order for the elliptic flow signal to be as strong as observed in the experiments.

As shown earlier in this Section, the hydrodynamically predicted elliptic flow is proportional to the initial spatial eccentricity  $\epsilon_x(\tau_{\text{equ}})$  at the beginning of the hydrodynamic evolution. If thermalization is slow, the matter will start to evolve in the transverse directions even before  $\tau_{\text{equ}}$ , following its

initial locally isotropic transverse momentum distribution. Even if no reinteractions among the produced particles occur, this radial free-streaming motion dilutes the spatial deformation, although not quite as quickly as in the opposite limit of complete thermalization where it decreases faster due to anisotropic hydrodynamic flow (see Fig. 9). Thus, if thermalization and hydrodynamic behavior set in later, they will be able to build only on a significantly reduced spatial eccentricity  $\epsilon_x$ , and the resulting elliptic flow response will be correspondingly smaller. To reach a certain measured value of  $v_2$  at a given impact parameter thus requires thermalization to set in before free radial motion has reduced the spatial deformation so much that even perfect hydrodynamic motion can no longer produce the measured momentum anisotropy. This consideration yields a *rigorous upper limit for the thermalization time*  $\tau_{\text{equ}}$ .

The dilution of the spatial eccentricity by collisionless radial free-streaming is easily estimated,<sup>4,72</sup> using the analytic solution of the collisionless Boltzmann equation for the distribution function  $f(\mathbf{r}, \mathbf{p}_T, \tau)$  of initially produced approximately massless partons (we only consider their transverse motion):

$$f(\mathbf{r}, \mathbf{p}_T, \tau + \Delta\tau) = f(\mathbf{r} - c\Delta\tau \mathbf{e}_p, \mathbf{p}_T, \tau). \quad (24)$$

Here  $\mathbf{e}_p$  is a unit vector in direction of  $\mathbf{p}_T$ . With Eq. (24) it is straightforward to compute the time-dependence of the spatial eccentricity:

$$\begin{aligned} \epsilon_x(\tau_0 + \Delta\tau) &= \frac{\int dx dy (y^2 - x^2) \int d^2 p_T f(\mathbf{r} - c\Delta\tau \mathbf{e}_p, \mathbf{p}_T, \tau_0)}{\int dx dy (y^2 + x^2) \int d^2 p_T f(\mathbf{r} - c\Delta\tau \mathbf{e}_p, \mathbf{p}_T, \tau_0)} \quad (25) \\ &= \frac{\int dx dy p_T dp_T d\varphi_p [(y + c\Delta\tau \sin \varphi_p)^2 - (x + c\Delta\tau \cos \varphi_p)^2] f(\mathbf{r}, \mathbf{p}_T, \tau_0)}{\int dx dy p_T dp_T d\varphi_p [(y + c\Delta\tau \sin \varphi_p)^2 + (x + c\Delta\tau \cos \varphi_p)^2] f(\mathbf{r}, \mathbf{p}_T, \tau_0)}. \end{aligned}$$

The initial distribution at  $\tau_0$  is even in  $x$  and  $y$ , and the initial transverse momentum distribution can be assumed to be locally isotropic. From this it follows directly that

$$\frac{\epsilon_x(\tau_0 + \Delta\tau)}{\epsilon_x(\tau_0)} = \left[ 1 + \frac{(c\Delta\tau)^2}{\langle \mathbf{r}^2 \rangle_{\tau_0}} \right]^{-1}, \quad (26)$$

where  $\langle \mathbf{r}^2 \rangle_{\tau_0}$  is the azimuthally averaged initial transverse radius squared of the reaction zone. Inserting typical values for, say, Au+Au collisions at  $b = 7$  fm one finds that a delay of thermalization by  $\Delta t = 2.5 \text{ fm}/c$  ( $3.5 \text{ fm}/c$ ) leads to a decrease of the spatial eccentricity by 30% (50%), without generating any momentum anisotropy. The elliptic flow signal resulting from subsequent hydrodynamic expansion would then be degraded by a similar

percentage. Since at  $b = 7$  fm the RHIC data exhaust the hydrodynamic limit calculated with the *full initial eccentricity*  $\epsilon_x(\tau_0)$  at least at the 80% level, the thermalization time  $\tau_{\text{equ}}$  cannot be larger than about 1.75 fm/ $c$ .

*Excitation function of elliptic flow:*

At RHIC energies, the spectator nucleons (i.e. those nucleons in the two colliding nuclei which do not participate in the reaction) leave the reaction zone at midrapidity before the transverse dynamics begins to develop. This is why the spectator matter could be completely ignored in the initialization of the thermodynamic fields (see Sec. 2.4). At lower energies, the spectator matter plays an active role in the dynamics as it blocks the transverse flow of matter into the reaction plane. Instead, its pressure squeezes the matter out<sup>11</sup> perpendicular to the reaction plane (i.e. in  $y$ -direction), resulting in a negative elliptic flow signal. A transition from negative to positive elliptic flow has been observed at the AGS in Au+Au collisions at beam energies of 4–6 GeV per nucleon.<sup>114,136</sup> Relativistic hadron transport model calculations<sup>136,137</sup> indicate a need for a softening of the equation of state in order to quantitatively reproduce the data.

Here we focus on the excitation function of the in-plane elliptic flow from the high end of the AGS energy range to RHIC and beyond. The left panel of Fig. 24 shows the  $p_T$ -integrated elliptic flow for Pb+Pb or Au+Au collisions at fixed impact parameter  $b = 7$  fm from a purely hydrodynamic calculation.<sup>4</sup> The excitation function is plotted versus the final particle multiplicity since hydrodynamics provides a unique relation between  $v_2$  and  $dN/dy$  at fixed impact parameter but cannot predict the dependence of the latter on the collision energy. The horizontal arrows indicate expected multiplicity ranges for RHIC and LHC before the first measurements were performed. We now know that Au+Au collisions at  $\sqrt{s} = 200$  A GeV and  $b = 0$  yield charged particle multiplicity densities  $dN^{\text{ch}}/dy \approx 650$  at midrapidity,<sup>138</sup> somewhat lower than most people originally expected.<sup>139</sup> It is an easy exercise to translate this into total hadron multiplicity density at  $b = 7$  fm as used in the Figure (roughly you have to multiply the above number by 3/4).<sup>4</sup>

A characteristic feature of the hydrodynamic excitation function of  $v_2$  (solid line in Fig. 24) is a pronounced maximum around multiplicities corresponding to SPS energies,<sup>140</sup> followed by a minimum in the RHIC energy domain (the 200 A GeV data<sup>138</sup> correspond almost exactly to this minimum). The origin of this structure is the quark-hadron phase transition in the equation of state.<sup>4</sup> It softens the matter in the phase transition re-

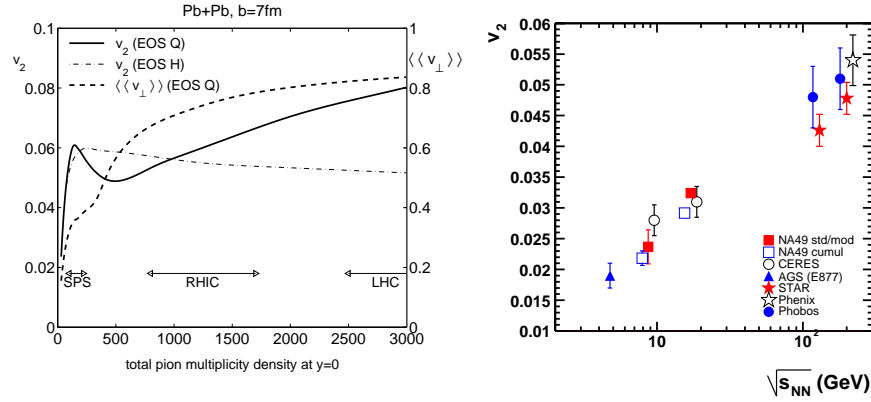


Fig. 24. Left: Excitation function of the elliptic (solid) and radial (dashed) flow for Pb+Pb or Au+Au collisions at  $b = 7$  fm from a hydrodynamic calculation.<sup>4</sup> The collision energy is parametrized on the horizontal axis in terms of total particle multiplicity density  $dN/dy$  at this impact parameter. Right: A compilation of  $v_2$  data vs. collision energy from midcentral (12–34% of the total cross section) Pb+Pb and Au+Au collisions.<sup>122</sup>

gion (small speed of sound  $c_s$ ) which inhibits the buildup of transverse flow (both radial and elliptic). This effect is strongest for RHIC energies where a crucial part of the expansion when the source is still spatially deformed is spent in or close to the phase transition. At SPS energies most of the elliptic flow is generated in the hadronic phase (where  $c_s^2 \approx \frac{1}{6}$ ), whereas at LHC energies essentially all elliptic flow is generated in the QGP phase ( $c_s^2 \approx \frac{1}{3}$ ).<sup>4</sup>

Unfortunately, the available data,<sup>122</sup> shown in the right panel of Fig. 24, do not support this hydrodynamic prediction. Given the success of the hydrodynamic approach at RHIC energies, as pointed out in the earlier parts of this Section, this suggests a breakdown of hydrodynamics at lower collision energies. One can think of at least two reasons for such a breakdown: (i) Lack of early thermalization: The equilibration times at SPS energies might be larger than assumed in the calculation ( $\tau_{\text{equ}} = 0.8$  fm/c), so the hydrodynamic evolution starts later and builds on an already degraded spatial eccentricity. Given the smaller particle densities and collision rates at lower collision energies this possibility requires serious consideration. (ii) Lack of late thermalization: In the hydrodynamic calculations for the SPS, the spatial eccentricity does not disappear until significantly after the fireball matter has been fully converted to hadrons. More than half of the finally observed elliptic flow is thus generated during the hadronic stage.<sup>4</sup> If during this stage the hydrodynamic evolution is replaced by a microscopic kinetic description, the hadronic growth of the momentum anisotropy is sig-

nificantly reduced,<sup>19,20</sup> due to viscous effects in the hadronic cascade. In fact, such a combination of a hydrodynamic description until hadronization followed by a hadronic cascade afterwards leads to a monotonously increasing excitation function, in qualitative agreement with experiment.<sup>19</sup> However, even in this hybrid approach the successful description of the SPS data still requires rapid thermalization to produce sufficient anisotropies already in the early collision stages;<sup>19,20</sup> this argues against possibility (i) above. The hybrid approach also does a better job than pure hydrodynamics in very peripheral collisions at RHIC energies where it produces a weaker response to the remaining spatial deformation during the hadronic stage than the pure hydrodynamic approach which overestimates  $v_2$  at large impact parameters.

If incomplete thermalization, especially somewhat later in the collision, is the reason for the failure of hydrodynamics at SPS energies, it would be of enormous help if we could perform elliptic flow studies with larger deformed systems than those created in peripheral Pb+Pb collisions. Fully central collisions between uranium nuclei offer such a possibility:<sup>4,22</sup> At similar spatial deformation as  $b = 7$  fm Pb+Pb collisions, the fireball formed in a side-on-side U+U collision is about twice as big in the transverse direction, a larger fraction of the elliptic flow is created before hadronization, and the fireball decouples several fm/ $c$  later and with smaller transverse velocity gradients.<sup>4</sup> All of these aspects should significantly improve the chances for a successful hydrodynamic description of elliptic flow in central U+U collisions down to SPS energies. This might open the door for confirming the hydrodynamic prediction of a non-monotonic behavior of  $v_2$  as a function of collision energy which would unambiguously signal the softening of the equation of state near the hadronization phase transition.<sup>4</sup>

#### *Elliptic flow at non-zero rapidity:*

The hydrodynamic results presented so far were obtained with a code which explicitly implements longitudinal boost invariance<sup>62,63,70</sup> (see Sec. 2.6). By doing so one gives up all predictive power for the rapidity dependence of physical observables. Even if longitudinal boost invariance may be a reasonable approximation around midrapidity, it surely breaks down close to the longitudinal kinematic limit, i.e. near the projectile and target rapidities.

In order to overcome these limitations, more elaborate 3+1 dimensional hydrodynamic calculations have recently been done, mostly by two Japanese groups.<sup>44,141,142,143,144</sup> These require, of course, initial condi-

tions along the entire longitudinal axis. Since there is relatively little hydrodynamic evolution in the rapidity direction<sup>64</sup> (due to the logarithmic nature of this variable), the initial longitudinal distribution is rather tightly constrained by the measured final rapidity distributions.<sup>144</sup> The underlying assumption is, of course, local thermalization at all rapidities, which needs to be tested.

Such a model can then predict the dependence of elliptic flow on rapidity. The PHOBOS collaboration has measured the elliptic flow of unidentified charged particles over a wide range of pseudorapidity.<sup>145</sup> In Figure 25 these data are compared to a fully three-dimensional hydrodynamic calculation.<sup>89</sup> The two different curves use different equations of state in

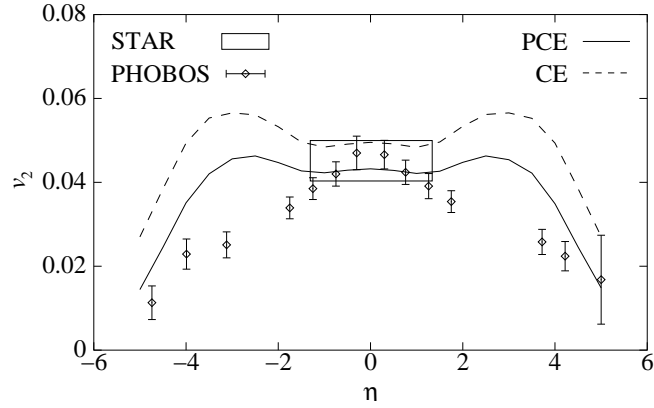


Fig. 25.  $p_T$ -integrated elliptic flow for minimum bias Au+Au collisions at  $\sqrt{s} = 130$  A GeV as a function of pseudorapidity,<sup>89</sup> compared with data from PHOBOS and STAR.<sup>145,124</sup>

the hadronic phase, either assuming chemical equilibrium (CE) until kinetic freeze-out or assuming decoupling of the abundances of stable hadrons already at hadronization (PCE). One sees that as soon as one moves away from midrapidity the nice agreement of the data with the hydrodynamic predictions is lost. The origin of this is not yet fully clarified but is presumably a combination of both longitudinal boost invariance and local thermal equilibrium breaking down away from midrapidity.

It may be worth commenting on some of the features of the data and the calculations: The slight peak at  $\eta = 0$  (which is more strongly expressed in the data than in the calculation) is largely a kinematic effect which arises when one plots a flat rapidity distribution as a function of pseudorapidity.<sup>146</sup> Preliminary  $v_2(\eta)$  data from the 200 GeV run at

RHIC<sup>147</sup> appear to be less peaked in the region  $|\eta| \lesssim 1$  and more consistent with the hydrodynamic calculations in this  $\eta$ -domain. The hydrodynamic peaks at  $\eta \sim \pm 3$  reflect mostly the initial conditions of the calculation, in particular the decreasing initial entropy density at forward and backward rapidities which, according to the discussion of the left panel of Fig. 24, should lessen the softening effects of the quark-hadron transition and *increase* the elliptic flow before dropping to zero at even larger rapidities. That this hydrodynamic feature is again not seen in the data may have similar reasons as the observation of a smaller than predicted elliptic flow at SPS energies (see previous subsection).

The rapidity-dependent baryon and antibaryon spectra<sup>102</sup> show that the net baryon number and thus the baryon chemical potential  $\mu_b$  increases with rapidity  $|y|$ . With observables at finite rapidity one might therefore be able to explore the equation of state over a larger parameter space. This is of particular interest since recent lattice calculations<sup>148</sup> provide evidence for a tricritical point somewhere at  $\mu_b > 0$  where the quark-hadron transition changes from a rapid crossover into a first-order phase transition. The effects of such a tricritical point in a hydrodynamically evolving system could lead to interesting signals and phenomena, such as bubble formation accompanied by large fluctuations.<sup>149</sup>

#### *Beyond hydrodynamics – elliptic flow at high $p_T$ :*

Hydrodynamic flow flattens the transverse momentum spectra, and elliptic flow flattens them more strongly in  $p_x$  than in  $p_y$  direction. As a result, hydrodynamics predicts  $v_2 = \langle \cos 2\varphi_p \rangle$  to grow monotonously with  $p_T$ , approaching  $v_2 = 1$  at  $p_T = \infty$ .<sup>81</sup>

In reality, high- $p_T$  particles do not behave hydrodynamically since they escape from the fireball before having suffered a sufficient number of rescatterings to thermalize their momenta. Whereas the hydrodynamic spectra drop exponentially at large  $p_T$ , with an asymptotic slope reflecting a blueshifted freeze-out temperature<sup>67,83</sup>  $T_{\text{eff}} = T_{\text{dec}} \sqrt{\frac{1+v_r}{1-v_r}}$  (where  $v_r$  here is the largest radial flow velocity at any point inside the fireball), the measured spectra<sup>150,151,152,153</sup> exhibit a power law tail at high  $p_T$  which increases the yield of high- $p_T$  hadrons much above the hydrodynamic expectation.

As reviewed elsewhere in this volume,<sup>154</sup> these “hard” hadrons reflect production and medium modification mechanisms which, at sufficiently high  $p_T$ , can be computed directly from QCD. Above  $p_T \gtrsim 4 \text{ GeV}/c$  they dominate hydrodynamic particle emission.<sup>155</sup> In the cross-over region between

the hydrodynamic domain ( $p_T \lesssim 2 \text{ GeV}/c$ ) and the perturbative QCD domain ( $p_T > 5-10 \text{ GeV}/c$ ) quark-coalescence may be the primary production mechanism.<sup>127,128,104,156,157</sup> In this picture, intermediate- $p_T$  hadrons form by recombination of two or three partons with lower  $p_T$  and thus still partially reflect the hydrodynamic behavior which fully controls soft hadron production.

Recent studies<sup>104,156</sup> suggest that at  $p_T > 5 \text{ GeV}/c$  hadron production may start to become dominated by fragmentation of hard partons whose production can be calculated perturbatively. In this domain one again expects momentum anisotropies which are correlated with the reaction plane, but from an entirely different effect which has nothing to do with collective hydrodynamic flow.<sup>158</sup> High energy partons traveling through a medium with deconfined color charges are expected to lose energy via induced gluon radiation (see the accompanying article by Gyulassy et al.<sup>154</sup> for details and references). In noncentral collisions, high momentum particles traveling along the short direction of the overlap zone (i.e. into the reaction plane) will lose less momentum and thus escape with higher  $p_T$  than partons emitted perpendicular to the reaction plane which have to cross a longer stretch of hot and dense matter. This leads to a positive value of  $v_2$  even at high  $p_T$  which drops to zero logarithmically as  $p_T \rightarrow \infty$ .<sup>158</sup> A qualitatively similar behavior at high  $p_T$  is expected in the ‘‘Color Glass Condensate’’ picture.<sup>159</sup>

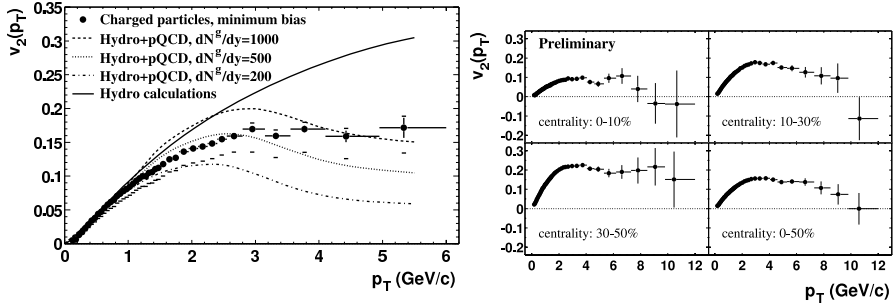


Fig. 26. Elliptic flow of charged particles out to large transverse momenta. The left panel shows results from STAR<sup>125</sup> from Au+Au collisions at 130 GeV, together with hydrodynamic<sup>23</sup> and perturbative jet quenching calculations,<sup>161</sup> assuming various initial gluon densities. The right panel shows preliminary results of the elliptic flow of all charged hadrons from 200 A GeV Au+Au collisions for four centrality classes, as measured by the STAR collaboration.<sup>160</sup>

Quantitative calculations of this effect, including the interplay<sup>161</sup> with hydrodynamic elliptic flow at low  $p_T$  and the diluting effects of hydrody-

namic expansion on the matter traversed by the hard parton<sup>162,163</sup> at high  $p_T$ , were recently performed. Generally, the observed signals (shown in Fig. 26) are considerably larger than predicted. Even in the extreme limit of complete jet quenching (zero mean free path for hard partons), where  $v_2$  reduces to an albedo effect which can be calculated geometrically,<sup>135</sup> the predicted signal is still too small.<sup>164</sup> This suggests that in the  $p_T$ -region covered by Fig. 26 additional contributions, other than parton energy loss, still contribute to the data. This may include unwanted two-particle correlations which are not correlated with the reaction plane and which may be removable by a higher-order cumulant analysis<sup>116</sup> once data with better statistics become available.

#### 4.2. Space-time information from momentum correlations

Obviously, the fireballs formed in heavy-ion collisions are too small and shortlived to obtain a picture of their size and shape in coordinate space by usual methods, i.e. by scattering something of them and observing the diffraction pattern. Quantum statistical and final state interaction induced correlations among the momenta of the produced particles offer an alternative approach to extract space-time information about the emitting source. This tool, known as intensity interferometry,<sup>165</sup> uses the fact that the probability of finding two particles with given pair and relative momenta in the same event is not simply the product of the independent probabilities to find each particle with the corresponding momenta, but reflects correlations between these momenta which are sensitive to the distance between the two particles when they were emitted. Although this tool does not allow for a complete model-independent reconstruction of the source,<sup>166,167</sup> it puts tight constraints on its spatial and temporal structure which, when combined with theoretical constraints for a consistent dynamical evolution and with supplementary experimental information from the single-particle spectra on the momentum-space structure of the source, allow to extract very detailed space-time information.<sup>166,167</sup>

An up-to-date review of this tool and a description of the underlying theoretical formalism can be found elsewhere in this volume in the article by Tomášik and Wiedemann.<sup>79</sup> Here we only summarize the most important predictions for two-particle Bose-Einstein correlations among pions from the hydrodynamic model, in particular for non-central collisions where a new type of intensity interferometric analysis can complement the above discussion of momentum anisotropies generated during the *early* collision

stages with information about spatial deformations *at the end of the collision*. Since any dynamical model relates these two aspects in a unique way, emission-angle dependent HBT-interferometry (where the acronym stands for the initials of the originators of this method<sup>165</sup>) has the potential of putting much stronger constraints on these models than a study of the single-particle spectra or of central collisions alone.

#### 4.2.1. The hydrodynamic source function

HBT interferometry is based on a fundamental relation<sup>79,166,168</sup> (see Eq. (33) below) which relates the two-particle correlation function to a Fourier transform of the source function (a.k.a. emission function)  $S_i(x, K)$  for particles of species  $i$ . This emission function is a Wigner density which, in hydrodynamic simulations, is replaced by its classical analogue, the phase-space probability density for finding a hadron  $i$  emitted from space-time point  $x$  with four-momentum  $K$ . If freeze-out is implemented in hydrodynamics by sudden decoupling on a sharp freeze-out hypersurface  $\Sigma$  as described in Sec. 2.5, the emission function takes the form<sup>169,170</sup>

$$S_i(x, K) = \frac{g_i}{(2\pi)^3} \int_{\Sigma} \frac{K \cdot d^3\sigma(x') \delta^4(x - x')}{\exp\{[K \cdot u(x') - \mu_i(x')]/T_{\text{dec}}(x')\} \pm 1}. \quad (27)$$

Phenomenological fits to spectra and HBT data often use a generalization of this form which replaces the  $\delta$ -function by allowing for a spread of emission times (“fuzzy freeze-out”).<sup>171,172,173</sup>

For a longitudinally boost invariant source (see Sec. 2.6) the freeze-out hypersurface can be parametrized in terms of the freeze-out eigentime as a function of the transverse coordinates,  $\tau_f(x, y)$ . The normal vector  $d^3\sigma_{\mu}$  on such a surface is given by

$$d^3\sigma = \left( \cosh \eta, \nabla_{\perp} \tau_f(x, y), \sinh \eta \right) \tau_f(x, y) dx dy d\eta. \quad (28)$$

With the four momentum  $K^{\mu} = (M_T \cosh Y, \mathbf{K}_T, M_T \sinh Y)$ , where  $Y$  and  $M_T$  are the rapidity and transverse mass associated with  $K$ , Eq. (27) becomes

$$\begin{aligned} S_i(x, K) = \frac{g_i}{(2\pi)^3} \int_{-\infty}^{\infty} d\eta dx dy & [M_T \cosh(Y - \eta) - \mathbf{K}_T \cdot \nabla_{\perp} \tau_f(x, y)] \\ & \times f(K \cdot u(x), x) \delta(\tau - \tau_f(x, y)) \end{aligned} \quad (29)$$

with the flow-boosted local equilibrium distribution  $f(K \cdot u(x), x)$  from (10).

With this expression we can now study the emissivity of the source as a function of mass and momentum of the particles. For the purpose of

presentation we integrate the emission function over two of the four space-time coordinates and discuss the contours of equal emission density in the remaining two coordinates. We begin with calculations describing central Au+Au collisions at  $\sqrt{s_{NN}} = 130$  GeV and focus on directly emitted pions, neglecting pions from unstable resonance decays. Resonance decay pions are known to produce non-Gaussian tails in the spatial emission distribution, increasing its width, but these tails are not efficiently picked up by a Gaussian fit to the width of the measured two-particle momentum correlation function.<sup>174,175</sup> A comparison of the experimental HBT size parameters extracted from such fits with the spatial widths of the emission function is thus best performed by plotting the latter without resonance decay contributions.

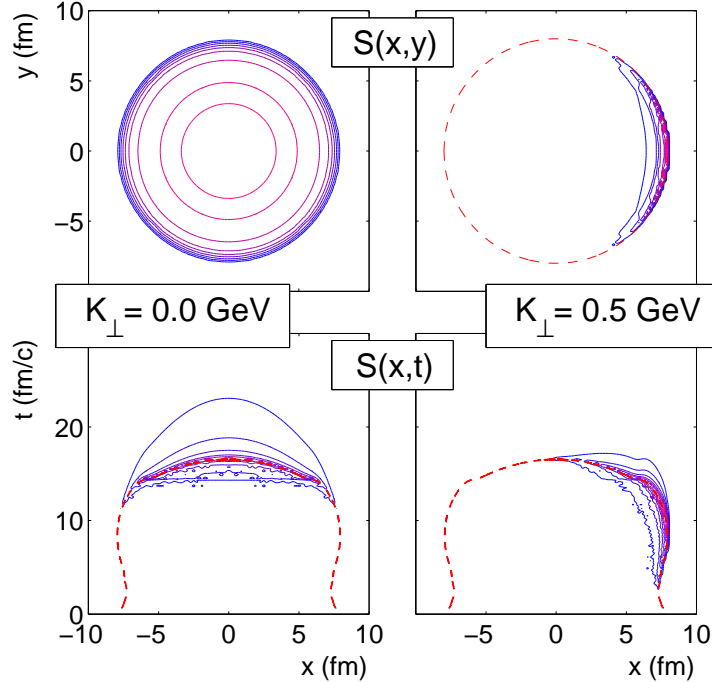


Fig. 27. Pion source function  $S(x, K)$  for central Au+Au collisions at  $\sqrt{s_{NN}} = 130$  GeV. The upper row shows the source after integrating out the longitudinal and temporal coordinate, in the lower row the source is integrated over the longitudinal and one transverse coordinate ( $y$ ). In the left column we investigate the case  $K = 0$ , in the right column the pions have rapidity  $Y = 0$  and transverse momentum  $K_T = 0.5$  GeV in  $x$  direction.<sup>13</sup>

Figure 27 shows equal density contours at 10, 20, ..., 90% of the max-

imum in a transverse cut integrated over time and  $\eta$  (top row) and as a function of radius and time integrated over  $\eta$  and the second transverse coordinate (bottom row). The dashed circle in the top row indicates the largest freeze-out radius reached during the expansion, the dashed line in the bottom row gives the freeze-out surface  $\tau_f(x, y=0) = t_f(x, y=z=0)$ . Pions with vanishing transverse momentum (left column) are seen to come from a broad region symmetric around the center and are emitted rather late. Pions with  $K_T = 0.5$  GeV pointing in  $x$ -direction, on the other hand, are emitted on average somewhat earlier and only from a rather thin, crescent shaped sliver along the surface of the fireball at its point of largest transverse extension. The reason for this apparent ‘‘opacity’’ (surface dominated emission) of high- $p_T$  particles is that they profit most from the radial collective flow which is largest near the fireball surface. Low- $p_T$  pions don’t need the collective flow boost and are preferably emitted from smaller radii (where the flow velocity is smaller) when the freeze-out surface eventually reaches these points during the final stage of the decoupling process.

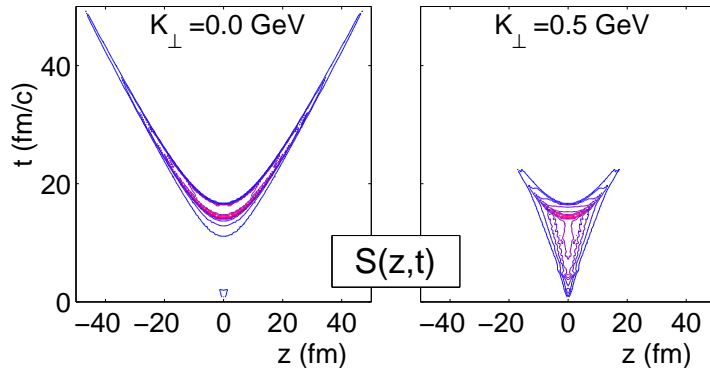


Fig. 28. Longitudinal cuts through the pion emission function  $S(x, K)$ , integrated over transverse coordinates, for  $Y=0$  pions with two different values of  $K_T$  as indicated.<sup>72</sup>

Fig. 28 displays the time structure of the emission process along the beam direction. Especially for low transverse momenta one clearly sees a very long emission duration, as measured in the laboratory (center-of-momentum frame). The reason is that, according to the assumed longitudinal boost invariance, freeze-out happens at constant proper time  $\tau = t^2 - z^2$  and extends over a significant range in longitudinal position  $z$ . This range is controlled by the competition between the longitudinal expansion velocity gradient (which makes emission of  $Y=0$  pions from points at large  $z$  values un-

likely) and the thermal velocity smearing. If freeze-out happens late (large  $\tau$ ), the longitudinal velocity gradient  $\sim 1/\tau$  is small and pions with zero longitudinal momentum are emitted with significant probability even from large values of  $|z|$ , i.e. very late in coordinate time  $t$ . Note that this is also visible in the lower left panel of Fig. 27 where significant particle emission still happens at times where the matter at  $z=0$  has already fully decoupled. We will see shortly that this poses a problem when compared with the data. The long tails at large values of  $|z|$  and  $t$  can only be avoided by reducing  $\tau_f$  (thereby increasing the longitudinal velocity gradient and reducing the  $z$ -range which contributes  $Y=0$  pions) and/or by additionally breaking longitudinal boost-invariance by reducing the particle density or postulating earlier freeze-out at larger space-time rapidities  $|\eta|$ .<sup>89</sup>

The spatial and temporal extensions of the emission process are characterized by the “spatial correlation tensor”

$$S_{\mu\nu}(Y, K_T, \Phi; b) = \langle \tilde{x}_\mu \tilde{x}_\nu \rangle \quad (30)$$

where  $\tilde{x}_\mu = x_\mu - \langle x_\mu \rangle$  is the distance to the center  $\langle x \rangle$  of the emission region for momentum  $K$  and  $\Phi = \angle(\mathbf{K}_T, \mathbf{b})$  is the azimuthal emission angle relative to the reaction plane. The averages are taken with the source function,

$$\langle g(x, y, z, t) \rangle(K) = \frac{\int d^4x g(x, y, z, t) S(x, K)}{\int d^4x S(x, K)}. \quad (31)$$

The components of the spatial correlation tensor quantify the emission regions in terms of their spatial and temporal widths. These are directly related to the HBT size parameters extracted from the width of the two-particle correlation function in momentum space.<sup>166</sup>

#### 4.2.2. HBT-radii – central collisions

Intensity interferometry is based on the analysis of the two-particle momentum correlation function

$$C(\mathbf{p}_1, \mathbf{p}_2) = \frac{E_1 E_2 \frac{dN}{d^3p_1 d^3p_2}}{E_1 \frac{dN}{d^3p_1} \cdot E_2 \frac{dN}{d^3p_2}}. \quad (32)$$

Quantum statistical effects (wave function (anti)symmetrization) between identical particles and final state interaction corrections between identical or non-identical particles cause this correlation function to deviate from unity for small momentum differences  $\mathbf{p}_1 \approx \mathbf{p}_2$ . One therefore conveniently expresses it in terms of the momentum difference  $\mathbf{q} = \mathbf{p}_1 - \mathbf{p}_2$  and the average momentum  $\mathbf{K} = (\mathbf{p}_1 + \mathbf{p}_2)/2$ . When these are supplemented by

the energy difference  $q^0 = E_1 - E_2$  and average energy  $K^0 = (E_1 + E_2)/2$  of the two particles, the resulting four-vectors satisfy the orthogonality relation  $K_\mu q^\mu = (m_1^2 - m_2^2)/2$  ( $= 0$  for identical particles). Under standard assumptions<sup>79,166</sup> (such as the absence of final state interactions) the 2-pion correlation function can be related to the pion emission function  $S(x, K)$ :

$$C(\mathbf{q}, \mathbf{K}) \approx 1 + \left| \frac{\int d^4x S(x, K) e^{i \mathbf{q} \cdot \mathbf{x}}}{\int d^4x S(x, K)} \right|^2. \quad (33)$$

For central collisions this does not depend on the azimuthal emission angle  $\Phi$ . In a Cartesian coordinate system where the *out*-, *side*- and *long*-directions are defined parallel to  $\mathbf{K}_T$ , perpendicular to  $\mathbf{K}_T$ , and in beam direction, respectively, the source formed in a central collision is reflection symmetric under  $x_s \rightarrow -x_s$ . Exploiting longitudinal boost invariance of the source by selecting a frame for the analysis which moves with the longitudinal pair velocity  $\beta_L = K_L/K^0$  (Longitudinal Co-Moving System, LCMS), one finds that in Gaussian approximation<sup>166</sup> the correlation function can be completely characterized in terms of three *HBT-radii* which depend only on the magnitude of  $K_T$ :

$$C(\mathbf{q}, \mathbf{K}) \approx 1 + \exp \left[ -R_o^2(K_T) q_o^2 - R_s^2(K_T) q_s^2 - R_l^2(K_T) q_l^2 \right]. \quad (34)$$

(Without boost invariance the exponent contains in general a fourth term<sup>176</sup> and all HBT radii depend additionally on the pair rapidity  $Y$ .) These HBT-radii are directly related to the following combination of components of the spatial correlation tensor  $S_{\mu\nu}$ :

$$R_s^2(K) = \langle \tilde{x}_s^2 \rangle, \quad (35)$$

$$R_o^2(K) = \langle \tilde{x}_o^2 \rangle - 2\beta_T \langle \tilde{x}_o \tilde{t} \rangle + \beta_T^2 \langle \tilde{t}^2 \rangle, \quad (36)$$

$$R_l^2(K) = \langle \tilde{z}^2 \rangle, \quad (37)$$

where  $\beta_T = K_T/K^0$  is the transverse pair velocity.

From earlier hydrodynamic calculations<sup>177</sup> it was expected that a fireball evolving through the quark-hadron phase transition would emit pions over a long time period, resulting in a large contribution  $\beta_T^2 \langle \tilde{t}^2 \rangle$  to the outward HBT radius and a large ratio  $R_o/R_s$ . This should be a clear signal of the time-delay induced by the phase transition. It was therefore a big surprise when the first RHIC HBT data<sup>178,179</sup> yielded  $R_o/R_s \approx 1$  in the entire accessible  $K_T$  region (up to  $0.7 \text{ GeV}/c$ ). In the meantime this finding has been shown to hold true out to  $K_T \gtrsim 1.2 \text{ GeV}/c$ .<sup>180</sup>

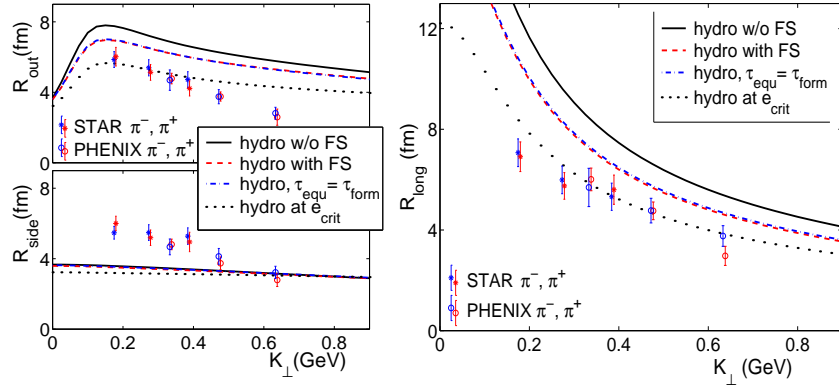


Fig. 29. HBT radii from hydrodynamic calculations<sup>14</sup> (solid lines) together with data from STAR<sup>178</sup> and PHENIX.<sup>179</sup> The dotted lines give hydrodynamic radii calculated directly after hadronization whereas the other two lines refer to different assumptions about the initial conditions (see text).

Figure 29 shows a comparison of the experimental data with results from hydrodynamic calculations.<sup>14</sup> Clearly, a purely hydrodynamic description with default initial conditions (solid lines in Fig. 29) fails to describe the measured HBT radii. The longitudinal and outward radii  $R_l$  and  $R_o$  are too large,  $R_s$  is too small, and the  $K_T$ -dependence of both  $R_o$  and  $R_s$  are too weak in the model. Since for longitudinally boost-invariant sources  $R_l$  is entirely controlled by the longitudinal velocity gradient at freeze-out which decreases as  $1/\tau_f$ , making  $R_l$  smaller within the hydrodynamic approach requires letting the fireball decouple earlier<sup>14</sup> or breaking the boost invariance.<sup>89</sup> As noted above, a smaller  $R_l$  would also reduce the emission duration, i.e.  $\langle \tilde{t}^2 \rangle$ , and thus help to bring down  $R_o$ , especially if freeze-out at nonzero rapidities  $|\eta| > 0$  happens earlier than at midrapidity.

The fireball can be forced to freeze out earlier by changing the freeze-out condition (e.g. by imposing freeze-out directly at hadronization, see dotted line in Fig. 29). This generates, however, serious conflicts with the single-particle spectra (see Sec. 4.1.1). Alternatively, one can allow transverse flow to build up sooner, either by seeding it with a non-zero value already at  $\tau_{\text{equ}}$  (short dashed line labelled “hydro with FS”<sup>14,65</sup>) or by letting the hydrodynamic stage begin even earlier (e.g. at  $\tau_{\text{form}} = 0.2 \text{ fm}/c$ , long-dashed line). The last two options produce similar results, but do not fully resolve the problems with the magnitudes of  $R_l$  and  $R_o$ .

The situation may improve by taking also the breaking of longitudinal boost-invariance into account,<sup>89</sup> but a fully consistent hydrodynamic

description has not yet been found. In particular, the sideward radius  $R_s$  is still too small and the  $K_T$ -dependences of both  $R_s$  and  $R_o$  are still to weak.<sup>14,89</sup> It is hard to see how to increase  $R_s$  without also increasing  $R_o$  and  $R_l$  which are already too large. Hybrid calculations<sup>17</sup> in which the hydrodynamic Cooper-Frye freeze-out is replaced by transition to a hadronic cascade at  $T_{\text{crit}}$ , followed by self-consistent kinetic freeze-out, tend to increase  $R_s$  by making freeze-out more “fuzzy”, but at the expense of also increasing  $R_o$  and  $R_l$  in a disproportionate manner, mainly due to an increase in the emission duration. This makes the problems with the  $R_o/R_s$  ratio even worse.

In the past, a strong  $K_T$ -dependence of  $R_s$  has been associated with strong transverse flow.<sup>166,167</sup> It is therefore surprising that even the hydrodynamic model with its strong radial flow cannot reproduce the strong  $K_T$ -dependence of  $R_s$  measured at RHIC. Also, according to Eq. (35) the difference between  $R_o^2$  and  $R_s^2$  can be reduced, especially at large  $K_T$ ,<sup>173</sup> if the positive contribution from the emission duration  $\langle \tilde{t}^2 \rangle$  is compensated by “source opacity”, i.e. by a strongly surface-dominated emission process.<sup>181,182,183</sup> In this case the geometric contribution  $\langle \tilde{x}_o^2 \rangle$  to  $R_o^2$  is much smaller than  $R_s^2 = \langle \tilde{x}_s^2 \rangle$ . Again, the source produced by the hydrodynamic model (see top right panel in Fig. 27) is about as “opaque” as one can imagine,<sup>74</sup> and it will be difficult to further increase the difference  $\langle \tilde{x}_s^2 - x_o^2 \rangle$ .<sup>183</sup>

This leaves almost only one way out of the “HBT puzzle”, namely the space-time correlation term  $-2\beta_T \langle \tilde{x}_o \tilde{t} \rangle$  in expression (35) for  $R_o^2$ . It correlates the freeze-out position along the outward direction with the freeze-out time. The hydrodynamic model has the generic feature that, in the region where most particles are emitted (see Fig. 27), these two quantities are negatively correlated, because the freeze-out surface moves from the outside towards the center rather than the other way around. Hence the term  $-2\beta_T \langle \tilde{x}_o \tilde{t} \rangle$  is positive and tends to make  $R_o^2$  larger than  $R_s^2$ . The small measured ratio  $R_o/R_s \lesssim 1$  may instead call for strong *positive*  $x_o-t$  correlations, implying that particles emitted from *larger*  $x_o$  values decouple *later*. Hydrodynamics can not produce such a positive  $x_o-t$  correlation (at least not at RHIC energies). On the other hand, there are indications that microscopic models, such as the AMPT<sup>175</sup> and MPC<sup>184</sup> models, may produce them, for reasons which are not yet completely understood.

One should also not forget that Fig. 29 really compares two different things: The data are extracted from the width of the 2-particle correlator in momentum space while in theory one calculates the same quantities from

the source width parameters in coordinate space. The two produce identical results only for Gaussian sources. The hydrodynamic source function shown in Figs. 27 and 28 are not very good Gaussians and show a lot of additional structure. We have checked, however, by explicit computation of the momentum-space correlation function using Eq. (33) that the non-Gaussian effects are small.<sup>b</sup> The largest non-Gaussian effects are seen in the longitudinal radius  $R_l$ ,<sup>174</sup> but although the corresponding corrections go in the right direction by making the  $R_l$  extracted from the momentum-space correlator smaller, the effect is only a fraction of 1 fm and not large enough to bridge the discrepancy with the data.

It was recently suggested<sup>72,185,186</sup> that neglecting dissipative effects might be at the origin of the discrepancy between the purely hydrodynamic calculations and the data. A calculation of first-order dissipative corrections to the spectra and HBT radii at freeze-out,<sup>186</sup> with a “reasonable” value for the viscosity, yielded a significant decrease of  $R_l$  along with a corresponding strong reduction of the emission duration contribution to  $R_o$ , both as desired by the data. There was no effect on the  $x_o - t$  correlations, however, and only a weak effect on  $R_s$  which went in the wrong direction, making it even flatter as a function of  $K_T$ . The rather steep  $K_T$ -dependence of the data for both  $R_s$  and  $R_o$  and the larger than predicted size of  $R_s$  at low  $K_T$  are therefore not explained by this mechanism.<sup>184,186</sup> Furthermore, the elliptic flow  $v_2$  has been shown to be very sensitive to viscosity,<sup>186,187</sup> and the viscosity values needed to produce the desired reduction in  $R_l$  turned out<sup>186</sup> to reduce  $v_2$  almost by a factor 2, incompatible with the data. The “RHIC HBT puzzle” thus still awaits its resolution.

#### 4.2.3. HBT with respect to the reaction plane

The discussion in Sec. 4.1 showed that azimuthal asymmetries in the momentum-space structure helped significantly in eliminating ambiguities of the global dynamical picture extracted from central collisions alone. Similarly, we can expect tight additional constraints from an analysis of spatial anisotropies, using HBT interferometry as a function of the azimuthal emission angle relative to the reaction plane in non-central collisions. In particular, dynamical models provide a characteristic relation between the momentum anisotropies generated early in the collision and the left-over

---

<sup>b</sup>They would have been larger if we had included resonance decay pions in the emission function, as found by Lin et al.,<sup>175</sup> which was our main reason for not doing so.

spatial deformation of the source at the end of the collision. This relation can be tested experimentally by combining elliptic flow measurements with the azimuthal dependence of the two-particle correlator and the extracted HBT radii, and this test can be used to ascertain the validity of the assumptions underlying the specific dynamical model. As an example, hydrodynamics makes clear predictions for the time-dependence of the transverse spatial and momentum anisotropies, and, if valid, it should give the correct sign and magnitude of the spatial deformation at freeze-out for the same set of model parameters which successfully reproduces the radial and elliptic flow in momentum space. Specifically, comparing the final spatial deformation to the initial one puts a constraint on the time between the beginning of transverse expansion and freeze-out, and this in turn may shed light on the origin of the discrepancies between the predicted and measured  $R_l$  values in central collisions discussed in the previous subsection.

The formalism for HBT interferometry relative to the reaction plane was developed by Wiedemann et al.<sup>188,189,190</sup> and is reviewed elsewhere in this volume.<sup>79</sup> Due to the lack of azimuthal symmetry in non-central collisions, there is no  $x_s \rightarrow -x_s$  symmetry and the exponent in Eq. (34) contains all six terms,  $\sum_{i,j=o,s,l} R_{ij}^2 q_i q_j$ , where the “HBT size parameters”  $R_{ij}(Y, K_T, \Phi)$  now also depend on the azimuthal emission angle  $\Phi$  between the transverse emission direction  $\mathbf{K}_T$  and the impact parameter  $\mathbf{b}$ . For longitudinally boost-invariant sources the transverse-longitudinal cross terms  $R_{sl}^2$  and  $R_{ol}^2$  still vanish in the LCMS frame, but there is an important outside cross term  $R_{os}^2$  which is related to the spatial deformation of the source in the transverse plane. For  $b \neq 0$  equations (35) generalize to<sup>79,188,189</sup>

$$R_s^2(\Phi) = \frac{1}{2}(S_{xx} + S_{yy}) - \frac{1}{2}(S_{xx} - S_{yy}) \cos 2\Phi - S_{xy} \sin 2\Phi \quad (38)$$

$$R_o^2(\Phi) = \frac{1}{2}(S_{xx} + S_{yy}) + \frac{1}{2}(S_{xx} - S_{yy}) \cos 2\Phi + S_{xy} \sin 2\Phi - 2\beta_T(S_{tx} \cos \Phi + S_{ty} \sin \Phi) + \beta_T^2 S_{tt} \quad (39)$$

$$R_{os}^2(\Phi) = S_{xy} \cos 2\Phi - \frac{1}{2}(S_{xx} - S_{yy}) \sin 2\Phi + \beta_T(S_{tx} \sin \Phi - S_{ty} \cos \Phi) \quad (40)$$

$$R_l^2(\Phi) = S_{zz}. \quad (41)$$

Here the spatial correlation tensor  $S_{\mu\nu} = \langle \tilde{x}_\mu \tilde{x}_\nu \rangle$  is specified in reaction-plane coordinates ( $x$  points along the impact parameter and  $y$  is perpendicular to the reaction plane) where, due the reflection symmetry of the overlap zone with respect to the  $x$  and  $y$  axes, it is most easily evaluated.

The indicated *explicit*  $\Phi$ -dependence arises from the rotation between the outward direction  $x_o \parallel \mathbf{K}_T$  and the  $x$ -axis. In addition, the components  $S_{\mu\nu}$  of the spatial correlation tensor, being defined as expectation values with a  $\Phi$ -dependent emission function  $S(x, K) = S(x, Y, K_T, \Phi)$ , contribute an *implicit*  $\Phi$ -dependence which is not shown here. Both types of  $\Phi$ -dependences can be analyzed together, exploiting the symmetries of the emission function with respect to the reaction plane and to projectile-target interchange. One finds<sup>190</sup> that in general  $R_s^2$ ,  $R_o^2$  and  $R_l^2$  are superpositions of cosines of even multiples of  $\Phi$  while  $R_{os}^2$  is a superposition of sines of even multiples of  $\Phi$ . In lowest order  $R_s^2$ ,  $R_o^2$ , and  $R_l^2$  thus oscillate with  $\cos(2\Phi)$  around some constant average while  $R_{os}^2$  oscillates with  $\sin(2\Phi)$  around zero.

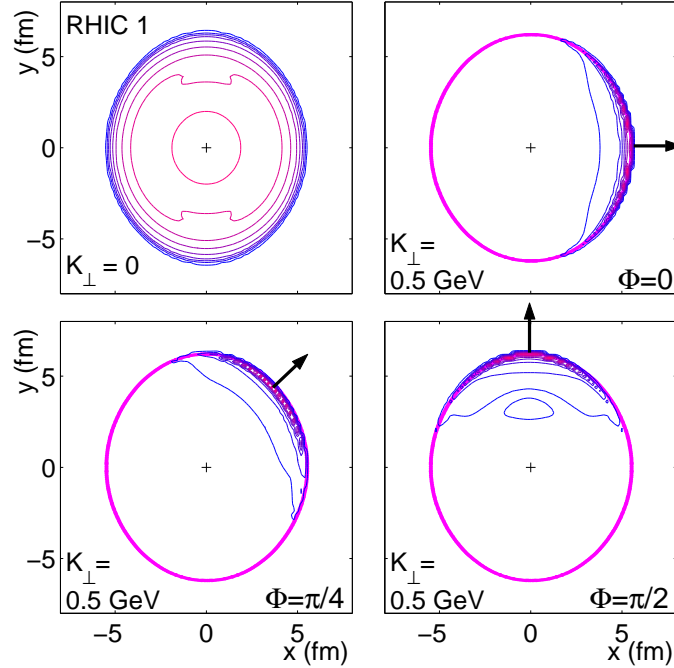


Fig. 30. Contours of constant emission density for the source created in 130 A GeV Au+Au collisions at  $b = 7$  fm as predicted by hydrodynamics.<sup>74</sup> The top left panel shows the contours for  $K_T = 0$ , the three other panels show contours for  $K_T = 0.5$  GeV pointing in 3 different directions. The thick solid oval lines indicate the maximum extension of the source.

In Sec 3.2 we saw for non-central collisions that, as time evolves, the initial out-of-plane deformation of the nuclear reaction zone decreases, crosses

zero and eventually turns into an elongation along the impact parameter direction (see Fig. 9). At different times the freeze-out surface (see Fig. 27) thus reflects different spatial deformations. Hence, the effective deformation probed by the two-particle correlation function is the average of the spatial eccentricity taken over the freeze-out surface. Figure 30 shows contour plots of the emission function from the same hydrodynamic calculations which reproduced the spectra and elliptic flow data from 130  $\text{A}$  GeV Au+Au collisions at RHIC (see Sec. 4.1), for an impact parameter  $b = 7$  fm. The underlaid outer contour shows that, at the time of its largest spatial extension, the hydrodynamic source is still elongated out-of-plane, although much less so than at the beginning. As seen in the upper left panel, this out-of-plane elongation is probed by low- $K_T$  pions which, just as in the central collision case shown in Fig. 27, are emitted from the entire region inside this outer contour. In contrast, pions with non-zero transverse momentum are emitted from relatively thin slivers near the outer edge of the fireball and therefore do not directly probe the overall deformation of the source. The shapes of their emission regions are controlled by an interplay between the curvature of the outer edge of the source and the strength of the anisotropic transverse flow, which both vary with the azimuthal emission angle.<sup>74</sup>

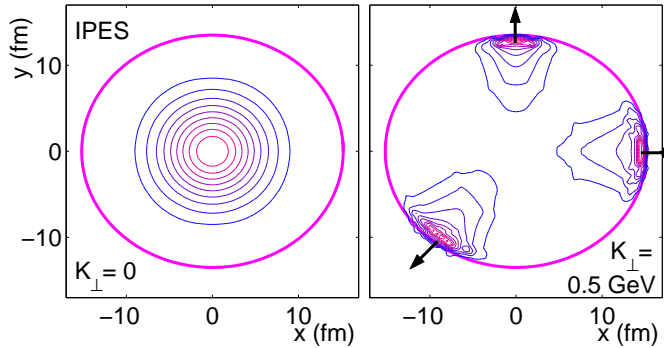


Fig. 31. Contours of constant emission density for a strongly in plane oriented source.<sup>74</sup> The left panel shows the contours for pions with  $K_T = 0$ , the right panel shows contours for pions with  $K_T = 0.5$  GeV emitted in 3 different azimuthal directions. In both panels the thick solid line indicates the maximum extension of the source.

In order to see how these patterns would change if at freeze-out the source were actually elongated *along* the reaction plane, and how the HBT correlation function would reflect this difference, we show in Fig. 31 the emission function for a hydrodynamic source which evolved from a much higher initial energy density. The calculation shown in Fig. 31 is for Au+Au

collisions at  $b = 7$  fm, assuming an initial central temperature of 2 GeV at  $\tau_{\text{equ}} = 0.1$  fm/c and decoupling at  $T_{\text{dec}} = 100$  MeV.<sup>74</sup> With such initial conditions it takes the fireball much longer to reach freeze-out and, as seen in the Figure, it has enough time to develop a strong in-plane elongation before decoupling. (IPES stands for “in-plane elongated source”.) The emission function for low- $K_T$  pions is again seen to reflect the overall in-plane elongation of the source at freeze-out (left panel), whereas the emission functions for pions with transverse momentum  $K_T = 500$  MeV/c (right panel) do not probe the overall source deformation, but rather the curvature of its outer edge as a function of the azimuthal emission direction.

These pictures suggest that, if one wants to measure the overall spatial deformation of the source at freeze-out, one should concentrate on pions with small transverse pair momenta  $K_T$ . This is confirmed by the plots in Fig. 32 which show the azimuthal oscillations of the four non-vanishing HBT radius parameters for several values of  $K_T$ . At  $K_T = 0$  the trans-

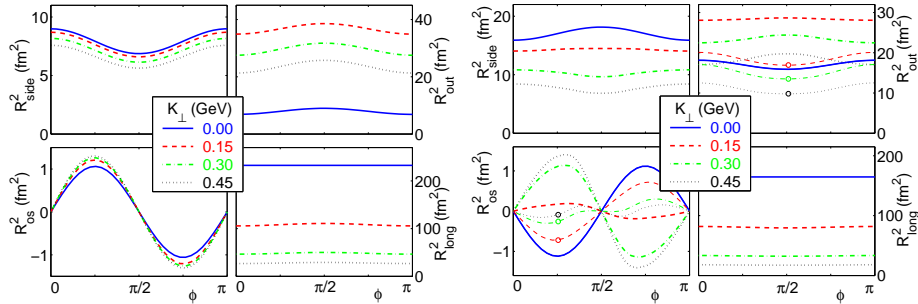


Fig. 32. Oscillations of the HBT radii for different transverse pair-momenta in RHIC collisions (left) and the source elongated into the reaction plane (right).<sup>74</sup> The thin circled lines in the right panel show the geometric contributions to the HBT radius parameters.

verse radius parameters  $R_s^2$ ,  $R_o^2$  and  $R_{os}^2$  show opposite oscillations for the out-of-plane (left) and in-plane (right) elongated sources, and the signs of these oscillations reflect the signs of the geometric source deformation as expected. For example, at RHIC energies  $R_s^2$  oscillates downward, implying a larger sideward radius when viewed from the  $x$  direction (i.e. within the reaction plane) than from the  $y$ -direction (i.e. perpendicular to the reaction plane). For the in-plane elongated source (IPES) some of the oscillation amplitudes change sign at larger transverse momentum. This change of sign originates from an intricate interplay between geometric, dynamical and

temporal aspects of the source at freeze-out.<sup>74</sup>

At this moment the significance of the  $K_T$ -dependence of the oscillation amplitudes for the HBT radius parameters is still largely unexplored. In the hydrodynamic model it is crucially affected by the Cooper-Frye freeze-out criterium which strictly limits the source size and provides a sharp radial cutoff for the distribution of emission points. From the analysis of central collisions<sup>173</sup> it is known that the emission-angle averaged transverse HBT radii (in particular the outward radius  $R_o$ ) exhibit stronger  $K_T$  dependence for sources with a sharp surface (such as a box-like density distribution) than for Gaussian sources. One might expect similarly strong differences for the  $K_T$ -dependence of the oscillation amplitudes in non-central collisions. Model calculations in which the surface diffuseness of the source can be varied confirm this expectation and show a particularly strong effect of this parameter on the oscillations of  $R_o^2$  as a function of  $K_T$ .<sup>191</sup>

The oscillation pattern shown in the left panel of Fig. 32 agrees qualitatively with measurements by the STAR Collaboration at 130 and 200 A GeV.<sup>192,193</sup> Figure 33 shows preliminary data from Au+Au colli-

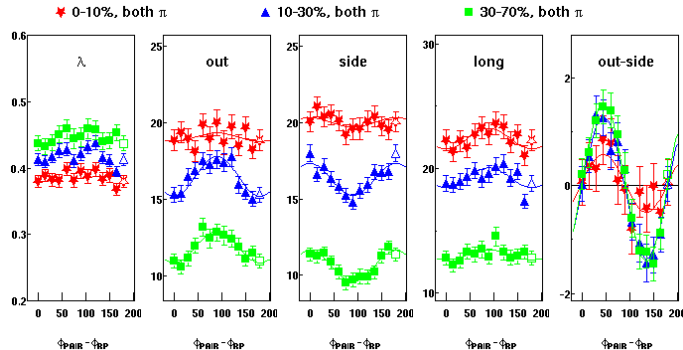


Fig. 33. Preliminary results of the angular dependence of the HBT-radii (squared) for three different centralities at  $\sqrt{s_{NN}} = 200$  GeV.<sup>193</sup>

sions at  $\sqrt{s_{NN}} = 200$  GeV for three different centrality classes.<sup>193</sup> Although these data are integrated over  $K_T$  and not yet final and thus should not be overinterpreted, one observes that the oscillation amplitudes follow the pattern in the left panel of Fig. 32, but not that in the right panel. This implies that the fireball formed in these collisions is still out-of-plane elongated at freeze-out,<sup>192,193</sup> as predicted by hydrodynamics. Whether the

deformation extracted from the data is larger than that in the hydrodynamic model (which, if true, would point to earlier freeze-out as discussed at the end of the previous subsection) is not yet clear. Higher statistics data which are presently being analyzed will soon answer this question.

## 5. Summary and Conclusions

In this review we have summarized some of the most recent theoretical and experimental results indicating that the fireball created in Au+Au collisions at RHIC thermalizes very quickly, evolves through an extended dynamic expansion stage which is governed by intense rescattering, follows the laws of ideal hydrodynamics, and probes the equation of state of nuclear matter at temperatures between 350 MeV and 100 MeV. The data are sensitive to the softening effects of a phase transition on the nuclear equation of state and were shown to be consistent with the existence of a quark-hadron phase transition at energy densities around  $1 \text{ GeV/fm}^3$ . Equations of state without such a phase transition, such as an ideal gas of massless partons or a hadron resonance gas with approximately constant sound velocity  $c_s^2 \approx 1/6$  extending to very high energy densities, are experimentally excluded.

The most important result of the comparison between theory and experiment presented in this review is very strong evidence that hydrodynamics *works* at RHIC, i.e. that it is able to describe the bulk of the data on soft hadron production at  $p_T \lesssim 1.5 - 2 \text{ GeV}/c$ . This includes all hadronic momentum spectra from central ( $b = 0$ ) to semiperipheral ( $b \lesssim 10 \text{ fm}$ ) Au+Au collisions, including their anisotropies. Since the anisotropies are sensitive to the spatial deformation of the reaction zone and thus develop early in the collision, they provide a unique probe for the dense matter formed at the beginning of the collision and its thermalization time scale. The data on elliptic flow can only be understood if thermalization of the early partonic system takes less than about  $1 \text{ fm}/c$ . At this early time, the energy density in the reaction zone is about an order of magnitude larger than the critical value for quark deconfinement, leading to the conclusion that a well-developed, thermalized quark-gluon plasma is created in these collisions which, according to hydrodynamics, lives for about  $5-7 \text{ fm}/c$  before it hadronizes.

The mechanisms responsible for fast thermalization are still not fully understood. Perturbative rescattering of quarks and gluons was shown to be insufficient, leading to thermalization times which are a factor 5–10 too long. The quark-gluon plasma created at RHIC is thus strongly nonperturbative.

As a result of the softening effects of the quark-hadron transition on the nuclear equation of state, hydrodynamics predicts a non-monotonous beam energy dependence of elliptic flow. In particular, the elliptic flow at SPS energies is expected to be larger than at RHIC, inspite of somewhat smaller radial flow. This is not borne out by the existing data from

Pb+Pb collisions at the SPS, due to the unfortunate breakdown of the hydrodynamic model at the lower SPS energy. It is suggested to explore the excitation function of elliptic flow at RHIC by going down as much as possible with the beam energy, using central collisions between deformed uranium nuclei. These would, at similar spatial deformation, provide much larger reaction volumes than peripheral Au+Au collisions, improving the chances for hydrodynamics to work even at lower energies where the fireballs are less dense and thermalization is harder to achieve. A decreasing elliptic flow as a function of increasing collision energy in U+U collisions at RHIC, followed by an increase as one further proceeds to LHC energies, would be an unmistakable signature for the existence of the quark-hadron *phase transition*.

The gradual breakdown of hydrodynamics in peripheral Au+Au collisions between RHIC and SPS energies goes hand-in-hand with a gradual breakdown of hydrodynamics in Au+Au collisions at RHIC as one moves away from midrapidity. The elliptic flow was found to drop dramatically at pseudorapidities  $|\eta| > 1$ , and hydrodynamic calculations are unable to reproduce this feature. It is likely that both observations are related, and again central U+U collisions may clarify this issue.

Whereas the momentum-space structure of the observed hadron spectra is described very well by the hydrodynamic model, at least for  $p_T \lesssim 1.5 - 2 \text{ GeV}/c$ , this is not true for the two-particle momentum correlations which reflect the spatial structure of the fireball at hadronic freeze-out. The hydrodynamic model shares with most other dynamical models a series of problems which have become known as the “RHIC HBT puzzle”. Typically, the longitudinal HBT radius is overpredicted while the sideward radius and its transverse momentum dependence are underpredicted. Furthermore, all calculations give an outward radius which is significantly larger than the sideward radius, in contradiction with experiment which shows that both radii are about equal.

This implies a serious lack of our understanding of the decoupling process in heavy-ion collisions and how its details affect our interpretation of the size parameters extracted from two-particle interferometry. However, these two-particle correlations are only fixed at the end of the collision when the hadrons cease to interact strongly with each other. Our failure to reproduce the correlations within the hydrodynamic model therefore does not affect our successful description of the elliptic flow patterns (which are established much earlier) within the same model. This is important since a quantitative understanding of the global collision dynamics, especially

during its early stages, is crucial for a quantitative interpretation of “hard probes” such as jet quenching, direct photon and dilepton production and charmonium suppression. These cannot be successfully exploited as “early collision signatures” without a proper understanding of the global collision dynamics which the hydrodynamic model provides.

As shown in the last Section, this global picture can be further constrained by emission-angle dependent HBT interferometry which allows to correlate momentum anisotropies measured by  $v_2$  with spatial anisotropies at freeze-out measured by the azimuthal oscillation amplitudes of the HBT radius parameters. Preliminary data confirm the hydrodynamic prediction that, at RHIC energies, the source is still slightly elongated perpendicular to the reaction plane when the hadrons finally decouple. At the LHC, the spatial deformation at freeze-out is expected to have the opposite sign, the fireball being wider in the reaction plane than perpendicular to it.

### **Acknowledgments**

This work was supported in part by the U.S. Department of Energy under Grants No. DE-FG02-88ER40388 and DE-FG02-01ER41190. Peter Kolb also acknowledges support by the Alexander von Humboldt Foundation through a Feodor Lynen Fellowship.

## References

1. L.D. Landau, *Izv. Akad. Nauk Ser. Fiz.* 17 (1953) 51.
2. Proceedings of the 15th International Conference on Ultrarelativistic Nucleus-Nucleus Collisions (QM 2001), Stony Brook, New York, January 15-20, 2001, *Nucl. Phys. A* 698 (2002) 1.
3. Proceedings of the 16th International Conference on Ultrarelativistic Nucleus-Nucleus Collisions (QM 2002), Nantes, France, July 18-24, 2002, *Nucl. Phys. A* 715 (2003) 1.
4. P.F. Kolb, J. Sollfrank, and U. Heinz, *Phys. Rev. C* 62 (2000) 054909.
5. J. Engels, F. Karsch, H. Satz, and I. Montvay, *Nucl. Phys. B* 205 (1982) 545.
6. F. Karsch, *Nucl. Phys. A* 698 (2002) 199c.
7. D.H. Rischke, "Fluid Dynamics for Relativistic Nuclear Collisions" in "Hadrons in Dense Matter and Hadrosynthesis" (J.Cleymans et al., eds., Springer Verlag, Berlin, 1999).
8. L.P. Csernai, "Introduction to relativistic heavy ion collisions", (Wiley, New York, 1994).
9. P.V. Ruuskanen, *Acta Phys. Pol.* 18 (1987) 551.
10. J.P. Blaizot and J.Y. Ollitrault, "Hydrodynamics of a quark gluon plasma", in: "Quark Gluon Plasma 2", R.C. Hwa (ed.), World Scientific, Singapore, 1990, p. 393.
11. H. Stöcker and W. Greiner, *Phys. Rept.* 137 (1986) 277.
12. R.B. Clare and D. Strottman, *Phys. Rept.* 141 (1986) 177.
13. U. Heinz and P.F. Kolb, *Nucl. Phys. A* 702 (2002) 269.
14. U. Heinz and P.F. Kolb, hep-ph/0204061, Proceedings of the 18th Winter Workshop on Nuclear Dynamics, Nassau, Bahamas, 20-27, 2002, (G.D. Westfall and W. Bauer, eds.), EP Systema, Debrecen, Hungary (2002)
15. S.A. Bass et al., *Phys. Rev. C* 60 (1999) 021902.
16. S.A. Bass and A. Dumitru, *Phys. Rev. C* 61 (2000) 064909.
17. S. Soff, S.A. Bass, and A. Dumitru, *Phys. Rev. Lett.* 86 (2001) 3981.
18. D. Teaney, J. Lauret, and E.V. Shuryak, *Phys. Rev. Lett.* 86 (2001) 4783.
19. D. Teaney, J. Lauret, and E.V. Shuryak, *nuc1h0037*.
20. D. Teaney, J. Lauret, and E.V. Shuryak, *Nucl. Phys. A* 698 (2002) 479.
21. B.A. Li, *Phys. Rev. C* 61 (2000) 021903(R).
22. E.V. Shuryak, *Phys. Rev. C* 61 (2000) 034905.
23. P.F. Kolb, P. Huovinen, U. Heinz, and H. Heiselberg, *Phys. Lett. B* 500 (2001) 232.
24. P.F. Kolb, J. Sollfrank, and U. Heinz, *Phys. Lett. B* 459 (1999) 667.
25. L.D. Landau and E.M. Lifshitz, "Fluid mechanics", (Addison-Wesley, Reading, Mass., 1959).
26. K.M. O'Hara, S.L. Hemmer, M.E. Gehm, S.R. Granade, and J.E. Thomas, *Science* 298 (2002) 2179.
27. C. Menotti, P. Pedri, and S. Stringari, *Phys. Rev. Lett.* 89 (2002) 250402.
28. J.P. Bondorf, S.I.A. Garpman, and J. Zimányi, *Nucl. Phys. A* 296 (1978) 320.

29. U. Heinz, K.S. Lee, and M. Rhoades-Brown, Phys. Rev. Lett. 58 (1987) 2292.
30. K.S. Lee, M. Rhoades-Brown, and U. Heinz, Phys. Rev. C 37 (1988) 1463.
31. C.M. Hung and E.V. Shuryak, Phys. Rev. C 57 (1998) 1891.
32. E. Schnedermann and U. Heinz, Phys. Rev. C 50 (1994) 1675.
33. A. Muronga, Phys. Rev. Lett. 88 (2002) 062302; Erratum *ibid.* 89 (2002) 159901.
34. P. Braun-Munzinger, I. Heppe, and J. Stachel, Phys. Lett. B 465 (1999) 15.
35. R. Hagedorn and J. Ranft, *Nuovo Cimento Suppl.* 6 (1968) 169.
36. K. Hagiwara et al. (Particle Data Group), Phys. Rev. D 66 (2002) 010001.
37. K.S. Lee, M. Rhoades-Brown, and U. Heinz, Phys. Rev. C 37 (1988) 1452.
38. J. Sollfrank et al., Phys. Rev. C 55 (1997) 392.
39. A. Chodos et al., Phys. Rev. D 9 (1974) 3471.
40. K. Geiger, *Comput. Phys. Commun.* **104** (1997) 70.
41. S.A. Bass, B. Müller, and D.K. Srivastava, Phys. Lett. B 551 (2003) 277.
42. D. Molnar and M. Gyulassy, Phys. Rev. C 62 (2000) 054907.
43. B. Zhang, C.M. Ko, B.A. Li, and Z.W. Lin, Phys. Rev. C 61 (2000) 067901.
44. C. Nonaka, E. Honda, and S. Muroya, *Eur. Phys. J. C* 17 (2000) 663.
45. R.J. Glauber, in “*Lectures on Theoretical Physics*”, Vol. 1, (W.E. Brittin, L.G. Dunham eds., Interscience, NY, 1959).
46. P.F. Kolb, P. Huovinen, U. Heinz, K. Eskola, and K. Tuominen, Nucl. Phys. A 696 (2001) 175.
47. D. Kharzeev and M. Nardi, Phys. Lett. B 507 (2001) 121.
48. B.B. Back et al. (PHOBOS Collaboration), Phys. Rev. Lett. 85 (2000) 3100.
49. B.B. Back et al. (PHOBOS Collaboration), Phys. Rev. Lett. 88 (2002) 022302.
50. K. Adcox et al. (PHENIX Collaboration), Phys. Rev. Lett. 86 (2001) 3500.
51. B.B. Back et al. (PHOBOS Collaboration), Phys. Rev. C 65 (2002) 031901(R).
52. A. Bohr and B.R. Mottelson, “*Nuclear structure*”, (Benjamin, New York, 1969).
53. A. Bialas, M. Bleszynski, and W. Czyz, Nucl. Phys. B 111 (1976) 461.
54. U. Heinz, K.S. Lee, and E. Schnedermann, in: “*The Nuclear Equation of State*”, (W. Greiner and H. Stöcker, eds.), NATO Asi Series B: Physics Vol. 216B (1989) 385, (Plenum Press, New York).
55. F. Cooper and G. Frye, Phys. Rev. D 10 (1974) 186.
56. J. Sollfrank, P. Koch, and U. Heinz, Phys. Lett. B 252 (1990) 256; and Z. Phys. C 52 (1991) 593.
57. F. Grassi, Y. Hama, and T. Kodama, Phys. Lett. B 355 (1995) 9.
58. Yu.M. Sinyukov, S.V. Akkelin, and Y. Hama, Phys. Rev. Lett. 89 (2002) 052301.
59. B. Tomášik and U.A. Wiedemann, arXiv:nucl-th/0207074.
60. K.A. Bugaev, Nucl. Phys. A 606 (1996) 559.
61. K.A. Bugaev, arXiv:nucl-th/0210087, Phys. Rev. Lett., in press.
62. J.D. Bjorken, Phys. Rev. D 27 (1983) 140.
63. G. Baym et al., Nucl. Phys. A 407 (1983) 541.

64. K.J. Eskola, K. Kajantie, and P.V. Ruuskanen, Eur. Phys. J. C 1 (1998) 627.
65. P.F. Kolb and R. Rapp, Phys. Rev. C 67 (2003) 044903.
66. P.F. Kolb, arXiv:nucl-th/0304036.
67. E. Schnedermann, J. Sollfrank, and U. Heinz, Phys. Rev. C 48 (1993) 2462.
68. E. Schnedermann, J. Sollfrank, and U. Heinz, in: "Particle production in highly excited matter", H.H. Gutbrod and J. Rafelski (eds.), NATO Asi Series B Vol. 303 (1993) 175 (Plenum Press, New York).
69. M. Prakash, M. Prakash, R. Venugopalan, and G. Welke, Phys. Rep. 227 (1993) 321.
70. J.-Y. Ollitrault, Phys. Rev. D 46 (1992) 229.
71. D. Teaney and E. Shuryak, Phys. Rev. Lett. 83 (1999) 4951.
72. P.F. Kolb, PhD-thesis, Universität Regensburg, 2002, published at <http://www.bibliothek.uni-regensburg.de/opus/volltexte/2002/66/>
73. P.F. Kolb and U. Heinz, Nucl. Phys. A 715 (2003) 653c.
74. U. Heinz and P.F. Kolb, Phys. Lett. B 542 (2002) 216.
75. H. Sorge, Phys. Rev. Lett. 78 (1997) 2309.
76. H. Sorge, Phys. Rev. Lett. 82 (1999) 2048.
77. B. Zhang, M. Gyulassy, and C.M. Ko, Phys. Lett. B 455 (1999) 45.
78. D. Molnar and M. Gyulassy, Nucl. Phys. A 697 (2002) 495, Erratum-ibid. A 703 (2002) 893; Nucl. Phys. A 698 (2002) 379.
79. B. Tomášik and U.A. Wiedemann, arXiv:hep-ph/0210250, this volume.
80. S.A. Voloshin and Y. Zhang, Z. Phys. C 70 (1996) 665
81. P. Huovinen, P.F. Kolb, U. Heinz, P.V. Ruuskanen, and S.A. Voloshin, Phys. Lett. B 503 (2001) 58.
82. P. Braun-Munzinger, D. Magestro, K. Redlich, and J. Stachel, Phys. Lett. B 518 (2001) 41.
83. K.S. Lee, U. Heinz, and E. Schnedermann, Z. Phys. C 48 (1990) 525.
84. J. Velkovska et al. (PHENIX Collaboration), Nucl. Phys. A 698 (2002) 507.
85. C. Adler et al. (STAR Collaboration), Phys. Rev. Lett. 87 (2001) 262302.
86. M. Calderon de la Barca Sanchez, Ph.D. Thesis, arXiv:nucl-ex/0111004.
87. D. Teaney, arXiv:nucl-th/0204023.
88. R. Rapp, Phys. Rev. C 66 (2002) 017901.
89. T. Hirano and K. Tsuda, Phys. Rev. C 66 (2002) 054905.
90. P.F. Kolb, J. Sollfrank, P.V. Ruuskanen, and U. Heinz, Nucl. Phys. A 661 (1999) 349c.
91. K. Adcox et al. (PHENIX Collaboration), Phys. Rev. Lett. 88 (2002) 242301.
92. J.M. Burward-Hoy et al. (PHENIX Collaboration), Nucl. Phys. A 715 (2003) 498c.
93. P.J. Siemens and J.O. Rasmussen, Phys. Rev. Lett. 42 (1979) 880.
94. C. Adler et al. (STAR Collaboration), Phys. Rev. Lett. 89 (2002) 092301.
95. G. van Buren et al. (STAR Collaboration), Nucl. Phys. A 715 (2003) 129c.
96. J. Castillo et al. (STAR Collaboration), Nucl. Phys. A 715 (2003) 518c.
97. C. Suerre et al. (STAR Collaboration), Nucl. Phys. A 715 (2003) 470c.
98. H. van Hecke, H. Sorge, and N. Xu, Phys. Rev. Lett. 81 (1998) 5764.
99. T. Chujo et al. (PHENIX Collaboration), Nucl. Phys. A 715 (2003) 151c.

100. O. Barannikova and F. Wang et al. (STAR Collaboration), Nucl. Phys. A 715 (2003) 458c.
101. B. Wosiek et al. (PHOBOS Collaboration), Nucl. Phys. A 715 (2003) 510c.
102. D. Ouerdane et al. (BRAHMS Collaboration), Nucl. Phys. A 715 (2003) 478c.
103. I. Vitev and M. Gyulassy, Phys. Rev. C 65 (2002) 041902.
104. R.J. Fries, B. Müller, C. Nonaka, and S.A. Bass, arXiv:nucl-th/0301087.
105. M. Velkovsky et al. (PHENIX Collaboration), to be published in the proceedings of 7th International Conference on Strangeness in Quark Matter (SQM2003) (Atlantic Beach, North Carolina, March 12 - 17, 2003), J. Phys. G, in press.
106. M.M. Aggarwal et al. (WA98 Collaboration), Eur. Phys. J. C 18 (2001) 651.
107. K. Adcox et al. (PHENIX Collaboration), Phys. Rev. Lett. 87 (2001) 052301.
108. A. Bazilevsky et al. (PHENIX Collaboration), Nucl. Phys. A 715 (2003) 486c.
109. H. Heiselberg and A.M. Levy, Phys. Rev. C 59 (1999) 2716.
110. A. Krasnitz, Y. Nara and R. Venugopalan, Phys. Lett. B 554 (2003) 21.
111. S.A. Voloshin and A.M. Poskanzer, Phys. Lett. B 474 (1999) 27.
112. H. Appelshäuser et al. (NA49 Collaboration), Phys. Rev. Lett. 80 (1998) 4136. Updated data can be found on the home-page of the NA49 Collaboration: <http://na49-info.cern.ch/na49/Archives/Images/Publications/Phys.Rev.Lett.80:4136-4140,1998>.
113. N. Borghini, P.M. Dinh, and J.-Y. Ollitrault, Phys. Rev. C 62 (2000) 034902.
114. C. Pinkenburg et al. (E895 Collaboration), Phys. Rev. Lett. 83 (1999) 1295.
115. N. Borghini, P.M. Dinh and J.-Y. Ollitrault, Phys. Rev. C 63 (2001) 054906.
116. N. Borghini, P.M. Dinh and J.-Y. Ollitrault, Phys. Rev. C 64 (2001) 054901.
117. P.M. Dinh, N. Borghini and J. Y. Ollitrault, Phys. Lett. B 477 (2000) 51.
118. N. Borghini, P.M. Dinh, J.-Y. Ollitrault, A.M. Poskanzer and S.A. Voloshin, Phys. Rev. C 66 (2002) 014901.
119. N. Borghini, arXiv:hep-ph/0302139, Eur. Phys. J. C, in press.
120. Y.V. Kovchegov and K.L. Tuchin, Nucl. Phys. A 708 (2002) 413.
121. C. Adler et al. (STAR Collaboration), Phys. Rev. C 66 (2002) 034904.
122. C. Alt et al. (NA49 Collaboration), nucl-ex/0303001.
123. J. Slivova et al. (CERES/NA45 Collaboration), nucl-ex/0212013.
124. K.H. Ackermann et al. (STAR Collaboration), Phys. Rev. Lett. 86 (2001) 402.
125. C. Adler et al. (STAR Collaboration), Phys. Rev. Lett 90 (2003) 032301.
126. E.V. Shuryak, arXiv:hep-ph/0205031.
127. D. Molnar and S.A. Voloshin, arXiv:nucl-th/0302014.
128. S.A. Voloshin, Nucl. Phys. A 715 (2003) 379c.
129. C. Adler et al. (STAR Collaboration), Phys. Rev. Lett. 87 (2001) 182301.
130. K. Adcox et al. (PHENIX Collaboration), Phys. Rev. Lett. 89 (2002) 212301.
131. C. Adler et al. (STAR Collaboration), Phys. Rev. Lett. 89 (2002) 132301.
132. S. Esumi et al. (PHENIX Collaboration), Nucl. Phys. A 715 (2003) 599c; S.S. Adler et al. (PHENIX Collaboration), nucl-ex/0205013.
133. P. Sorensen et al. (STAR Collaboration), to be published in the proceedings

of 7th International Conference on Strangeness in Quark Matter (SQM2003) (Atlantic Beach, North Carolina, March 12 - 17, 2003), *J. Phys. G*, in press.

134. H. Sorge, *Phys. Rev. C* 52 (1995) 3291.
135. P. Huovinen, P.F. Kolb, and U. Heinz, *Nucl. Phys. A* 698 (2002) 475.
136. P. Chung et al. (E895 Collaboration), *Phys. Rev. C* 66 (2002) 021901(R).
137. P. Danielewicz et al., *Phys. Rev. Lett.* 81 (1998) 2438.
138. B.B. Back et al. (PHOBOS Collaboration), *Phys. Rev. Lett.* 88 (2002) 022302.
139. S.A. Bass et al., *Nucl. Phys. A* 661 (1999) 205.
140. H. Appelshäuser et al. (NA49-Collaboration), *Phys. Rev. Lett.* 82 (1999) 2471.
141. T. Hirano, *Phys. Rev. Lett.* 86 (2001) 2754.
142. T. Hirano, *Phys. Rev. C* 65 (2001) 011901(R).
143. T. Hirano, K. Morita, S. Muroya, and C. Nonaka, *Phys. Rev. C* 65 (2002) 061902.
144. K. Morita, S. Muroya, C. Nonaka, and T. Hirano, *Phys. Rev. C* 66 (2002) 054904.
145. B.B. Back et al. (PHOBOS Collaboration), *Phys. Rev. Lett.* 89 (2002) 222301.
146. P.F. Kolb, arXiv:nucl-th/0104089, Proceedings of the 17th Winter Workshop on Nuclear Dynamics, Park City, Utah, March 10-17, 2001, (G.D. Westfall and W. Bauer, eds.), EP Systema, Debrecen, Hungary (2001).
147. S. Manly et al. (PHOBOS Collaboration), *Nucl. Phys. A* 715 (2003) 611c.
148. Z. Fodor and S.D. Katz, *J. High Energy Phys.* 03 (2002) 014.
149. K. Paech, H. Stöcker, and A. Dumitru, arXiv:nucl-th/0302013.
150. S. Mioduszewski et al. (PHENIX Collaboration), *Nucl. Phys. A* 715 (2003) 199c.
151. J.L. Klay et al. (STAR Collaboration), *Nucl. Phys. A* 715 (2003) 733c; J. Adams et al. (STAR Collaboration), nucl-ex/0305015.
152. C.E. Jørgensen et al. (BRAHMS Collaboration), *Nucl. Phys. A* 715 (2003) 741c.
153. C. Roland et al. (PHOBOS Collaboration), *Nucl. Phys. A* 715 (2003) 745c.
154. M. Gyulassy, I. Vitev, X. N. Wang, and B. W. Zhang, arXiv:nucl-th/0302077, in this volume.
155. T. Peitzmann, arXiv:nucl-th/0303046.
156. V. Greco, C.M. Ko and P. Levai, arXiv:nucl-th/0301093.
157. Z.W. Lin and D. Molnar, arXiv:nucl-th/0304045.
158. X.N. Wang, *Phys. Rev. C* 63 (2001) 054902.
159. D. Teaney and R. Venugopalan, *Phys. Lett. B* 539 (2002) 53.
160. K. Filimonov et al. (STAR-Collaboration), *Nucl. Phys. A* 715 (2003) 137c. nucl-ex/0210027.
161. M. Gyulassy, I. Vitev, and X.N. Wang, *Phys. Rev. Lett.* 86 (2001) 2537.
162. M. Gyulassy, I. Vitev, X.N. Wang, and P. Huovinen, *Phys. Lett. B* 526 (2002) 301.
163. T. Hirano and Y. Nara, *Phys. Rev. C* 66 (2002) 041901(R).

164. E.V. Shuryak, Phys. Rev. C 66 (2002) 027902.
165. R. Hanbury-Brown and R.Q. Twiss, Nature 178 (1956) 1046.
166. U.A. Wiedemann and U. Heinz, Phys. Rept. 319 (1999) 145.
167. U. Heinz and B.V. Jacak, Ann. Rev. Nucl. Part. Sci. 49 (1999) 529.
168. E.V. Shuryak, Phys. Lett. B 44 (1973) 387.
169. B.R. Schlei, U. Ornik, M. Plümer, and R.M. Weiner, Phys. Lett. B 293 (1992) 275.
170. S. Chapman and U. Heinz, Phys. Lett. B 340 (1994) 250.
171. T. Csörgő and B. Lörstad, Phys. Rev. C 54 (1996) 1390.
172. S. Chapman, J.R. Nix, and U. Heinz, Phys. Rev. C 52 (1995) 2694.
173. B. Tomášik, U.A. Wiedemann and U. Heinz, Heavy Ion Phys. 17 (2003) 105.
174. U.A. Wiedemann and U. Heinz, Phys. Rev. C 56 (1997) 3265.
175. Z.W. Lin, C.M. Ko, and S. Pal, Phys. Rev. Lett. 89 (2002) 152301.
176. S. Chapman, P. Scotto, and U. Heinz, Phys. Rev. Lett. 74 (1995) 4400.
177. D.H. Rischke and M. Gyulassy, Nucl. Phys. A 608 (1996) 479.
178. C. Adler et al. (STAR Collaboration), Phys. Rev. Lett. 87 (2001) 082301.
179. K. Adcox et al. (PHENIX Collaboration), Phys. Rev. Lett. 88 (2002) 192302.
180. A. Enokizono et al. (PHENIX Collaboration), Nucl. Phys. A 715 (2003) 595c.
181. H. Heiselberg and A.P. Vischer, Eur. Phys. J. C 1 (1998) 593.
182. B. Tomášik and U. Heinz, arXiv:nucl-th/9805016, and Acta Phys. Slov. 49 (1999) 251.
183. L.D. McLerran and S.S. Padula, arXiv:nucl-th/0205028, Nucl. Phys. A, in press.
184. D. Molnar and M. Gyulassy, arXiv:nucl-th/0211017.
185. A. Dumitru, nucl-th/0206011.
186. D. Teaney, nucl-th/0301099.
187. U. Heinz and S.M.H. Wong, Phys. Rev. C 66 (2002) 014907.
188. U.A. Wiedemann, Phys. Rev. C 57 (1998) 266.
189. M.A. Lisa, U. Heinz, and U.A. Wiedemann, Phys. Lett. B 489 (2000) 287.
190. U. Heinz, A. Hummel, M.A. Lisa, and U.A. Wiedemann, Phys. Rev. C 66 (2002) 044903.
191. F. Retiere and M.A. Lisa, private communication and to be published.
192. M. López Noriega et al. (STAR Collaboration), Nucl. Phys. A 715 (2003) 623c.
193. M.A. Lisa et al. (STAR Collaboration), nucl-ex/0301005.